2017

Periodically patterned structures for nanoplasmonic and biomedical applications

Akshit Peer
Iowa State University

Recommended Citation

Peer, Akshit, "Periodically patterned structures for nanoplasmonic and biomedical applications" (2017). *Graduate Theses and Dissertations*. 15600.
https://lib.dr.iastate.edu/etd/15600

Periodically patterned structures for nanoplasmonic and biomedical applications

by

Akshit Peer

A dissertation submitted to the graduate faculty

in partial fulfillment of the requirements for the degree of

DOCTOR OF PHILOSOPHY

Major: Electrical Engineering

Program of Study Committee:
Rana Biswas, Major Professor
Jaeyoun Kim
Vikram L. Dalal
Joseph Shinar
Liang Dong

Iowa State University

Ames, Iowa

2017

DEDICATION

Dedicated to my grandparents and parents.

TABLE OF CONTENTS

ACKNOWLEDGEMENTS

I would like to express my sincere gratitude to my advisor Dr. Rana Biswas for his immense guidance and support during my PhD. Without his help, I would not have gotten the chance to come here and explore the interesting research happening in the world of nanophotonics. The various discussions I have had with him on problem solving approach and implementation have always challenged my analytical thinking and helped me grow scientifically over these years. He has always listened patiently to my research ideas and corrected me whenever I was wrong. I would also like to thank him for the positive feedback he has given for improving my various manuscripts, and exam and conference presentations. In addition to being an inspirational mentor, he has always shown personal interest in my overall career and helped me in every possible way to make an informed decision.

I am extremely obliged to my program of study committee member Dr. Jaeyoun Kim for his continuous guidance on the collaborative project related to biomaterials. I was introduced to the key aspects of experimental research while working in his laboratory. I am thankful to him for the various joint publications that have resulted from this collaboration. I would also miss our regular group meetings, which have helped me to expand my knowledge base outside the core photonics domain.

I am grateful to my other program of study committee members Dr. Vikram Dalal, Dr. Joseph Shinar, and Dr. Liang Dong for their time and constructive suggestions on my research. I am thankful to Dr. Vikram Dalal for laying my strong foundation in semiconductors through his courses, which has helped me at various

stages in my PhD. I am thankful to Dr. Liang Dong for offering us to use his laboratory equipment for our research. I also appreciate the time of my committee members for administering my preliminary and final oral exams.

I am thankful to Dr. Joseph Shinar and Dr. Ruth Shinar for their valuable guidance on the ongoing collaborative project on OLEDs. The measurements on OLEDs made by Dr. Joong-Mok Park have resulted in a joint publication with more collaborative publications anticipated in the future.

I am thankful to Dr. Sumit Chaudhary for agreeing to serve on my program of study committee before he left ISU. The experimental data provided by Dr. Ryan Gebhardt from his research group on including microlens arrays and high-index nanoparticles in organic solar cells resulted in a joint publication.

I would like to acknowledge Dr. Han Htoon for the opportunity to join his group at Los Alamos National Laboratory for the summer internship in 2016. I had a very valuable learning experience while working on the ultrafast laser spectroscopy of quantum dots, which later resulted in a collaborative publication. I thank Dr. Zhongjian Hu for training me on optical spectroscopy measurements. Special thanks to Dr. Ajay Singh from the research group of Dr. Jennifer Hollingsworth for synthesizing the desired quantum dots within a very short span of time.

I am thankful to Dr. W. Dennis Slafer from Microcontinuum Inc. for providing the flexible polycarbonate masters used extensively in my research for fabricating nanopatterned polymer surfaces.

I am grateful to my lab colleagues Dr. Rabin Dhakal and Qiang Li for assistance with experiments on soft lithography. I am thankful to Dr. Eeshita Manna for providing training on operating AFM. I am also thankful to MRC associates Dr. Pranav Joshi, Dr.

Mehran Samiee, Dr. Joydeep Bhattacharya, Dr. Hisham Abbas, and Dr. Tanvir Muntasir for various insightful discussions on coursework and research. I appreciate the assistance of Dr. Warren Straszheim from Materials Analysis and Research Laboratory with electron microscopy imaging of extremely fragile polymer samples. I am grateful to the extensive assistance provided by Dr. Ann Perera from W. M. Keck Metabolomics Laboratory for setting up the high-performance liquid chromatography experiment and troubleshooting at various stages.

I am delighted to acknowledge the conducive research environment provided by Iowa State University and Ames Laboratory. I am grateful to ISU Research Foundation for submitting the provisional patent application on our drug delivery research. I sincerely thank the ECE department for nominating me for the prestigious Research Excellence Award. The administrative support from MRC and ECE department staff members especially Nancy Johnson, Vicky Thorland-Oster, and Sara Harris has been very useful during these years. Thanks to the communications specialist Kristin Clague for including our various research highlights on the department website.

I am grateful to my undergraduate advisors especially Dr. Ajeet Kumar (Delhi Technological University) and Dr. Vipul Rastogi (Indian Institute of Technology Roorkee) for introducing me to optics research.

I would like to acknowledge the funding agencies U.S. National Science Foundation (NSF) and U.S. Department of Energy (DOE) for generously supporting the research reported in this dissertation. I am especially thankful to the massively parallel computing support provided by the National Energy Research Scientific Computing Center (NERSC), a U.S. DOE high-performance computing facility with more than 200,000 nodes located in Berkeley, California.

I am fortunate to have the support of my friends namely Anup, Pranav, Santosh, Anuj, Satvik, Anand, Viraj, Amulya, Gauri, and Bhakti, who made my stay at Ames a joyful and rewarding experience. Special thanks to my distant friend Gautam for being instrumental in my admission to the doctoral program, and always being there for the advice and support when I needed him. His generous personality and passion for science has inspired me positively. The occasional group phone calls with my undergraduate friends Aseem, Ishaan, Puneet, and Vivek made my weekends more lively and cheerful.

Finally, this journey would not have been possible without the encouragement and support from my mother Anita Peer and father Bharat Bhushan Peer who have always trusted me and given me the freedom to pursue my goals. Their guidance and sacrifice at various instances has helped me to reach this stage of my life. I cannot forget to mention my grandparents whose unparalleled vision and values have always motivated me. Though most of them are physically not with me today, I am sure they would be proud had they been present.

Akshit Peer

ABSTRACT

Periodically patterned nanostructures have imparted profound impact on diverse scientific disciplines. In physics, chemistry, and materials science, artificially engineered photonic crystals have demonstrated an unprecedented ability to control the propagation of photons through light concentration and diffraction. The field of photonic crystals has led to many technical advances in fabricating periodically patterned nanostructures in dielectric/metallic materials and controlling the light-matter interactions at the nanoscale. In the field of biomaterials, it is of great interest to apply our knowledge base of photonic materials and explore how such periodically patterned structures control diverse biological functions by varying the available surface area, which is a key attribute for surface hydrophobicity, cell growth and drug delivery. Here we describe closely related scientific applications of large-scale periodically patterned polymers and metal nanostructures.

The dissertation starts with nanoplasmonics for improving photovoltaic devices, where we design and optimize experimentally realizable light-trapping nanostructures using rigorous scattering matrix simulations for enhancing the performance of organic and perovskite solar cells. The use of periodically patterned plasmonic metal cathode in conjunction with polymer microlens array significantly improves the absorption in solar cells, providing new opportunities for photovoltaic device design. We further show the unprecedented ability of nanoplasmonics to concentrate light at the nanoscale by designing a large-area plasmonic nanocup array with frequency-selective optical transmission. The fabrication of nanostructure is achieved by coating non-uniform gold

layer over a submicron periodic nanocup array imprinted on polystyrene using soft lithography. The gold nanocup array shows extraordinary optical transmission at a wavelength close to the structure period. The resonance wavelength for transmission can be tuned by changing the period of the gold nanocup array, which opens up new avenues in subwavelength optics for designing optoelectronic devices and biological sensors. We then demonstrate strong exciton-plasmon coupling between non-toxic $CuInS_2/ZnS$ quantum dots in solution and plasmonic gold nanocup array. The photoluminescence decay rate of quantum dots can be enhanced by more than an order of magnitude due to the high electric field intensity enhancement inside the plasmonic nanocup cavity. This solution based metal-nanocrystal coupled system has great promise for biological applications such as biosensing and biolabeling.

Moving to the area of biomedical applications, we fabricate nanopatterned biopolymers as templates for controlling the release of therapeutic drugs coated on the polymer surface. From careful drug release experiments performed over extended time periods (e.g. eight days), we find that nanopatterned polymers release the drug slower as compared to the flat polymer surfaces. The slow-down in the drug release from nanopatterned surfaces is attributed to increase in the surface hydrophobicity confirmed by the contact angle measurements and microfluidic simulations. This nanoscale drug release control scheme has great promise for improving the performance of drug-eluting stents in cardiac therapies.

CHAPTER 1

INTRODUCTION

1.1 Motivation

Periodically patterned structures play an important role in enhancing the performance of various optoelectronic devices such as solar cells and light-emitting diodes by improving the light management inside these devices. Incorporation of nanopatterned structures as back reflectors or electrodes in solar cells increases the path length of light inside the absorber material resulting in enhanced absorption and photocurrent [1-10]. Similarly, including flexible polymer microlenses on the air-glass side external to the solar cells increases the light absorption significantly [11-13]. The nanopatterned surfaces can also be coated with thin layers of metals such as gold and silver, resulting in formation of interesting plasmonic nanostructures. These plasmonic nanostructures have the unprecedented ability to focus electromagnetic energy at the nanoscale level and offer a route to uniquely control the light-matter interaction [14-18].

The recent advances in the development of biomaterials in parallel has also led to the application of patterned polymer surfaces in various biomedical systems [19-31]. Nanopatterning the biopolymer surfaces can increase the available surface area, which is a key attribute for tissue culture and cell growth. Nanopatterned materials involving hydrophobic surfaces such as electrospun fiber meshes and nanoporous templates have been leveraged for controlling the drug release rate in complex drug delivery systems [32-34].

With these important applications, it is of great interest to develop methods for large-area scalable nanofabrication of such patterned structures. The conventional nanopatterning approaches such as electron beam lithography, reactive ion etching, or focused ion beam milling can only be used to pattern areas typically much smaller than 500 μm × 500 μm. Such small area samples are not suitable for applications such as solar cells, sensor arrays, and display devices. Recently over the last two decades, soft lithography has been used extensively for imprinting, embossing and molding the polymer surfaces on microscale or nanoscale level using an elastomeric stamp. This technique is described in detail in the following section.

1.2 Soft Lithography

Soft lithography is a technique of replicating structures using elastomeric stamps, molds and conformable photomasks [35-38]. The term 'soft' mainly refers to the elastomeric material, notably polydimethylsiloxane (PDMS), used extensively in the molding process. The features at the microscale or nanoscale level can easily be replicated using soft lithography with high fidelity. The soft lithography process is inexpensive as compared to the traditional photolithography approaches and can be scaled easily over large areas for mass production using roll-to-roll techniques. In addition, the initial elastomer stamp generated from a master pattern can be reused easily over many patterning cycles without significant degradation. The other advantages include compatibility with biotechnology, flexible electronics, and non-planar surfaces. In this dissertation, we use two variants of soft lithography described below to imprint our polymer films.

1.2.1 Nanoimprinting

In the nanoimprinting approach, the patterned side of the stamp faces the polymer surface to be patterned, and the whole assembly is typically held together between the two glass slides under the effect of temperature and pressure. The imprint temperature is the key parameter in this process. For an effective pattern transfer, the imprint temperature should typically be much higher than the glass transition temperature of the polymer to be imprinted. The pressure can usually be applied using a set of binder clips or an imprint press. The whole assembly is kept under the effect of temperature and pressure for the desired period. Figure 1.1 illustrates the process for imprinting the polystyrene film from a PDMS stamp using this method.

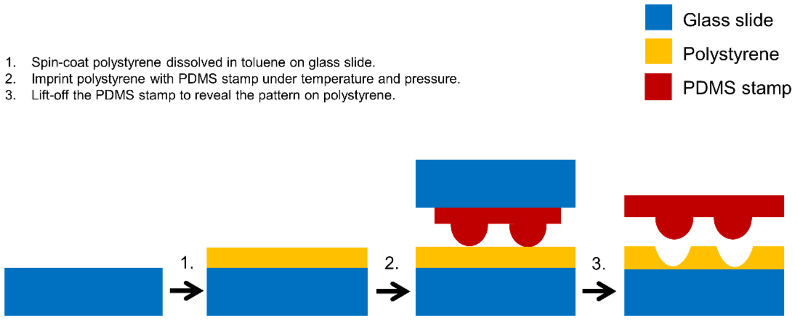
1. Spin-coat polystyrene dissolved in toluene on glass slide.
2. Imprint polystyrene with PDMS stamp under temperature and pressure.
3. Lift-off the PDMS stamp to reveal the pattern on polystyrene.

Figure 1.1. Schematic of the process for nanoimpriting polystyrene film over glass substrate using a PDMS stamp. The pattern transfer is achieved using desired temperature and pressure.

1.2.2 Solution drop casting

In the solution-based drop casting approach, the polymer to be patterned is dissolved in a suitable solvent and the solution is poured on a PDMS mold. After letting the solvent evaporate and dry for the desired period, the polymer film is peeled off from the PDMS mold to reveal the patterns on the surface. Figure 1.2 illustrates the process for fabricating nanopatterned poly(L-lactic acid) film using this method.

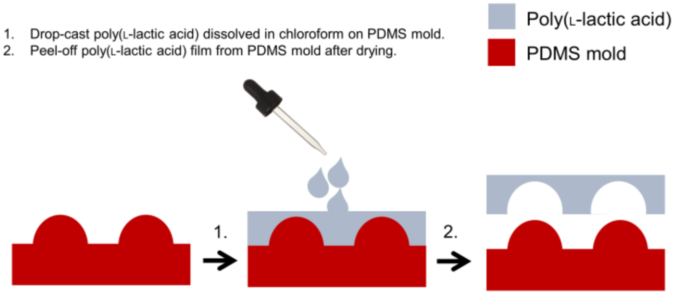
1. Drop-cast poly(L-lactic acid) dissolved in chloroform on PDMS mold.
2. Peel-off poly(L-lactic acid) film from PDMS mold after drying.

Figure 1.2. Schematic of the process for fabricating patterned poly(L-lactic acid) film by solution drop casting. The final pattern transfer is achieved by peeling-off the dried film from PDMS mold.

1.3 Electromagnetic Simulations

In this section, we provide a brief summary of the electromagnetic simulations that are used extensively in the dissertation to model the optical properties of periodic nanostructures. The periodic nanostructures are essentially photonic crystals with periodically varying dielectric constant either in one, two or three dimensions. The propagation of electromagnetic waves in photonic crystals can be described by the macroscopic Maxwell's equations:

$$\begin{gathered} \nabla . \boldsymbol{D} = \rho \\ \nabla . \boldsymbol{B} = 0 \\ \nabla \times \boldsymbol{E} + \frac{\partial \boldsymbol{B}}{\partial t} = 0 \\ \nabla \times \boldsymbol{H} - \frac{\partial \boldsymbol{D}}{\partial t} = \boldsymbol{J} \end{gathered} \tag{1.1}$$

where **E** and **B** denote the electric field and magnetic field, **D** and **H** denote the electric displacement and magnetic induction, respectively. In the absence of free charge and current, equations (1.1) reduce to:

$$\begin{gathered} \nabla . \boldsymbol{D} = 0 \\ \nabla . \boldsymbol{B} = 0 \\ \nabla \times \boldsymbol{E} + \frac{\partial \boldsymbol{B}}{\partial t} = 0 \\ \nabla \times \boldsymbol{H} - \frac{\partial \boldsymbol{D}}{\partial t} = 0 \end{gathered} \tag{1.2}$$

For the case of linear isotropic materials, the constitutive relation gives,

$$\begin{gathered} \boldsymbol{D}(\boldsymbol{r}, \omega) = \varepsilon(\boldsymbol{r}, \omega) \boldsymbol{E}(\boldsymbol{r}, \omega) \\ \boldsymbol{B}(\boldsymbol{r}, \omega) = \mu(\boldsymbol{r}, \omega) \boldsymbol{H}(\boldsymbol{r}, \omega) \end{gathered} \tag{1.3}$$

where ε is the permittivity and μ is permeability. For most of the simulations presented here, ε is a complex valued function dependent on the frequency and position, whereas μ is a constant. By combining the constitutive relations (1.3) with Maxwell's equations, we obtain:

$$\begin{aligned}\nabla\times\boldsymbol{E}(\boldsymbol{r},t)&=-\mu\frac{\partial\boldsymbol{H}(\boldsymbol{r},t)}{\partial t}\\ \nabla\times\boldsymbol{H}(\boldsymbol{r},t)&=\varepsilon(\boldsymbol{r})\frac{\partial\boldsymbol{E}(\boldsymbol{r},t)}{\partial t}\end{aligned}\tag{1.4}$$

In terms of time harmonically varying fields with time dependence $e^{-i\omega t}$, the above equations can be expressed as follows:

$$\begin{aligned}\nabla\times\boldsymbol{E}(\boldsymbol{r})&=i\omega\mu\boldsymbol{H}(\boldsymbol{r})\\ \nabla\times\boldsymbol{H}(\boldsymbol{r})&=-i\omega\varepsilon(\boldsymbol{r})\boldsymbol{E}(\boldsymbol{r})\end{aligned}\tag{1.5}$$

Taking the curl of the above equation both sides, we get,

$$\nabla\times\left(\frac{1}{\varepsilon(\boldsymbol{r})}\right)\nabla\times\boldsymbol{H}(\boldsymbol{r})=-i\omega\nabla\times\boldsymbol{E}(\boldsymbol{r})\tag{1.6}$$

$$\nabla\times\left(\frac{1}{\varepsilon(\boldsymbol{r})}\right)\nabla\times\boldsymbol{H}(\boldsymbol{r})=\left(\frac{\omega}{c}\right)^2\boldsymbol{H}(\boldsymbol{r})\tag{1.7}$$

where c is the speed of light. This is an eigenvalue equation with eigenvalue $\left(\frac{\omega}{c}\right)^2$ and an eigen operator Θ given by [39]:

$$\Theta=\nabla\times\left(\frac{1}{\varepsilon(\boldsymbol{r})}\right)\nabla\times\tag{1.8}$$

The eigenvalue equation (1.7) can be solved by computer simulations for large structures.

For a two-dimensional periodic crystal, the initial wave-vector $\boldsymbol{k}_\mathrm{i}$ of the incident wave can be defined as follows:

$$\boldsymbol{k}_i=k_{ix}\hat{\boldsymbol{i}}+k_{iy}\hat{\boldsymbol{y}}+k_{iz}\hat{\boldsymbol{z}}\tag{1.9}$$

The incident and reflected electric field vectors would be given by the following expressions:

$$\boldsymbol{E}_i = \boldsymbol{E}_0 e^{-i\boldsymbol{k}_i \cdot \boldsymbol{r}} = \boldsymbol{E}_0 e^{-i(k_x x + k_y y + k_z z)}$$
$$\boldsymbol{E}_r = \sum_{m,n} \boldsymbol{E}_{r0,mn} e^{-i\boldsymbol{k}_{r,mn} \cdot \boldsymbol{r}} \tag{1.10}$$

where $\boldsymbol{E}_{\mathrm{r0,mn}}$ is the magnitude of the diffracted wave of (m,n)th order and the integers m and n define the order of the waves diffracted from the periodic crystal.

From the phase matching condition and Floquet condition, the wave-vector of the reflected wave can be expressed as:

$$\boldsymbol{k}_{r,mn} = k_{xm}\hat{\boldsymbol{i}} + k_{yn}\hat{\boldsymbol{j}} + k_{zr,mn}\hat{\boldsymbol{k}} \tag{1.11}$$

where,

$$\begin{aligned} k_{xm} &= k_x + mG_x \\ k_{yn} &= k_y + nG_y \\ k_{zr,mn}^2 &= k_i^2 - k_{xm}^2 - k_{yn}^2 \end{aligned} \tag{1.12}$$

G_{x} and G_{y} are the unit vectors of the reciprocal lattice vector $\boldsymbol{G}$.

For the square lattice,

$$\boldsymbol{G}_1 = \frac{2\pi}{a}(1,0);\boldsymbol{G}_2 = \frac{2\pi}{a}(0,1) \tag{1.13}$$

whereas for the triangular lattice,

$$\boldsymbol{G}_1 = \frac{2\pi}{a}\left(1,-\frac{1}{\sqrt{3}}\right);\boldsymbol{G}_2 = \frac{2\pi}{a}\left(0,\frac{2}{\sqrt{3}}\right) \tag{1.14}$$

In the above equations, $\boldsymbol{G}_1$ and $\boldsymbol{G}_2$ are the components of the reciprocal lattice vector, and a is the lattice period.

If $k_{zr,mn}^2 > 0$, the wave reflected from the crystal is a propagating wave, otherwise it is an evanescent wave that decays exponentially away from the surface.

1.3.1 Scattering matrix method

We use the scattering matrix method (SMM) to simulate the properties of periodic structures. SMM has been used extensively to calculate the reflection and transmission of layered structures. In this approach, the Maxwell's equations are solved in Fourier space in three-dimensions. The entire structure, which is periodic in the *x* and *y* directions, is divided into thin slices in *z*-direction as shown in Figure 1.3.

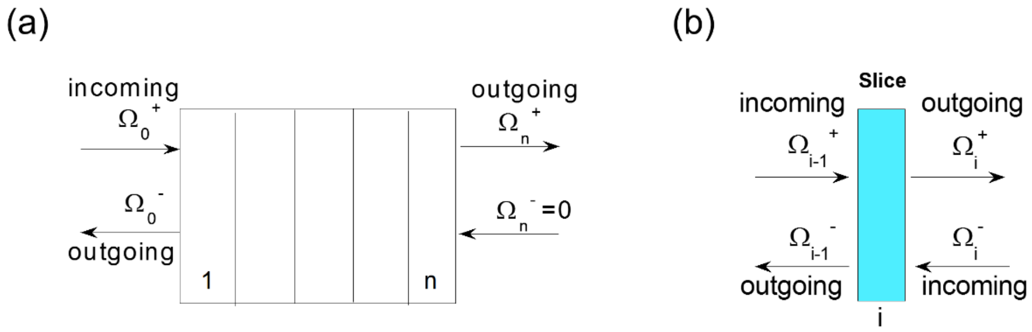

Figure 1.3. (a) Schematic showing the *S* matrix setup for a structure with *n* layers. (b) Schematic showing the *S* matrix setup for an individual slice within the structure.

For each slice *i*, the incoming and outgoing fields can be expressed in terms of the following matrix, with s^i being the scattering matrix for each slice *i*.

$$\begin{pmatrix}\Omega_i^+\\ \Omega_{i-1}^-\end{pmatrix}=\left(s^i\right)\begin{pmatrix}\Omega_{i-1}^+\\ \Omega_i^-\end{pmatrix} \tag{1.15}$$

The total scattering matrix *S*, which relates the incident, transmitted and reflected fields from all the layers, can be expressed as

$$\begin{pmatrix}\Omega_n^+\\ \Omega_0^-\end{pmatrix}=\left(S\right)\begin{pmatrix}\Omega_0^+\\ \Omega_n^-\end{pmatrix} \tag{1.16}$$

Since the structure is periodic in *x* and *y*, the dielectric function $\varepsilon(\boldsymbol{r})$ is a periodic function of the planar coordinates (*x*,*y*) in each slice. Hence the dielectric function $\varepsilon(\boldsymbol{r})$ and its inverse $\varepsilon^{-1}(\boldsymbol{r})$ can be expressed as a Fourier expansion with coefficients $\varepsilon(\mathbf{G})$ or $\varepsilon^{-1}(\mathbf{G})$, as follows:

$$\begin{aligned} \varepsilon(\boldsymbol{r}) &= \sum_{mn} \varepsilon(\boldsymbol{G}_{mn}) e^{-i\boldsymbol{G}_{mn}.\boldsymbol{r}} \\ \varepsilon^{-1}(\boldsymbol{r}) &= \sum_{mn} \varepsilon^{-1}(\boldsymbol{G}_{mn}) e^{-i\boldsymbol{G}_{mn}.\boldsymbol{r}} \end{aligned} \tag{1.17}$$

A scattering matrix in each layer is calculated that relates the *z* dependence of the **E**, **H** fields in each layer. The transfer matrix includes both polarizations of the wave, and is diagonalized to obtain the eigenmodes within the layer. Continuity of the parallel components of **E** and **H** at each interface leads to the individual scattering matrices of each layer, which are then convoluted into the scattering matrix *S* for the entire structure using a recursion algorithm [40]. Using the total *S* matrix, we can obtain the reflection and transmission of the entire layered structure with fields incident either from the left or right side of the structure.

Since the scattering matrix is employed in frequency domain, the computation can be easily parallelized with each frequency or group of frequencies being sent to a different processor. The method is advantageous as compared to traditional methods such as finite-difference time-domain (FDTD) since there is no need to use a real space grid which requires enormous memory for thick structures.

1.3.2 Fourier transform of dielectric functions

As seen in the previous section, we need the Fourier transform of the dielectric function in order to calculate the reflection and transmission using scattering matrix simulation methodology. In many cases, the layer for which the Fourier transform is to be calculated would comprise of two or more than two materials, with one material residing in the background of the other. In this section, we show the method to compute the Fourier transform of the dielectric function for a triangular array of cylinders of material A located at the center of the lattice with material B as the background. This scheme is particularly useful when we are interested in solving periodic structures with an array of nanocups (or nanocones) residing in a different background material. Each nanocup (or nanocone) can further be divided into several layers in *z*-direction and the Fourier transform can be obtained for each circular cylinder with gradually tapering radius. Figure 1.4a shows the *xz* cross-section of a nanocone (yellow) residing in the background material (blue). The nanocone with base radius *R* has been divided into five cylindrical slices in z-direction each having a radius of *R*, 0.8*R*, 0.6*R*, 0.4*R* and 0.2*R*. As can be seen from *xy* cross-section in Figure 1.4b, each cylinder can be separately considered to be residing in the background material and the Fourier transform of the composite layer can be obtained using the scheme described below. In the later chapters, we will see that this slice-based decomposition scheme will be very useful for simulating the optical properties of periodic nanocup or nanocone arrays.

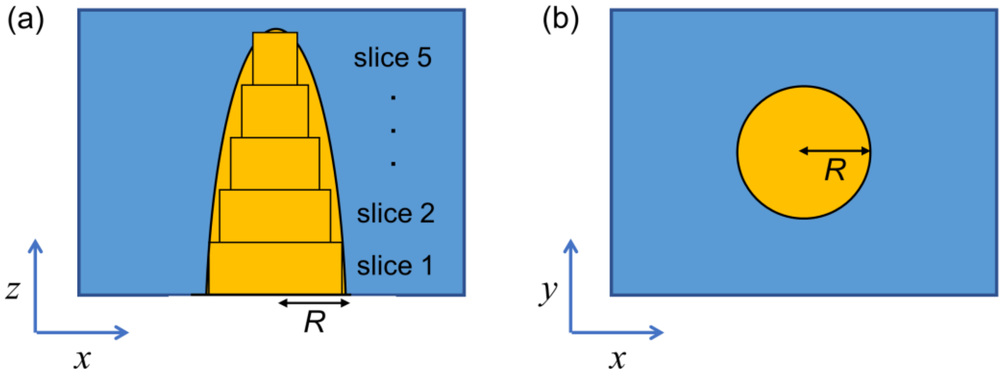

Figure 1.4. (a) Schematic illustrating *xz* cross-section of a nanocone (yellow) residing in the background material (blue). The nanocone has been divided into five cylindrical slices of decreasing radii in *z*-direction. (b) Schematic illustrating the *xy* cross-section of slice 1 of radius *R* residing in a background dielectric material.

Consider a geometry where we have a cylindrical material (yellow) of radius *R* residing in a background dielectric material (blue) with ε = ε(ω) as shown in Figure 1.5. For simplicity, let us assume that the cylindrical material is composed of air such that ε(ω) = 1.

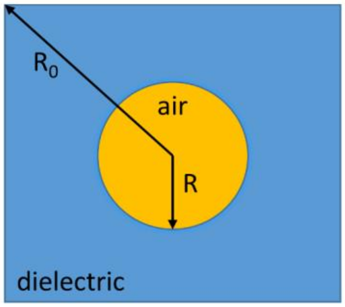

Figure 1.5. Schematic showing the *xy* cross-section of the cylindrical material (yellow) of radius *R* residing in a background dielectric material (blue).

Let us define a box function *s*(*x*) such that

$$s(x)=\begin{cases}1, \text{ for } x\in R,\\ 0, \text{ for } x\notin R\end{cases} \tag{1.18}$$

Consider the following two cases:

$$\begin{aligned}&x>R,\ \varepsilon=\varepsilon(\omega),\ s=0\\ &x<R,\ \varepsilon=1,\ s=1,\ \varepsilon=\varepsilon(\omega)+(1-\varepsilon(\omega)).s\end{aligned} \tag{1.19}$$

We can then write,

$$\varepsilon(x)=\varepsilon(\omega)+(1-\varepsilon(\omega)).\sum_{l} s(x_l-x_{cl}) \tag{1.20}$$

where x_{cl} is the center of the circle coordinate.

With a_c as the area of the unit cell, we have the following Fourier transform relations:

$$\begin{aligned}&\varepsilon(G)=\frac{1}{a_c}\int_{a_c} d^2x.\varepsilon(x).e^{-iG.x}\\ &\varepsilon(x)=\sum_{G}\varepsilon(G)e^{iG.x}\end{aligned} \tag{1.21}$$

We substitute the value of ε(*x*) from (1.20) in the expression of ε(*G*) to obtain the Fourier expansion of the dielectric function,

$$\varepsilon(G)=\frac{1}{a_c}\int_{a_c} d^2x.e^{-i\boldsymbol{G}.\boldsymbol{x}}[\varepsilon(\omega)+(1-\varepsilon(\omega)).\sum_l s(x_l-x_{cl})] \tag{1.22}$$

We now discuss the following two cases:

Case 1: G=0

$$\varepsilon(G=0)=\frac{1}{a_c}\int_{a_c} d^2x[\varepsilon(\omega)]+(1-\varepsilon(\omega)).\frac{1}{a_c}\int_{a_c} d^2x\sum_l s(x_l-x_{cl}) \tag{1.23}$$

For *l*=0, integration over the whole unit cell gives $\int_{a_c} d^2x\sum_l s(x_l-x_{cl})=\pi R^2$. Using this relation in (1.23) above gives,

$$\varepsilon(G=0)=\varepsilon(\omega)+(1-\varepsilon(\omega))\frac{\pi R^2}{a_c} \tag{1.24}$$

Case 2: G≠0

$$\varepsilon(G)=\frac{1}{a_c}\int_{a_c} d^2x.e^{-iG.x}[\varepsilon(\omega)]+(1-\varepsilon(\omega)).\frac{1}{a_c}\int_{a_c} d^2x.e^{-iG.x}\sum_l s(x_l-x_{cl}) \tag{1.25}$$

In the above expression, the first term on the right is zero, since it is an oscillating function when *G* is not equal to 0. The second term will be non-zero for only the *l*=0 part over the first unit cell, resulting in the following expression:

$$\varepsilon(G)=(1-\varepsilon(\omega)).\frac{1}{a_c}\int_{a_c} d^2x.s(x-R_0)e^{-iG.x} \tag{1.26}$$

By introducing the new variable $x'=x-R_0$, the above function becomes:

$$\varepsilon(G)=(1-\varepsilon(\omega)).\frac{1}{a_c}\int_{a_c} d^2x'.s(x')e^{-i\boldsymbol{G}.\boldsymbol{x}'}.e^{-i\boldsymbol{G}.\boldsymbol{R}_0} \tag{1.27}$$

Using the standard result of the Fourier transform for a cylinder,

$$\frac{1}{a_c}\int_{a_c} d^2x'.s(x')e^{-i\boldsymbol{G}.x'}.e^{-i\boldsymbol{G}.\boldsymbol{R}_0} = f.\frac{2J_1(GR)}{GR} \tag{1.28}$$

where J_1 is the Bessel function of the first kind and f is the filling ratio.

The dielectric function in (1.28) then becomes,

$$\varepsilon(G) = (1-\varepsilon(\omega)).f.\frac{2J_1(GR)}{GR}.e^{-i\boldsymbol{G}.\boldsymbol{R}_0} \tag{1.29}$$

where $e^{-i\boldsymbol{G}.\boldsymbol{R}_0}$ is the phase factor, which is generally complex.

The same treatment can be extended to calculate the Fourier transform for composite layers consisting of three or four different materials.

1.4 Dissertation Organization

We describe closely related applications of periodically patterned structures for nanoplasmonics and biomedical systems. The periodic structures are fabricated using soft lithography techniques described above, and the experimental results are supported with simulations and modeling. The dissertation is organized as follows:

Chapter 2 describes how periodic nanostructures can enhance the light absorption of organic solar cells using a dual-photonic crystal architecture. The proposed light-trapping architecture consists of polymer microlens at the top and photonic crystal metal cathode at the back of the solar cell. Using rigorous scattering matrix simulations, we optimize the structural parameters to obtain maximum enhancement in organic solar cells. We also estimate the amount of parasitic losses due to the presence of anode (usually ITO) and metal cathode.

Chapter 3 describes the application of polymer-based microlens arrays in enhancing the performance of perovskite solar cells and organic light-emitting diodes. We demonstrate the fabrication of polymer microlenses using nanoimprint lithography. Using rigorous scattering matrix simulations, we calculate the enhancement in photocurrent for the perovskite solar cells. We experimentally show the improvement in light extraction from organic light-emitting diodes when coupled to a microlens array.

Chapter 4 describes the fabrication and characterization of gold-coated periodic nanocup array imprinted on polystyrene film. The periodic nanocup array exhibits extraordinary optical transmission due to the non-uniform gold coating whose thickness varies spatially over the nanocup. The nanocup cavity exhibits 100-fold enhancement in electric field intensity due to plasmonic light concentration, confirmed using rigorous scattering matrix simulations.

Chapter 5 describes the follow-up work on previous chapter where semiconductor quantum dots in solution are coupled to this gold nanocup array. The photoluminescence decay lifetime of the quantum dots residing inside the nanocup, measured using time-resolved laser spectroscopy, is enhanced by more than an order of magnitude. This faster decay is a result of the high plasmonic field intensity inside the nanocup array.

Chapter 6 describes the application of nanopatterned biopolymers as templates for drug release. Nanopatterning the biopolymer surface renders it hydrophobic, making the release of therapeutic drugs coated on the surface much slower as compared to the flat control surface. The incomplete wetting, which is a result of the hydrophobicity, is also confirmed using contact angle measurements and microfluidic simulations. This nanoscale drug release scheme has vital applications in many biomedical areas including stents in cardiac therapies.

Chapter 7 provides the conclusion of the work with a future outlook.

1.5 References

1. D. Zhou and R. Biswas, "Photonic crystal enhanced light-trapping in thin film solar cells," *J. Appl. Phys.* **103**, 093102 (2008).

2. B. Curtin, R. Biswas and V. Dalal, "Photonic crystal based back reflectors for light management and enhanced absorption in amorphous silicon solar cells," *Appl. Phys. Lett.* **95**, 231102 (2009).

3. R. Biswas, J. Bhattacharya, B. Lewis, N. Chakravarty and V. Dalal, "Enhanced nanocrystalline silicon solar cell with a photonic crystal back-reflector," *Sol. Energy Mater. Sol. Cells* **94**, 2337-2342 (2010).

4. R. Biswas and C. Xu, "Nano-crystalline silicon solar cell architecture with absorption at the classical 4n2 limit," *Opt. Express* **19**, A664-A672 (2011).

5. J. Bhattacharya, N. Chakravarty, S. Pattnaik, W. D. Slafer, R. Biswas and V. L. Dalal, "A photonic-plasmonic structure for enhancing light absorption in thin film solar cells," *Appl. Phys. Lett.* **99**, 131114 (2011).

6. R. Biswas and C. Xu, "Photonic and plasmonic crystal based enhancement of solar cells—Theory of overcoming the Lambertian limit," *J. Non-Cryst. Solids* **358**, 2289-2294 (2012).

7. J. Bhattacharya, N. Chakravarty, S. Pattnaik, W. D. Slafer, R. Biswas and V. Dalal, "Comparison of optical properties of periodic photonic–plasmonic and randomly textured back reflectors for nc-Si solar cells," *J. Non-Cryst. Solids* **358**, 2313-2318 (2012).

8. A. Peer and R. Biswas, "Nanophotonic organic solar cell architecture for advanced light trapping with dual photonic crystals," *ACS Photonics* **1**, 840-847 (2014).

9. J. You, X. Li, F.-X. Xie, W. E. I. Sha, J. H. W. Kwong, G. Li, W. C. H. Choy and Y. Yang, "Surface Plasmon and Scattering-Enhanced Low Bandgap Polymer Solar Cell by a Metal Grating Back Electrode," *Adv. Energy Mater.* 2, 1203-1207 (2012).

10. S. Pattnaik, N. Chakravarty, R. Biswas, V. Dalal and D. Slafer, "Nano-photonic and nano-plasmonic enhancements in thin film silicon solar cells," *Sol. Energy Mater. Sol. Cells* **129**, 115-123 (2014).

11. Y. Chen, M. Elshobaki, R. Gebhardt, S. Bergeson, M. Noack, J.-M. Park, A. C. Hillier, K.-M. Ho, R. Biswas and S. Chaudhary, "Reducing optical losses in organic solar cells using microlens arrays: theoretical and experimental investigation of microlens dimensions," *Phys. Chem. Chem. Phys.* **17**, 3723–3730 (2015).

12. Y. Chen, M. Elshobaki, Z. Ye, J.-M. Park, M. A. Noack, K.-M. Ho and S. Chaudhary, "Microlens array induced light absorption enhancement in polymer solar cells," *Phys. Chem. Chem. Phys.* **15**, 4297-4302 (2013).

13. A. Peer, R. Biswas, J.-M. Park, R. Shinar and J. Shinar, “Light management in perovskite solar cells and organic LEDs with microlens arrays,” *Opt. Express* **25**, 10704-10709 (2017).

14. S. A. Maier and H. A. Atwater, “Plasmonics: Localization and guiding of electromagnetic energy in metal/dielectric structures,” *J. Appl. Phys.* **98**, 10 (2005).

15. D. K. Gramotnev and S. I. Bozhevolnyi, “Plasmonics beyond the diffraction limit,” *Nat. Photon.* 4, 83-91 (2010).

16. J. A. Schuller, E. S. Barnard, W. S. Cai, Y. C. Jun, J. S. White and M. L. Brongersma, “Plasmonics for extreme light concentration and manipulation,” *Nat. Mater.* 9, 193-204 (2010).

17. S. A. Maier, M. L. Brongersma, P. G. Kik, S. Meltzer, A. A. G. Requicha and H. A. Atwater, “Plasmonics—A Route to Nanoscale Optical Devices,” *Adv. Mater.* 13, 1501-1505 (2001).

18. E. Ozbay, “Plasmonics: Merging Photonics and Electronics at Nanoscale Dimensions,” *Science* 311, 189-193 (2006).

19. K. R. Milner and C. A. Siedlecki, “Submicron poly (L-lactic acid) pillars affect fibroblast adhesion and proliferation,” *J. Biomed. Mater. Res. A* 82, 80-91 (2007).

20. Y. Zhu, C. Gao, Y. Liu and J. Shen, “Endothelial cell functions in vitro cultured on poly (L-lactic acid) membranes modified with different methods,” *J. Biomed. Mater. Res. A* 69, 436-443 (2004).

21. F. Badique, D. R. Stamov, P. M. Davidson, M. Veuillet, G. Reiter, J. N. Freund, C. M. Franz and K. Anselme, “Directing nuclear deformation on micropillared surfaces by substrate geometry and cytoskeleton organization,” *Biomaterials* 34, 2991-3001 (2013).

22. P. M. Davidson, H. Özçelik, V. Hasirci, G. Reiter and K. Anselme, “Microstructured Surfaces Cause Severe but Non-Detrimental Deformation of the Cell Nucleus,” *Adv. Mater.* 21, 3586-3590 (2009).

23. S. Shi, X. H. Wang, G. Guo, M. Fan, M. J. Huang and Z. Y. Qian, “Preparation and characterization of microporous poly (D, L-lactic acid) film for tissue engineering scaffold,” *Int. J. Nanomedicine* 5, 1049-1055 (2010).

24. C. Miller, H. Shanks, A. Witt, G. Rutkowski and S. Mallapragada, “Oriented Schwann cell growth on micropatterned biodegradable polymer substrates,” *Biomaterials* 22, 1263-1269 (2001).

25. G. E. Rutkowski, C. A. Miller, S. Jeftinija and S. K. Mallapragada, “Synergistic effects of micropatterned biodegradable conduits and Schwann cells on sciatic nerve regeneration,” *J. Neural Eng.* 1, 151-157 (2004).

26. L. Moroni and L. P. Lee, “Micropatterned hot-embossed polymeric surfaces influence cell proliferation and alignment,” *J. Biomed. Mater. Res. A* 88, 644-653 (2009).

27. S. K. Mallapragada, T. M. Brenza, J. M. McMillan, B. Narasimhan, D. S. Sakaguchi, A. D. Sharma, S. Zbarska and H. E. Gendelman, “Enabling nanomaterial, nanofabrication and cellular technologies for nanoneuromedicines,” *Nanomed. Nanotechnol. Biol. Med.* **11**, 715-729 (2015).

28. M. Uz, A. D. Sharma, P. Adhikari, D. S. Sakaguchi and S. K. Mallapragada, “Development of Multifunctional Films for Peripheral Nerve Regeneration,” *Acta Biomater.* **56**, 141-152 (2017).

29. M. E. Marti, A. D. Sharma, D. S. Sakaguchi and S. K. Mallapragada, “Nanomaterials for neural tissue engineering,” in *Nanomaterials in Tissue Engineering*, Woodhead Publishing Series in Biomaterials, 275-301 (2013).

30. E. J. Sandquist, M. Uz, A. D. Sharma, B. B. Patel, S. K. Mallapragada and D. S. Sakaguchi, “Stem Cells, Bioengineering, and 3-D Scaffolds for Nervous System Repair and Regeneration,” in *Neural Engineering: From Advanced Biomaterials to 3D Fabrication Techniques*, Springer International Publishing, 25-81 (2016).

31. A. D. Sharma, S. Zbarska, E. M. Petersen, M. E. Marti, S. K. Mallapragada and D. S. Sakaguchi, “Oriented growth and transdifferentiation of mesenchymal stem cells towards a Schwann cell fate on micropatterned substrates,” *J. Biosci. Bioeng.* **121**, 325-335 (2016).

32. H. Xu, H. Li and J. Chang, “Controlled drug release from a polymer matrix by patterned electrospun nanofibers with controllable hydrophobicity,” *J. Mater. Chem. B* 1, 4182-4188 (2013).

33. S. T. Yohe, Y. L. Colson and M. W. Grinstaff, “Superhydrophobic materials for tunable drug release: using displacement of air to control delivery rates,” *J. Am. Chem. Soc.* 134, 2016-2019 (2012).

34. K. H. Lo, M. C. Chen, R. M. Ho and H. W. Sung, “Pore-Filling Nanoporous Templates from Degradable Block Copolymers for Nanoscale Drug Delivery,” *ACS Nano* 3, 2660-2666 (2009).

35. Y. Xia, J. J. McClelland, R. Gupta, D. Qin, X.-M. Zhao, L. L. Sohn, R. J. Celotta and G. M. Whitesides, “Replica molding using polymeric materials: A practical step toward nanomanufacturing,” *Adv. Mater.* **9**, 147-149 (1997).

36. Y. Xia, J. A. Rogers, K. E. Paul and G. M. Whitesides, “Unconventional methods for fabricating and patterning nanostructures,” *Chem. Rev.* **99**, 1823-1848 (1999).

37. G. M. Whitesides, E. Ostuni, S. Takayama, X. Jiang and D. E. Ingber, “Soft lithography in biology and biochemistry,” *Annu. Rev. Biomed. Eng.* **3**, 335-373 (2001).

38. J. A. Rogers and R. G. Nuzzo, “Recent progress in soft lithography,” *Mater. Today* **8**, 50-56 (2005).

39. J. D. Joannopoulos, S. G. Johnson, J. N. Winn, and R. D. Meade, *Photonic Crystals: Molding the Flow of Light*, Princeton University Press, Princeton, 2011.

40. Z.-Y. Li and L.-L. Lin, “Photonic band structures solved by a plane-wave based transfer-matrix method,” *Phys. Rev. E* **67**, 046607 (2003).

CHAPTER 2

NANOPHOTONIC ORGANIC SOLAR CELL ARCHITECTURE FOR ADVANCED LIGHT TRAPPING WITH DUAL PHOTONIC CRYSTALS

Akshit Peer[1], Rana Biswas[1,2]

1. Department of Electrical and Computer Engineering, and Microelectronics Research Center, Iowa State University, Ames, IA, United States
2. Ames Laboratory, Department of Physics & Astronomy, and Microelectronics Research Center; Iowa State University, Ames, IA, United States

Adapted from an article published in *ACS Photonics* **1**, 843-847 (2014)

2.1 Abstract

Organic solar cells have demonstrated rapidly increasing efficiencies, but typically absorb less than half of the incident solar spectrum. To increase broad-band light absorption, we rigorously design experimentally realizable solar cell architectures based on dual photonic crystals using scattering matrix simulations. There is a polymer microlens on the glass coupled with a photonic-plasmonic crystal at the metal cathode on the back of the cell. The microlens focuses light on the periodic nanostructure that in turn strongly diffracts light. Waveguiding modes and surface plasmon modes enhance long wavelength absorption. The optimal architecture has a period of 500 nm for both arrays, resulting in absorption enhancement of 49% and photocurrent enhancement of 58% relative to the flat cell, for nearly lossless metal cathodes. The enhanced absorption approaches the Lambertian limit. Misalignment between the two photonic crystals leads to about 1% loss of performance.

Simulations incorporating experimental dielectric functions for metal cathode and ITO, using a real space methodology find the enhancement of 38% for the photocurrent and 36% for the weighted absorption, due to parasitic losses mainly in the metal cathode. This solar architecture is particularly amenable for fabrication since it does *not* require spin coating of organic layers on corrugated surfaces, but instead requires nano-imprinting an organic layer, followed by metal cathode deposition. This dual photonic crystal architecture has great potential to achieve >12% efficient single junction organic solar cells and to control photons by focusing light on nanostructures and plasmonic components.

2.2 Introduction

Organic solar cells (OSCs) have exhibited enormous progress with their power conversion efficiencies increasing from ~4% just 10 years ago to 11% recently [1] using novel low band gap polymers and tandem solar cells [2,3]. With these rapid advances, organic solar cells may overtake thin film amorphous silicon based cells. The preferred architecture of organic absorber layers is a bulk heterojunction, with an intimate blend of donor and acceptor material. Photocurrent generation involves photon absorption, exciton formation, exciton diffusion and dissociation at donor-acceptor interfaces, leading to charge separation and transport of electrons in the acceptor and holes in the donor, under internal electric fields to their respective electrodes.

Organic absorbers are limited in thickness [4] to ensure efficient carrier collection and to minimize carrier recombination, leading to thicknesses of ~200 nm for prototypical P3HT-PCBM blends and ~90-100 nm for the lower band gap PTB7 layers. At such thicknesses the absorption of light is incomplete both at long wavelengths (>600 nm) as well as at shorter wavelengths (<450 nm). Utilizing measured wavelength dependent refractive indices [5], photon absorption lengths are larger than the absorber layer thicknesses (Figure 2.1). Consequently, *more* than half of the incident solar photon flux is *not* absorbed.

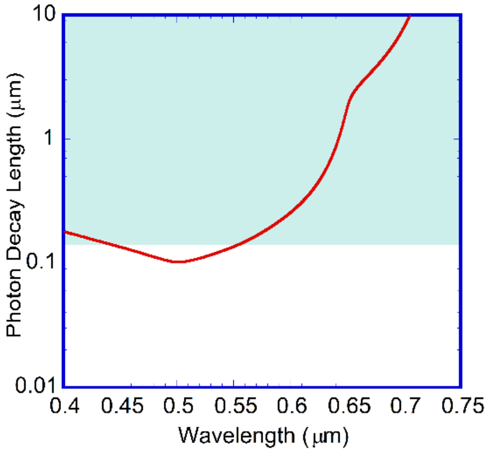

Figure 2.1. Decay length of photons as a function of wavelength utilizing measured wavelength dependent refractive indices [5] for the P3HT-PCBM blend. The blue color illustrates the regions where photon decay length exceeds 150 nm – a typical absorber layer thickness.

Various light management strategies using photonic and plasmonic structures have been proposed and studied for enhancing OSCs. One approach utilizes the metal nanoparticle (NPs) arrays in the electrode or absorber layer [6-14] to generate surface plasmon polaritons (SPPs) within the active layer. SPPs scatter light and enhance the electric field strongly in the active layer, thereby leading to increased light absorption. The incorporation of gold nanoparticles in the PEDOT:PSS as well as the absorber layer improved the efficiency of the polymer solar cell by ~22% [15], whereas Ag NPs in the PEDOT layer [16] enhanced efficiency from 6.4% to 7.6% (18% gain) in PCDTBT, through forward scattering effects of the NPs. Recently, organic absorber layers patterned with one-dimensional metal-grating back electrode showed an increase in the efficiency from ~7.2 to 7.73% due to field enhancement and scattering [17]. Simulations predicted ~23% absorption enhancement by patterning the organic absorber layer together with two-dimensional metal gratings [18]. OSCs on wrinkled substrates showed 47% enhancement of photocurrent with a 6-fold enhancement of quantum efficiency at long wavelengths [19] due to light-trapping [20]. A microlens combined with self-aligned micro-apertures increased the photocurrent from OSCs by 25% [21] by light-trapping.

We recently simulated a fully conformal organic solar cell with a periodically textured indium tin oxide (ITO) or PEDOT layer followed by organic layers and a cathode that conform to this textured substrate [22]. Such a conformal solar cell showed an absorption enhancement of 40% and a current enhancement of 50% for typical thicknesses (150-200 nm) of P3HT-PCBM layers. Although this prediction is very encouraging, there are severe practical problems to achieving such conformal cells. Spin coating an organic layer on a corrugated substrate is very challenging since material preferentially accumulates in the troughs of the structure [23]. Approaches to overcome this problem include reducing the corrugation height or increasing the pitch – but these reduce enhancement from optimal values.

We propose in this paper a *more practical* approach to light trapping in OSCs than the previous conformal solar cell [22]. Polymer microlens arrays can be readily fabricated by interference lithography [24] and positioned on the top of the glass substrate without altering the architecture or electrical characteristics of the OSC residing on the opposite face of the glass. Microlens arrays focus and diffract light within OSCs and increase out-coupling from OLEDs [24]. We then couple this microlens array with a periodically patterned organic layer with a periodic metal cathode to substantially enhance the photocurrent. Such patterned organic layers have been achieved by imprinting where a PDMS stamp was used to imprint an organic absorber layer with a one-dimensional pattern. A thin (8 nm) layer of MoO_3 followed by Ag cathode was grown on this structure resulting in a 1-dimensional grating cathode [17]. Two-dimensional gratings, offering higher diffraction enhancement, can be similarly imprinted immediately after spin-coating of the organic absorber. Hence we investigate the architecture (Figure 2.2) combining a patterned organic-cathode grating with a microlens on the exterior glass – both of which can be fabricated. The combination of the patterned cathode and the microlens has *not* been investigated theoretically or experimentally before. We rigorously optimize this solar architecture with simulations to predict a current enhancement of ~58% for this realizable structure.

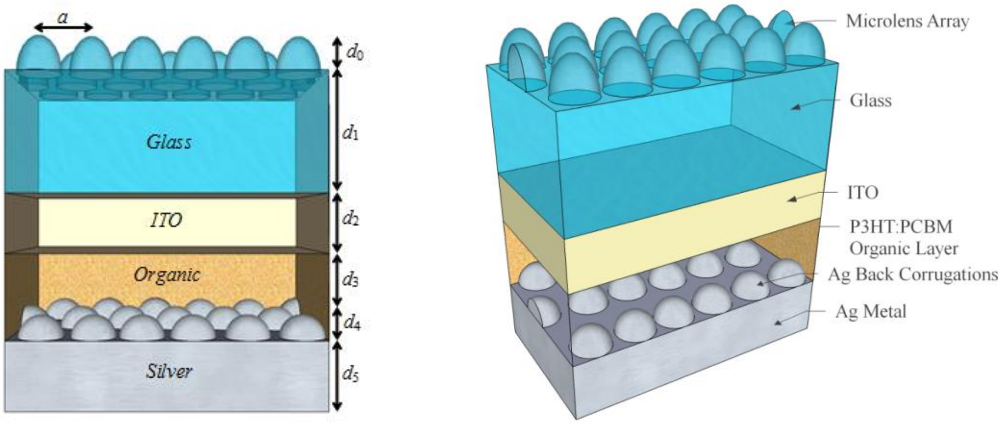

Figure 2.2. Schematic of the solar cell architecture. The heights of various layers are shown by the d_n where n denotes the subscript for the particular layer. The pitch of the microlens as well as the photonic crystal array is a. The figure is not drawn to scale.

2.3 Materials and Methods

The simulated solar cell architecture (Figure 2.2) has a thick glass substrate (thickness d_1), whose bottom side is coated with an ITO layer (thickness d_2). A triangular microlens array of conical pillars (height d_0) rests on top of the glass. In practice, there is a thin PEDOT:PSS layer (<30 nm) between the ITO and the organic absorber. We do not include the thin layer in our calculations since the optical properties of this layer are similar to ITO. We coat this with a P3HT-PCBM layer (thickness d_3) and a reflecting silver cathode. The organic-cathode interface has periodic corrugations in the form of conical pillars of base radius R and height d_4 in a triangular lattice. The microlens array and the cathode conical array have the same pitch (a). This architecture is suitable for regular organic solar cells, rather than inverted solar cells.

We use the rigorous scattering matrix (SM) method [22,25,26] where Maxwell's equations are solved in Fourier space, i.e. in a basis of plane waves for both polarizations. We divide the solar cell into slices in the z-direction wherein the dielectric function depends periodically on x and y. We obtain the SM for the entire structure by integrating the Maxwell's equations with continuity boundary conditions. The SM yields the total reflectance R (including diffraction), transmittance T (~0) and absorbance A (=1-R-T) at each wavelength. This SM technique has advantages over real-space methods of being able to simulate fully 3D geometries, without added memory requirements, since a real space grid is unnecessary. The SM method is fully parallelized with each frequency being sent to a different processor [22]. We characterize solar architectures by their broad-band weighted absorption $<A_W>$, weighted by the AM1.5 solar intensity $dI/d\lambda$, and the idealized short circuit current J_{SC}, where

$$< A_w >= \int_{\lambda_2}^{\lambda_1} A(\lambda) \frac{dI}{d\lambda} d\lambda, \tag{2.1}$$

$$J_{SC} = \frac{e}{hc} \int_{\lambda_2}^{\lambda_2} \lambda A(\lambda) \frac{dI}{d\lambda} d\lambda. \tag{2.2}$$

The spectral range of absorption is from λ_1=400 nm to λ_2=700 nm appropriate for P3HT-PCBM with a HOMO-LUMO splitting of 1.77 eV. Ideal internal quantum efficiency is assumed in simulations. We employ conical arrays in a triangular lattice, an architecture that yielded high enhancements in thin-Si solar cells [26,27,28]. Convergence was easily achieved with ~330 plane waves for each polarization, corresponding to a matrix size of 660. We utilize measured wavelength dependent refractive indices (*n*+i*k*) for ITO and Ag [22]. To compute the organic layer absorption only, we neglect ITO absorption, and use nearly ideal loss-less metal [22,29]. By adopting this approach, we consider the absorption of photons only in the active layer. The absorption of photons in any other layer cannot contribute to the photocurrent.

2.4 Results

A commensurate solar architecture can be achieved by the microlens array having the same pitch as the patterned organic-cathode interface. A critical factor governing light management and diffraction is the pitch of the structure, which we vary first. For a solar cell with just the microlens on top of the glass substrate and flat internal interfaces within the solar cell, we obtain a maximal enhancement of ~13% in both the absorption and the photocurrent, with an optimized pitch near 1.7 µm (Figure 2.3a). The enhancement is significantly smaller for smaller pitch, but decreases relatively slowly for larger pitch values. The microlens alone increases the absorption over all wavelengths but the amount of enhancement is limited.

In contrast, when we couple the microlens with a corrugated organic-cathode photonic crystal interface (Figure 2.2), the enhancement increases dramatically, reaching ~49% for the weighted absorption, and ~58% for the photocurrent (Figure 2.3a). The optimal pitch is ~500 nm, significantly smaller than for the microlens alone. The enhancement factor oscillates with a period near 200 nm, indicative of diffraction, and decreases rapidly for larger pitch, going *below* the performance for the microlens alone as *a* exceeds 1400 nm. Large pitch corrugations offer limited enhancement. We used an organic-cathode photonic crystal corrugation height of 90 nm (Figure 2.2), slightly smaller than the thickness of the uniform portion of the organic layer. The reference flat cells have the same volume of absorber material as in the corrugated cell, corresponding to 173 nm thickness of the flat cell. It should be noted that our all optical model predicts photocurrents which are in reasonable agreement with experimental measurements on flat cells with the same absorber layer thickness. For example, using our model we predict J_{SC} of 8.66 mA/cm^2 for a 150 nm thick cell, which is in very good agreement with the J_{SC} of 8.7 mA/cm^2 measured in [30] for the same cell thickness. The complex refractive index of the organic film does depend on spin coating and preparation conditions, which may lead to deviations from the predictions of our model.

The optimal pitch of 500 nm for the patterned solar cell is consistent with mode-coupling theories [31] that predict the optimal pitch to be slightly smaller than the wavelength region of interest over which light trapping is desired, which is the 600 - 700 nm wavelength region. The photocurrent enhancement exceeds that of the weighted absorption since the photocurrent preferentially weights the longer wavelengths (eqn. 2.2), where larger enhancements are found. We also find (Figure 2.3b) that even the periodic corrugations in organic-cathode interface alone result in enhancement of about 50% in J_{SC} and 40% in $<A_W>$ with an optimal a~500nm, indicating that surface plasmons and diffraction from the corrugated cathode are significant in enhancing the present solar cell architecture's performance.

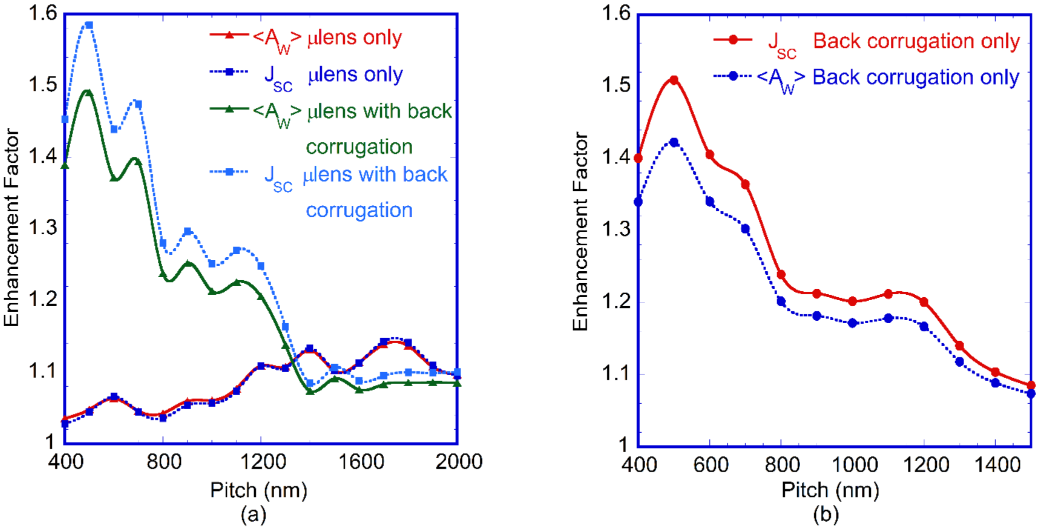

(a) (b)

Figure 2.3. (a) Enhancement in absorption and the photocurrent relative to a flat organic solar cell, as a function of the pitch (i) for the microlens alone and no corrugation in the organic-cathode interface, and (ii) with a microlens combined with photonic crystal array at the organic-cathode interface using a corrugation height of 90 nm in the cathode interface. For the combined array, the optimized microlens height and radii of the microlens as well as the photonic crystal array is 0.3 µm and 0.35*a* respectively. For the microlens only case, the optimized microlens height and radii of the microlens is 2.1 µm and 0.40*a* respectively. (b) Enhancement in absorption and the photocurrent relative to a flat organic solar cell, as a function of the pitch with only photonic crystal array at the organic-cathode interface using a corrugation height of 90 nm in the cathode interface. The optimized pitch and radii of the photonic crystal array is 500 nm and 0.35*a* respectively. The flat portion of the organic layer has a thickness d_3 = 100 nm in both cases. The line through the data points corresponds to the curve fit to guide the eye.

The presence of the microlens is important in determining the enhancement, with the pitch being a critical parameter and the microlens height being less important. The largest photocurrent (J_{SC}) obtained from the present architecture is 13.9 mA/cm^2, corresponding to ~58% enhancement in J_{SC} and 49% in <A_W> (Figure 2.4). For a fixed organic-cathode corrugation (d_4=90nm), the enhancement factor is relatively flat for microlens heights (d_0) in the range 0.3 - 1.0 µm. There is a weak minimum for d_0 ~1.3 µm, although the enhancement becomes nearly constant for larger heights (>1.5 µm). This suggests that although the microlens height is not a critical parameter in the design, the pitch is. This occurs since the pitch of the structure controls the diffraction whereas the lens height may shift the position of the focusing regions within the solar cell structure.

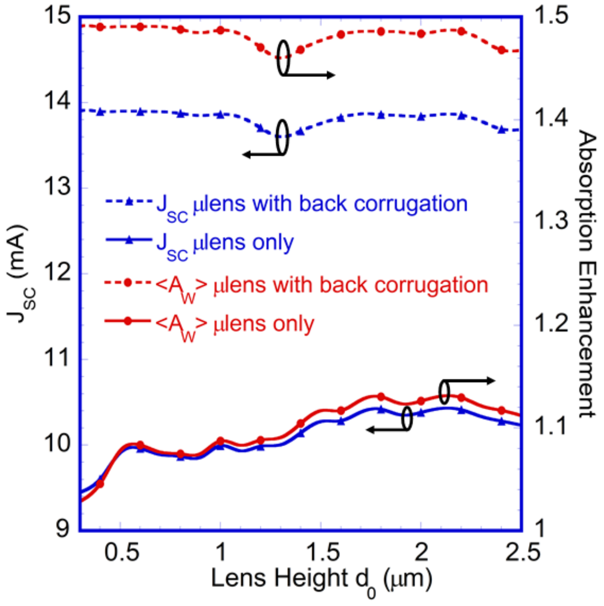

Figure 2.4. Enhancement in absorption and the photocurrent relative to a flat organic solar cell, as a function of the microlens height d_0 (i) for the microlens alone and no corrugation in the organic-cathode interface, and (ii) with a microlens combined with photonic crystal array at the organic-cathode interface using a corrugation height of 90 nm in the cathode interface. The optimized pitch value of 1700 nm was used for the microlens alone and 500 nm for the combined arrays. The optimized radii (*R*) of the microlens was 0.4*a* for the microlens alone and 0.35*a* in the combined array. The flat portion of the organic layer has a thickness d_3 = 100 nm in both cases. The line through the data points corresponds to the curve fit to guide the eye.

We simulated the weighted absorption as a function of the cone radius (*R/a*) for a fixed lens height of 0.3 μm (Figure 2.5). The conical pillars with a base radius *R* have the highest absorption when $R/a \cong 0.35$. This result is expected from analytic considerations since the scattering potential in this lattice is proportional to $2J_1(GR)/GR$, where J_1 is the first order Bessel function. For the triangular lattice, the lowest reciprocal lattice vector is $\mathbf{G_1} = (2\pi / a)(1, -1/\sqrt{3})$ and the largest scattering potential occurs near R/a~0.35 [22], corroborating the numerical results. Thus we choose *R*/*a* as 0.35 for all simulations.

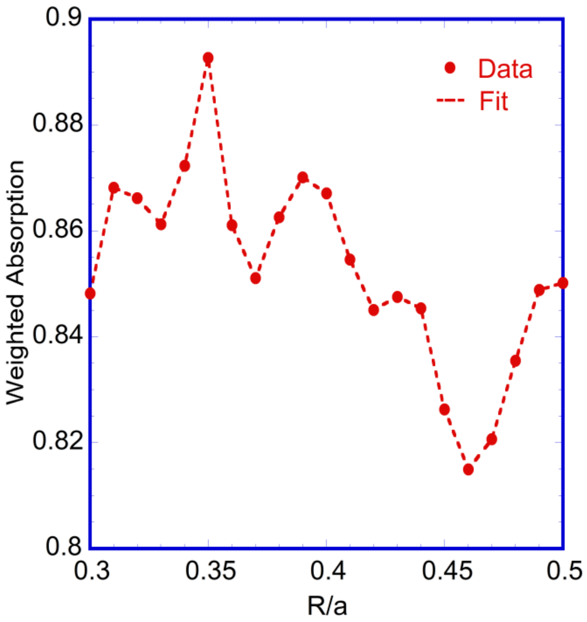

Figure 2.5. Weighted absorption as a function of R/a for solar cell with 90 nm corrugation in the Ag cathode and microlens of height 0.3 µm. The flat portion of the organic layer has a thickness d_3 = 100 nm and the pitch of the cell is 500 nm. The line through the data points corresponds to the curve fit to guide the eye.

We compare the absorptivity (Figure 2.6) of the flat and optimally corrugated solar cell (combining the microlens and PC array). We include the Lambertian limit [32] (Figure 2.6) where light is completely randomized, uniformly populating the photon phase space [33], and the path length of light is enhanced by a factor of $4n^2$ at each wavelength [34] (n is the λ-dependent refractive index). For organic materials, $4n^2$ is typically 12-15. The optimally corrugated solar cell has enhanced absorption over the flat case at all wavelengths, with largest gains (exceeding 10) at long wavelengths (>600nm). The absorption of the optimally corrugated cell has a maximum at 460 nm, and approaches the Lambertian limit between 420 nm – 500 nm and beyond 640 nm. Moreover, the enhanced absorption can be attributed to the maxima and minima of a dense mesh of resonant wave-guided modes that occur over wavelengths of interest. When the wave-guided modes propagate in the plane of the absorber, the round-trip phase difference from the top and bottom of the absorber layer is a multiple of 2π. The wave-vector perpendicular to the layers is $k_z = m\pi / d$ (*d* is the absorber layer thickness). For a triangular lattice, any reciprocal lattice vector **G** has components $i(2\pi / a)$ and $(2j-i)(2\pi / a)/\sqrt{3}$ respectively, where *i* and *j* are integers. Incident light with wave-vector $\mathbf{k}_{\|}$' is diffracted according to $\mathbf{k}_{\|}' = \mathbf{k}_{\|} + \mathbf{G}$. Since $k_z = m\pi/d$, and $\mathbf{k}_z^2 + \mathbf{k}_{\|}'^2 = n(\lambda)^2(\omega / c)^2$, wave-guiding occurs at resonant wavelengths given by:

$$\lambda(i, j, m) = \frac{2\pi n(\lambda)}{\left[\left(i^2 + \frac{1}{3}(2j-i)^2\right)\left(\frac{2\pi}{a}\right)^2 + \left(\frac{m\pi}{d}\right)^2\right]^{1/2}} \qquad (2.3)$$

where *i*, *j* and *m* are integers. A dense mesh of wave-guided modes occurs in the long λ region, for our choice of parameters. The phase coherence of waves is assumed at each interface.

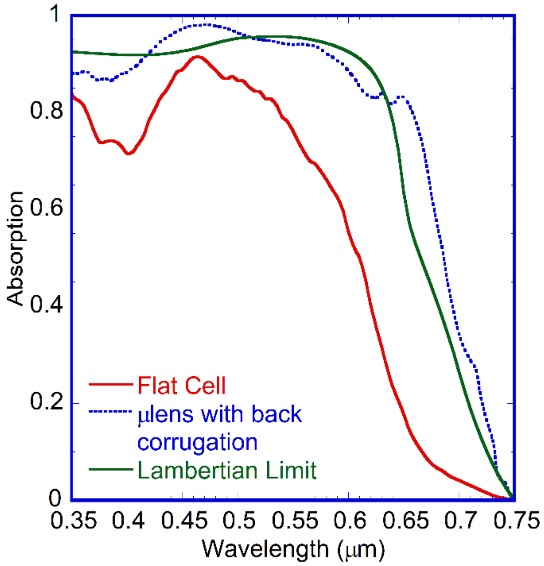

Figure 2.6. Absorption spectra of (i) a flat cell, (ii) a cell with microlens at the top and corrugation in the cathode, and (iii) the Lambertian limit. The optimized pitch, radii (*R*) of the microlens as well as the photonic crystal array, and the lens height are 500 nm, 0.35*a*, and 0.3 μm respectively.

Figure 2.7 illustrates the electric field intensity $|\mathbf{E}|^2$ in the cross section of the solar cell at a typical wavelength of 600 nm for the different optimized solar architectures. In the microlens with a corrugated cathode (Figure 2.7a), the microlens focuses the field in localized regions within the cell, near the organic – ITO interface, with an enhancement of ~2 in the field intensity. The lateral separation between the intensity maxima is the pitch. Previous ray-tracing simulations confirm focused regions within the absorber for microlenses combined with apertures [21]. As the pitch is increased, the lateral separation of focused spots increases. The microlens focuses light into the absorber layer, which is diffracted by the corrugated cathode. The intensity variations in the absorber also indicate wave-guided modes that propagate in the plane of the structure. Surface plasmons, propagating in the plane of the structure, are generated at the periodically textured metal cathode, resulting in the maximum enhancement in the field intensity by ~2.5 near the organic-metal interface (Figure 2.7a), at the sides of the conical metal nano-pillars, as expected from surface plasmon fields. The lower n ~ 1.7 of organics reduces the intensity enhancements as compared to thin silicon solar architectures with corrugated back reflectors [26], due to the much higher silicon n (~3.5).

When the organic cathode interface is corrugated without the microlens (Figure 2.7b), we find surface plasmon formation at this interface without the focusing regions caused by the microlens. The surface plasmons propagate in the plane of the structure generating enhanced absorption. Diffraction from the organic-cathode grating also generates wave-guided modes. For the configuration with only a top microlens array (Figure 2.7c) and flat solar cell layers, there are narrow highly focused regions where the intensity is enhanced by ~10 within the organic layer, significantly larger than for the microlens with organic-cathode grating. Outside these regions there is no intensity enhancement. Propagating surface plasmons and wave-guided modes are absent.

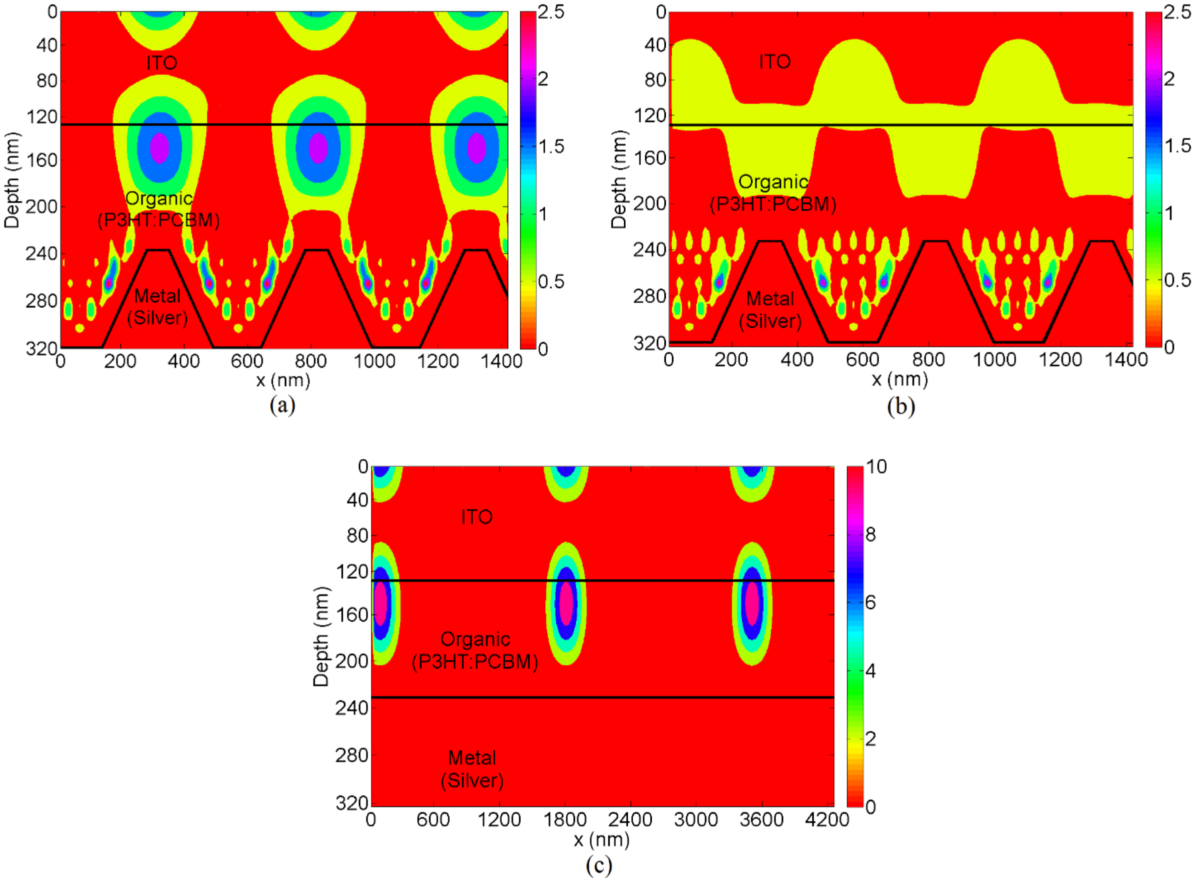

(a) (b)

(c)

Figure 2.7. Electric field intensity in the cross-section of the solar cell at 600 nm wavelength (a) with microlens of height 0.3 µm, (b) without the microlens, and (c) with microlens alone (height = 2.1 µm). The optimized pitch value of 1700 nm was used for the microlens alone and 500 nm for the combined arrays. The optimized radii (*R*) of the microlens was 0.4*a* for the microlens alone and 0.35*a* in the combined array.

2.5 Discussion

The microlens array produces a succession of standing wave maxima and minima in the underlying dielectric layers, ending with the boundary conditions of vanishing electric field in the metal. The expected separation between nodes (minima) is λ/2*n* which for a free-space λ=600 nm and a typical organic *n*~1.7, is ~176 nm. From Figure 2.7a, this separation is

~170 nm, very close to the theoretical prediction. The maxima of the standing waves occur at a separation of $\lambda/4n$ from the metal cathode, which is ~88 nm and located near the interface between the organic and ITO layer.

The fabrication of this architecture requires the microlens to be commensurate with the corrugated cathode, having the same pitch (Figure 2.2). There could be unavoidable misalignment while experimentally positioning the microlens on the glass. To investigate the effect of lens misalignment on the performance, we simulated the variation in enhancement factor when the microlens array is shifted along a symmetry axis (*x*-direction) with respect to corrugated organic-metal cathode by varying amounts (Figure 2.8). Misalignment only reduces the enhancement factor by <1% (Figure 2.8). The largest misalignment of 250 nm occurs when the top microlens is exactly in the troughs of the corrugated cathode resulting in only ~0.9% decrease in *J*sc and <Aw> in comparison to the perfectly aligned structure. The enhancement ratio is symmetric about the 250 nm shift, due to the structural periodicity (with pitch 500 nm). Hence the structure is not sensitive to typical fabrication constraints of the thin microlens placement, and the robustness of this design is appealing for fabrication – an advantage over designs combining microlens arrays with micro-apertures [21] – where precise alignment is necessary.

The regions of high intensity $|\mathbf{E}|^2$ within the absorber lead to high exciton concentration in locally inhomogeneous regions within the absorber. High exciton densities near the ITO-organic interface promote hole collection at the ITO, whereas excitons near the cathode from surface plasmons benefit electron collection. The quenching of excitons close to the metal cathode has been studied previously. To reduce the exciton quenching near the cathode thin (~10 nm) exciton blocking layers have been employed [35]. Such thin layers will not affect the optical absorption processes studied here. The e- and h-transport is an aspect for further work.

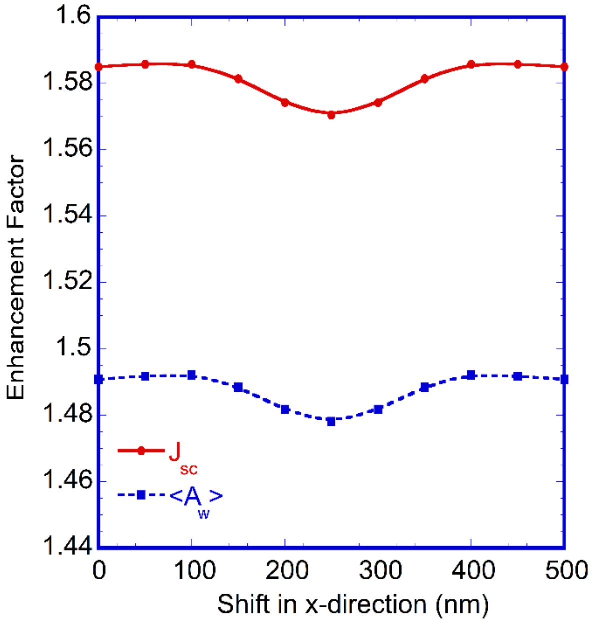

Figure 2.8. Enhancement in photocurrent and weighted absorption when the microlens is shifted in *x*-direction with respect to the conical corrugations in the Ag cathode. The optimized values of pitch, radii (*R*) of the microlens as well as the photonic crystal array, and the lens height are 500 nm, 0.35*a*, and 0.3 µm respectively.

Periodic patterning of conformal thin silicon solar cells has achieved >30% measured enhancements [27] and are a promising direction for organic cells. OSCs on quasi-periodic wrinkled polymer substrates [19] show measured photocurrent enhancements as large as 47% due to light trapping similar to those for periodic structures. Very recently moth-eye structures with two photonic patterns have shown to enhance the performance of OLEDs [36]. The photocurrent enhancements of 58% found here, imply that the state of the art 8% efficient *single junction* organic solar cell could be improved to ~12% efficiency with optimal light management, competitive with thin film silicon cells. Light trapping may be employed for tandem organic cells which could increase their efficiency even further, and may lead to >15% efficiency tandem cells, competitive with current thin film technologies.

2.6 Parasitic Losses

One of the critical questions is the magnitude of the parasitic losses within (i) the metal cathode and (ii) within the ITO layer, and it is essential to assess whether the enhancements are still valid when all these parasitic losses are accounted for. To address this question, we repeat our calculations for the realistic ITO, as well as the metal cathode where $n_2 = \mathrm{Im}(n) \neq 0$ and is given by experimental measurements. With such calculations, the wavelength dependent absorption A(l) from the optical simulation includes contributions from the ITO and metal cathode. To deconvolute the contribution of the absorption from only the organic material, it is necessary to extract the electric fields $\boldsymbol{E}(\mathbf{r})$ and magnetic fields $\boldsymbol{H}(\mathbf{r})$ in *real* space by transforming the computed fields in Fourier space. The absorption rate R per unit volume at the position **r** is

$$R = \frac{1}{8\pi}\omega \,\mathrm{Im}\left(\varepsilon(\omega)\right)\left|E(r)\right|^2 \qquad (2.4)$$

The absorption A is then

$$A = \frac{1}{V}\int \frac{4\pi n_1 n_2}{\lambda}\left|E(x,y,z)\right|^2 dxdydz \qquad (2.5)$$

where the integral is only over the organic material of volume V. The absorption is proportional to the imaginary component of the refractive index $n_2 = \mathrm{Im}(n)$. In the mixed grating layer, the sum is only over the organic layer material – a procedure that is computationally intensive since it involves the geometry of the nano-cones.

Such a procedure is computationally laborious and not well suited for the present scattering matrix method where Maxwell's equations are solved in *Fourier space rather than real space*. In fact, such procedures are more amenable to real space solvers such as the finite difference time domain (FDTD) method. The use of Fourier space has great advantages for parallelization and computational efficiency at the expense of not directly calculating the real space fields and separating the losses. Nonetheless, we have implemented this procedure of extracting the real space fields and we separately calculate the losses *only* in the organic material, with each simulation taking about 1600 CPU hours in a multi-processor environment utilizing 64 processors.

This procedure yields an enhancement of 38% for J_{SC} and 36% for $<A_W>$ for the pitch (a) = 600 nm and R/a = 0.39 – the optimum geometry for solar architecture with absorption in the metal *and* ITO included. This enhancement is somewhat lower than the (J_{SC}, $<A_W>$) enhancement values of (58%, 49%) for the ideal case due to the parasitic absorption in the ITO as well as the metal cathode for both the flat reference and textured cases. We plot the enhancement ratio as a function of the pitch (Figure 2.9) which shows a maximum for pitch of 600 nm – a trend similar to that for the ideal case (Figure 2.3). The principal difference is that the peak enhancement at small pitch (600 nm) including parasitic absorption is lower than the ideal case. Similar to the ideal case, the enhancement factor shows an oscillatory behavior, with a value ~1.3 for the larger pitch values around 1000-1300 nm. This indicates that structures with periodicity around 1 μm, which are more amenable to fabrication, provide enhancements near 30%, and may also be suitable. As in the ideal case, the enhancement factor decreases for pitch values larger than 1500 nm. Notably the enhancement of $<A_W>$ can be slightly larger than that of J_{SC} for pitch values around 900 nm.

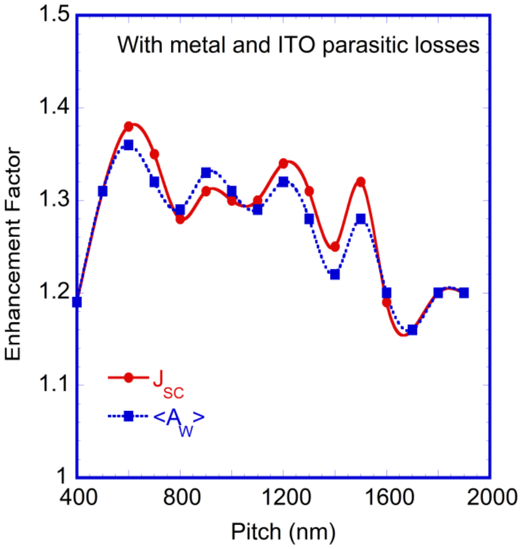

Figure 2.9. Simulated enhancements as a function of pitch including the losses in both metal cathode and ITO layers. The enhancement in absorption and the photocurrent is relative to a flat organic solar cell, for a solar cell with a microlens combined with photonic crystal array at the organic-cathode interface using a corrugation height of 90 nm in the cathode interface. The optimized microlens height and radii of the microlens as well as the photonic crystal array is 0.3 µm and 0.39*a* respectively. The line through the data points corresponds to the curve fit to guide the eye.

By performing calculations with the Im(*n*) to be equal to experimental value, we find the ITO absorption to be less than 1% of the total absorption, whereas the parasitic absorption in the metal cathode is much more significant with a value ~10%.

2.7 Conclusion

The fundamental advance in this paper is that advanced photonic structures can tremendously enhance photon harvesting in organic solar cells through strong diffraction and waveguide modes in conjunction with plasmonic light concentration. We demonstrate experimentally realizable organic solar cell architecture with a periodically textured microlens array on the top of the glass substrate in conjunction with a periodically corrugated metal cathode. This solar architecture is amenable to fabrication since it does *not* require spin coating of organic layers on corrugated surfaces. It instead requires imprinting an organic layer, followed by metal cathode deposition. The optimized architecture has a period of 500 nm for both arrays, resulting in absorption enhancement of 49% and photocurrent enhancement of 58% relative to the flat cell, with much enhanced absorption at long wavelengths. The absorption approaches the Lambertian limit. By performing the simulations for realistic metal and ITO by a real space methodology, the enhancement was 38% for photocurrent and 36% for weighted absorption due to parasitic losses mainly in the metal cathode. The high enhancement in absorption can be attributed to the patterned metal cathode that diffracts light and generates propagating surface plasmons which enhance the field intensity at the organic-metal interface. The microlens at the top of the glass substrate focuses the light within the organic absorber layer and further enhances the plasmonic effects. The present solar cell architecture is a unique and practical way to control the light interaction with nanostructures and it has great potential to achieve >12% efficiency for *single junction* organic solar cells.

2.8 Acknowledgements

This research was partially supported by the Ames Laboratory, operated for the Department of Energy (theoretical analysis) by Iowa State University under contract No. DE-AC02-07CH11385; and the National Science Foundation through grant ECCS-1232067 (computational work). The research used resources at the National Energy Research Scientific Computing Center (NERSC) which is supported by the Office of Science of the USDOE under Contract No. DE-AC02-05CH11231. We thank A. Moule for providing experimental data.

2.9 References

1. J. You, L. Dou, K. Yoshimura, T. Kato, K. Ohya, T. Moriarty, K. Emery, C.-C. Chen, J. Gao, G. Li and Y. Yang, "A polymer tandem solar cell with 10.6% power conversion efficiency," *Nat. Commun.* **4**, 1446-1455 (2013).

2. S. H. Park, A. Roy, S. Beaupre´, S. Cho, N. Coates, J. S. Moon, D. Moses, M. Leclerc, K. Lee and A. J. Heeger, "Bulk heterojunction solar cells with internal quantum efficiency approaching 100%," *Nat. Photonics* **3**, 297-303 (2009).

3. L. Dou, J. You, J. Yang, C.-C. Chen, Y. He, S. Murase, T. Moriarty, K. Emery, G. Li and Y. Yang, "Tandem polymer solar cells featuring a spectrally matched low-bandgap polymer," *Nat. Photonics* **6**, 180-185 (2012).

4. T. Soga, *Nanostructured Materials for Solar Energy Conversion*, Elsevier Science, Amsterdam, 2006.

5. A. J. Moule and K. Meerholz, "Interference method for the determination of the complex refractive index of thin polymer layers," *Appl. Phys. Lett.* **91**, 061901 (2007).

6. H. A. Atwater and A. Polman, "Plasmonics for improved photovoltaic devices," *Nat. Mater.* **9**, 205-213 (2010).

7. S.-S. Kim, S.-I. Na, J. Jo, D.-Y. Kim and Y.-C. Nah, "Plasmon enhanced performance of organic solar cells using electrodeposited Ag nanoparticles," *Appl. Phys. Lett.* **93**, 073307 (2008).

8. A. J. Morfa, K. L. Rowlen, T. H. Reilly III, M. J. Romero, J. van de Lagemaat, "Plasmon-enhanced solar energy conversion in organic bulk heterojunction photovoltaics," *Appl. Phys. Lett.* **92**, 013504 (2008).

9. D. Duche, P. Torchio, L. Escoubas, F. Monestier, J.-J. Simon, F. Flory and G. Mathian, "Improving light absorption in organic solar cells by plasmonic contribution," *Sol. Energy Mater. Sol. Cells* **93**, 1377-1382 (2009).

10. H. Shen, P. Bienstman and B. Maes, "Plasmonic absorption enhancement in organic solar cells with thin active layers," *J. Appl. Phys.* **106**, 073109 (2009).

11. S. Vedraine, P. Torchio, D. Duche´, F. Flory, J.-J. Simon, J. L. Rouzo and L. Escoubas, "Intrinsic absorption of plasmonic structures for organic solar cells," *Solar Energy Mater. Sol. Cells* **95**, S57-S64 (2011).

12. S. Shahin, P. Gangopadhyay and R. A. Norwood, "Ultrathin organic bulk heterojunction solar cells: Plasmon enhanced performance using Au nanoparticles," *Appl. Phys. Lett.* **101**, 053109 (2012).

13. Q. Gan, F. J. Bartoli and Z. H. Kafafi, "Plasmonic Enhanced Organic Photovoltaics: Breaking the 10% Efficiency Barrier," *Adv. Mater.* **25**, 2385-2396 (2013).

14. Z. Ouyang, S. Pillai, F. Beck, O. Kunz, S. Varlamov, K. R. Catchpole, P. Campbell and M. A. Green, “Effective light trapping in polycrystalline silicon thin-film solar cells by means of rear localized surface plasmons,” *Appl. Phys. Lett.* **96**, 261109 (2010).

15. F.-X. Xie, W. C. H. Choy, C. C. D. Wang, W. E. I. Sha and D. D. S. Fung, “Improving the efficiency of polymer solar cells by incorporating gold nanoparticles into all polymer layers,” *Appl. Phys. Lett.* **99**, 153304 (2011).

16. S.-W. Baek, J. Noh, C.-H. Lee, B. Kim, M.-K. Seo and J.-Y. Lee, “Plasmonic Forward Scattering Effect in Organic Solar Cells: A Powerful Optical Engineering Method,” *Sci. Rep.* **3**, 1726 (2013).

17. J. You, X. Li, F.-X. Xie, W. E. I. Sha, J. H. W. Kwong, G. Li, W. C. H. Choy and Y. Yang, “Surface Plasmon and Scattering-Enhanced Low Bandgap Polymer Solar Cell by a Metal Grating Back Electrode,” *Adv. Energy Mater.* **2**, 1203-1207 (2012).

18. K. Q. Le, A. Abass, B. Maes, P. Bienstman and A. Alù, “Comparing plasmonic and dielectric gratings for absorption enhancement in thin-film organic solar cells,” *Opt. Express* **20**, A39-A50 (2012).

19. J. B. Kim, P. Kim, N. C. Pe´gard, S. J. Oh, C. R. Kagan, J. W. Fleischer, H. A. Stone and Y.-L. Loo, “Wrinkles and deep folds as photonic structures in photovoltaics,” *Nat. Photonics* **6**, 327-332 (2012).

20. B. Gregg and J. van de Lagemaat, “Solar cells: Folding photons,” *Nat. Photonics* **6**, 278-280 (2012).

21. K. Tvingstedt, S. D. Zilio, O. Inganäs and M. Tormen, “Trapping light with micro-lenses in thin film organic photovoltaic cells,” *Opt. Express* **16**, 21608-21615 (2008).

22. R. Biswas and E. Timmons, “Nano-photonic light trapping near the Lambertian limit in organic solar cell architectures,” *Opt. Express* **21**, A841-A846 (2013).

23. K. S. Nalwa, J.-M. Park, K.-M. Ho and S. Chaudhary, “On Realizing Higher Efficiency Polymer Solar Cells Using a Textured Substrate Platform,” *Adv. Mater.* **23**, 112-116 (2011).

24. J.-M. Park, Z. Gan, W. Y. Leung, R. Liu, Z. Ye, K. Constant, J. Shinar, R. Shinar and K.-M. Ho, “Soft holographic interference lithography microlens for enhanced organic light emitting diode light extraction,” *Opt. Express* **19**, A786-A792 (2011).

25. Z.-Y. Li and L.-L. Lin, “Photonic band structures solved by a plane-wave based transfer-matrix method,” *Phys. Rev. E* **67**, 046607 (2003).

26. R. Biswas and C. Xu, “Nano-crystalline silicon solar cell architecture with absorption at the classical 4n2 limit,” *Opt. Express* **19**, A664-A672 (2011).

27. J. Bhattacharya, N. Chakravarty, S. Pattnaik, W. D. Slafer, R. Biswas and V. L. Dalal, “A photonic-plasmonic structure for enhancing light absorption in thin film solar cells,” *Appl. Phys. Lett.* **99**, 131114 (2011).

28. K. S. Nalwa and S. Chaudhary, “Design of light-trapping microscale-textured surfaces for efficient organic solar cells,” *Opt. Express* **18**, 5168-5178 (2010).

29. D. Zhou and R. Biswas, “Photonic crystal enhanced light-trapping in thin film solar cells,” *J. Appl. Phys.* **103**, 093102 (2008).

30. J. Bhattacharya, R. W. Mayer, M. Samiee and V. L. Dalal, “Photo-induced changes in fundamental properties of organic solar cells,” *Appl. Phys. Lett.* **100**, 193501 (2012).

31. Z. Yu, A. Raman and S. Fan, “Fundamental limit of nanophotonic light trapping in solar cells,” *Proc. Natl. Acad. Sci. U.S.A* **107**, 17491-17496 (2010).

32. E. Yablonovitch, “Statistical ray optics,” *J. Opt. Soc. Am.* **72**, 899-907 (1982).

33. E. A. Schiff, “Thermodynamic limit to photonic-plasmonic light-trapping in thin films on metals,” *J. Appl. Phys.* **110**, 104501 (2011).

34. T. Tiedje, E. Yablonovitch, G. D. Cody and B. G. Brooks, “Limiting efficiency of silicon solar cells,” *IEEE Trans. Electron Dev.* **31**, 711-716 (1984).

35. P. Peumans, V. Bulović and S. R. Forrest, “Efficient photon harvesting at high optical intensities in ultrathin organic double heterostructure photovoltaic diodes,” *Appl. Phys. Lett.* **76**, 2650 (2000).

36. L. Zhou, Q.-D. Ou, J.-D. Chen, S. Shen, J.-X. Tang, Y.-Q. Li and S.-T. Lee, “Light Manipulation for Organic Optoelectronics Using Bio-inspired Moth’s Eye Nanostructures,” *Sci. Rep.* **4**, 4040 (2014).

CHAPTER 3

LIGHT MANAGEMENT IN PEROVSKITE SOLAR CELLS AND ORGANIC LEDs WITH MICROLENS ARRAYS[†]

Akshit Peer[1,2], Rana Biswas[1,2,3], Joong-Mok Park[1], Ruth Shinar[2] and Joseph Shinar[1,2,3]

1. Ames Laboratory, Ames, IA 50011, USA
2. Microelectronics Research Center, and Department of Electrical and Computer Engineering, Iowa State University, Ames, IA 50011, USA
3. Department of Physics and Astronomy, Iowa State University, Ames, IA 50011, USA

Adapted from an article published in *Optics Express* **25**, 10704-10709 (2017)

3.1 Abstract

We demonstrate enhanced absorption in solar cells and enhanced light emission in OLEDs by light interaction with a periodically structured microlens array. We simulate n-i-p perovskite solar cells with a microlens at the air-glass interface, with rigorous scattering matrix simulations. The microlens focuses light in nanoscale regions within the absorber layer enhancing the solar cell. Optimal period of ~700 nm and microlens height of ~800-1000 nm, provides absorption (photocurrent) enhancement of 6% (6.3%). An external polymer microlens array on the air-glass side of the OLED generates experimental and theoretical enhancements >100%, by outcoupling trapped modes in the glass substrate.

[†] Measurements on organic LEDs were carried out by Dr. Joong-Mok Park.

3.2 Introduction

Periodically structured materials can interact with light in unusual ways that can serve as a new platform for enhancing many optoelectronic devices. We describe polymer microlens array structures that can enhance perovskite solar cell photocurrents and light emission from organic light emitting diodes (OLEDs).

In the area of solar cells, methyl ammonium lead iodide ($MAPbI_3$) type perovskite solar cells (PSCs) have attracted enormous interest from the photovoltaic community due to their rapidly increasing efficiency from ~12% in 2013 to > 22% in 2016 [1]. Although the perovskite material has very high absorption coefficient and solar cells made of thin layers of ~300-400 nm thickness absorb light very effectively, there is still considerable loss in light absorption at ~440-480 nm, ~550-650 nm, and near the band edge ~700-800 nm [2–5]. Most PSC research has focused on improving the efficiency by modifying the materials and/or their underlying properties, the processing techniques, and different transport layers.

Very recently, few light management schemes to enhance the performance of PSCs have emerged. Incorporation of periodic inverted cones in the perovskite layer simulated 6% absorption enhancement (25.1 mA/cm^2) compared to the Lambertian limit (23.7 mA/cm^2) [6]. Inverted pyramid cones with Bragg-stack reflectors have also been proposed to theoretically enhance the performance of perovskite/c-Si tandem solar cells in recent reports [7,8]. In another study, texturing the front surfaces and back reflector showed that the maximum photocurrent enhancement is found for 97 nm thick absorber layers [9], thinner than in the common PSCs. Incorporating nano-dendrites in the TiO_2 electron transport layer experimentally showed 22% and 25% enhancements in the average photocurrent and power conversion efficiency (PCE) respectively compared to the TiO_2 nanorods due to enhanced light trapping [3]. The localized plasmon resonances of metallic nanoparticles have been utilized extensively to enhance the performance of PSCs [4,5,10,11]. For instance, the addition of Au-Ag alloy popcorn-shaped nanoparticles increased the PCE from 8.9% to 10.3%, whereas the core-shell Ag/TiO_2 increased the PCE from 14.5% to 16.3%, due to plasmonic effects. However, Snaith et al. reported increase in PCE from 10.7% to 11.4% by incorporating core-shell gold nanoparticles due to the lowering of the exciton dissociation energy from ~100 meV to ~35 meV, rather than enhanced light absorption [12].

In this paper, we implement an experimentally realizable microlens-based light trapping scheme for a PSC where a microlens array (MLA) can be attached to the glass side of the solar cell *without affecting* the internal absorbing layers. We use rigorous scattering matrix simulations to optimize the solar cell architecture. The MLA-based light trapping is easier to implement due to the ease of fabrication over large-areas (>1 $inch^2$) using the roll-to-roll nanoimprint lithography approach. It does not involve disturbing the internal layers which might affect the change transport and synthesis procedures adversely. In our previous work, the P3HT- and PTB7-based organic solar cells with MLAs have been successful in yielding enhancement of ~12% in photocurrent [13]. In a recent report, quasi-periodic microstructured hole transport layer with conformal Au cathode showed enhanced light harvesting in thin 240 nm PSCs with PCE of 17.7% [2]. Although internal texturing of the absorber layer shows greater promise for enhancement, the deposition on corrugated substrates is very challenging.

3.3 Simulation Methodology

We use the rigorous scattering matrix (SM) method [14,15] where Maxwell's equations are solved in Fourier space, in a basis of plane waves for both polarizations, to obtain the total reflectance R (including diffracted beams) and transmission T (which is 0) at each incident wavelength. The absorption at each wavelength is then $A = 1 - R - T$ as described previously [16]. We characterize solar architectures by their broad-band absorption $<A_w>$, weighted by the AM1.5 solar intensity d*I*/d*l*, and the idealized short circuit current J_{sc}, where

$$< A_w >= \int_{\lambda_1}^{\lambda_2} A(\lambda) \frac{dI}{d\lambda} d\lambda, \tag{3.1}$$

$$J_{SC} = \frac{e}{hc} \int_{\lambda_1}^{\lambda_2} \lambda A(\lambda) \frac{dI}{d\lambda} d\lambda \tag{3.2}$$

The spectral range of absorption for PSC with a bandgap of ~1.6 eV is from λ_1=350 nm to λ_2=800 nm. Ideal internal quantum efficiency is assumed in simulations.

3.4 Results and Discussion

3.4.1 Perovskite solar cells

We simulate a standard n-i-p device architecture with layers stacked as glass/FTO/TiO_2/perovskite/Spiro-OMeTAD/Au shown in Figure 3.1a. The thickness of glass, FTO, TiO_2, Spiro, and Au are fixed at 700 mm, 300 nm, 40 nm, 250 nm and 100 nm, respectively, similar to typical experimental values. The measured complex refractive index (n_1+in_2) values for FTO, TiO_2, Spiro [17] and perovskite [18] are taken from the literature. The wavelength-dependent photon decay length (ζ) for perovskite calculated using $\zeta(\lambda)$ =

$l/4\pi n_2(\lambda)$ is plotted in Figure 3.1b, where n_2 is the imaginary part of the measured perovskite complex refractive index.

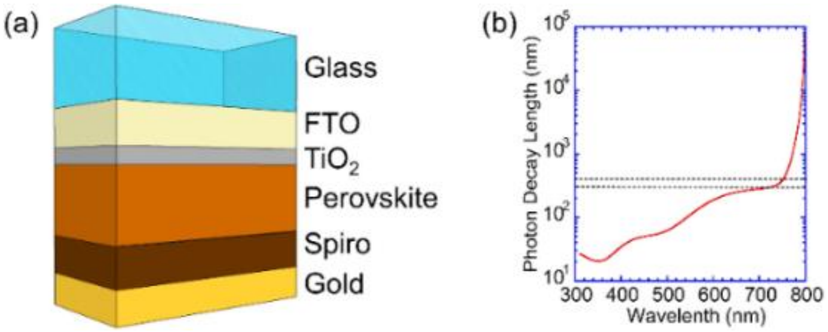

Figure 3.1. (a) Schematic of PSC architecture without MLA. (b) Photon decay length of perovskite.

We first show the variation in J_{SC} with the perovskite layer thickness in Figure 3.2a, where Jsc increases until perovskite layer thickness reaches ~400 nm and nearly saturates for thicknesses exceeding 400 nm. The J_{SC} variation with thickness is in agreement with results previously reported in the literature [17]. Consequently, we employ the perovskite layer thickness of ~400 nm in the rest of our simulations, consistent with the experiments reported in the literature for efficient charge collection in PSCs.

The variation of J_{SC} with absorber layer thickness can be fitted well using the function:

$$J_{SC}(x) = J_{SC,\max}(1 - e^{-\frac{x}{\zeta}}), \tag{3.3}$$

where $J_{SC,\max} = 21\ \mathrm{mA/cm^2}$ and z is the photon decay length. We plot *ln* $(1-J_{SC}(x)/J_{SC,\max})$ as a function of x which must be approximately a straight line, as shown in Figure 3.2b. The slope of the line $1/\zeta = 6.21 \times 10^{-3}\ \mathrm{nm}^{-1}$ gives the decay parameter $\zeta \sim 161$ nm. The decay parameter corresponds well to the wavelength-averaged photon decay length for the perovskite absorber material calculated using $\zeta(\lambda) = l/4\pi n_2(\lambda)$, with measured n_2 of perovskite [18].

Figure 3.2c shows that the absorption spectra for 400 nm thick perovskite layer has >90% absorption at all wavelengths except for λ ~ 450-550 nm and 600-700 nm where it falls to ~80%, and can be improved by incorporating a microlens.

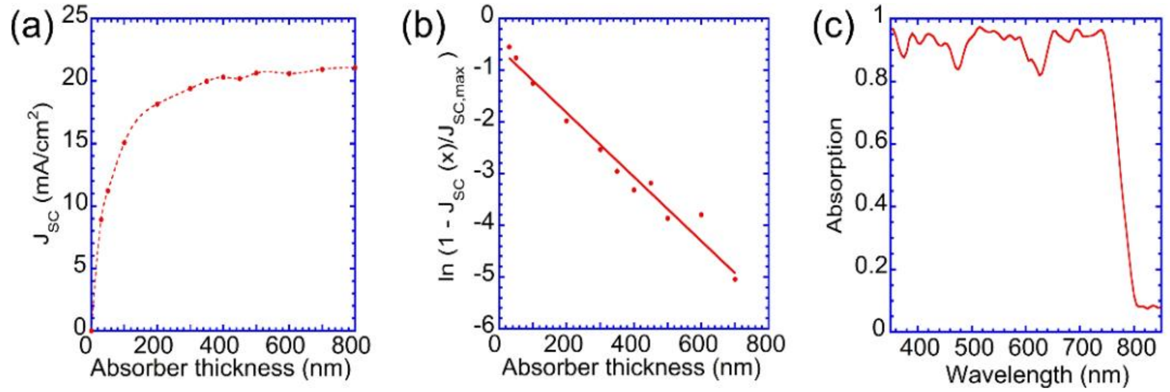

Figure 3.2. (a) Variation of photocurrent (J_{SC}) as a function of perovskite layer thickness. (b) *ln* ($1-J_{SC}/J_{SC,\ max}$) as a function of perovskite layer thickness. (c) Simulated absorption as a function of wavelength for 400 nm thick perovskite absorber layer.

The MLA can easily be fabricated on an ITO/FTO-coated glass substrate using nanoimprint lithography as described in our previous publication [19]. A typical polymer (e.g. polystyrene, polyurethane) index-matched to glass is spin-coated on a thick glass substrate. The polymer is then stamped using a PDMS mold replicated from a flexible master pattern under the effect of temperature and pressure. The PDMS mold is then released to reveal the inverse of the PDMS pattern on the polymer surface.

Figure 3.3a shows the atomic force microscopy (AFM) image of a representative MLA fabricated in polystyrene using the nanoimprinting process. As shown in Figure 3.3a, the AFM image illustrates the well-defined microlens array arranged in triangular lattice with the period ~750 nm. The AFM line scan confirms the height of microlens to be ~120 nm. The

MLA period and height can be conveniently changed by starting with a master pattern having different geometrical parameters (e.g. periodicity, height, depth). Figure 3.3b illustrates the diffraction pattern generated due to the MLA when it is normally illuminated with the white light source from the glass side. The diffraction pattern is collected on a sheet of paper normal to the glass surface, and is imaged using a digital camera.

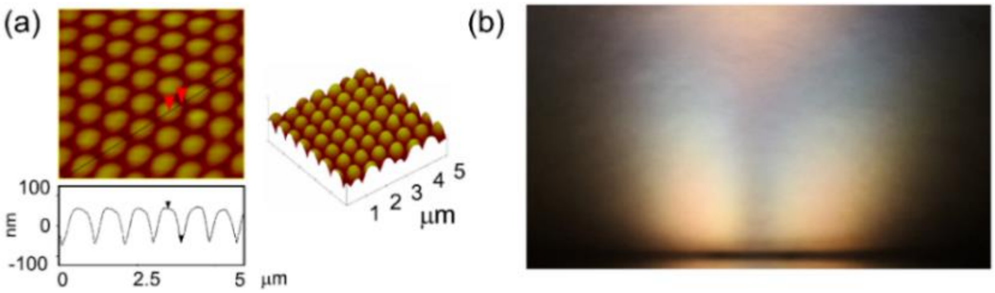

Figure 3.3. (a) AFM image of the MLA. The inset illustrates AFM line scan showing the height of the microlens ~120 nm. The right panel shows three-dimensional view of the MLA. (b) The diffraction pattern from the MLA when illuminated with white light.

We now couple the MLA on the air-glass side of the PSC, as schematically shown in Figure 3.4a. We optimize the period (*a*) and height (*h*) of the MLA for the solar cell architecture, through simulation. For each period the optimal lens height is determined and we plot the enhancement as a function of MLA period in Figure 3.4b. The photocurrent enhancement is highest (~6.3%) for MLA period *a*~700 nm with height *h*~800 nm for *a*/*h* ratio ≈ 1. Shallower heights (~500nm) decrease the enhancement by ~1%. The optimal period is in the range of band-edge wavelengths where light trapping is needed [20]. The optimal period of ~700 nm agrees well with our previous calculations for thin silicon [21] and organic solar cells [16]. There is a second maximum of MLA pitch ~1300 nm exhibiting ~5% enhancement, as shown in Figure 3.4b. Figure 3.4c shows absorption for the solar cell without MLA and with MLA of optimal period ~700 nm and height ~800 nm, showing absorption enhancement for the MLA-based device at all wavelengths, with high enhancements at 440-480 nm, 550-650 nm, and beyond ~780 nm, relative to without the MLA. The enhancement is due to light focusing by the MLA. Narrow waveguiding modes are evident above 800 nm. Figure 3.4d illustrates the electric field intensity distribution at λ = 550 nm inside the PSC with the top MLA with high intensity enhancement by a factor >2.5 inside the absorber layer, resulting in enhanced absorption and photocurrent in solar cell. Regions of maximum field intensity occur directly above the MLA and are separated in *x*-direction by the MLA period ~700 nm. The positions of field maxima with enhancement ~3.5 (red regions) residing mostly in FTO region, are separated by ~100 nm in *z*-direction indicating the formation of standing waves, where maxima are separated by $l/2n_{FTO}$ (~140 nm). Similar standing-waves were observed in our previous results on organic [16] and silicon [15,22] solar cells. Most of the enhanced field intensity does not lie deep inside the perovskite absorber layer but stays near the perovskite-TiO_2 interface. This is due to the high index of the perovskite layer and most of the electric field intensity absorbed near the FTO-perovskite interface, especially at shorter wavelengths.

3.4.2 Organic light emitting diodes

MLAs have also been greatly beneficial in enhancing OLEDs. In OLEDs the fraction of the outcoupled light is only ~17-20% in the absence of extraction measures. This is due to several loss paths within the device, such as photons trapped in the substrate due to total internal reflection (TIR) at the glass (*n* ~1.5)/air interface, photons waveguided in the high index organic (*n* ~1.7-1.8) + anode (often ITO, *n* ~1.8-2.1) layers, and photons dissipated at the organic/metal cathode by surface plasmon excitation. While recapturing all photons for useful emission remains a challenge, the use of a microlens array provides a solution for mitigating the loss due to TIR at the substrate/air interface.

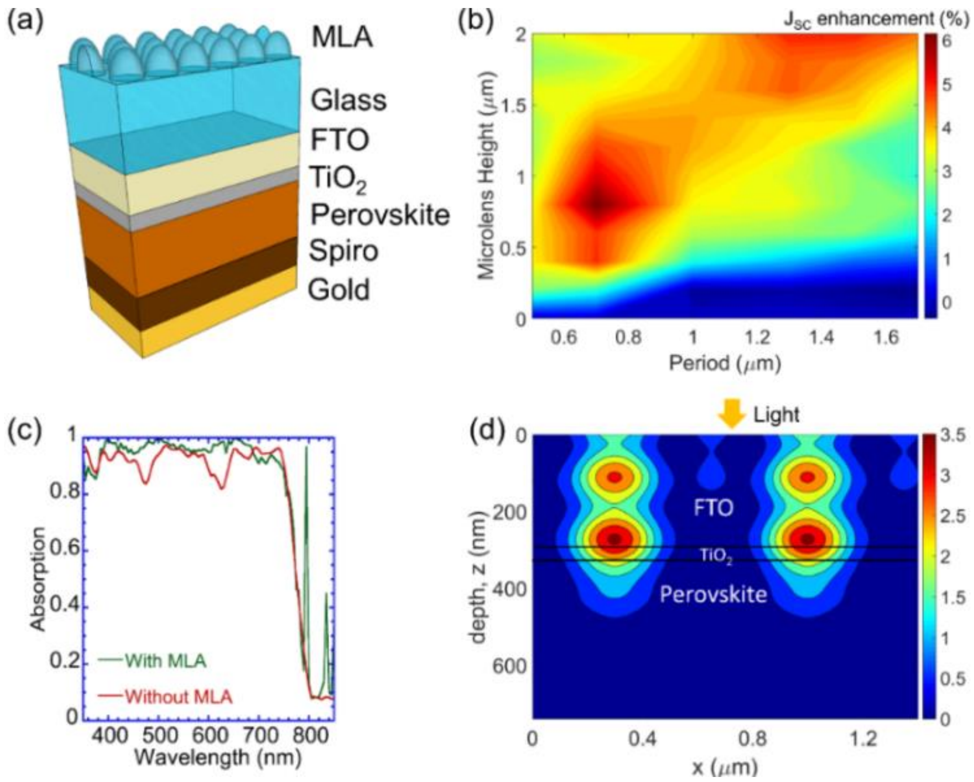

Figure 3.4. (a) Schematic of PSC architecture showing stacking of different layers with MLA on air-glass side. (b) 2D plot showing optimal microlens height as a function of period. (c) Absorption as a function of wavelength for solar cell with MLA of *a* ~ 700nm and *h* ~ 800nm. The absorption of flat solar cell without MLA is overlaid for comparison. (d) Electric field intensity plot for the PSC with MLA *a* ~ 800nm and *h* = 700nm at l = 550nm.

Figure 3.5a shows the effect of attaching a uniform 2 μm-period, 1.6 μm diameter, and 1.2 μm height polyurethane microsphere MLA to the opposite (blank) side of a 1.1 mm thick glass substrate on which the OLED pixels were fabricated. The MLA was fabricated using soft lithography whose advantages include ease of fabrication of large area designs with very ordered and uniform patterns. To achieve the observed maximal (~100%) enhancement in the forward electroluminescence, the array size (15x15 mm^2) was ~25 fold that of the pixel (3x3 mm^2). This approach avoids confining the microlens to an area directly under the pixel, which typically results in a lower enhancement, measured in green and blue OLEDs based on Al (Alq3) and DPVBi, respectively [23].

The square-shaped, sharp pixel shown in Figure 3.5a is devoid of the microlens array. The defocused green and blue images are of pixels in which the light scatters through the MLA. That spreading light demonstrates that the MLA actually extracts light from the glass substrate, outside the pixel area. Figure 3.5b shows measured intensity increases with the size of the collection region surrounding the pixel, with an enhancement of ~50% for a 10 mm opening diameter of an integrating sphere and >100% for a 25 mm opening diameter. Figure 3.5c shows that the power efficiency and luminous efficiency (L) are enhanced by ~100% with the MLA over the shown range of voltages, with peak efficiencies near 6V. We observed additionally that pixels adjacent to those with a MLA also contribute to the enhanced light extraction. A similar enhancement in light extraction was obtained in simulations as shown in Figure 3.5d, showing higher enhancement (>100%) for a microlens considerably larger than the small source. We also obtained an enhancement of ~60% in the OLEDs' electroluminescence by easily forming thin microporous films on the blank side of the glass substrate [24]. Micropores that scatter light are formed from phase separation of the blends' constituents during film drying process.

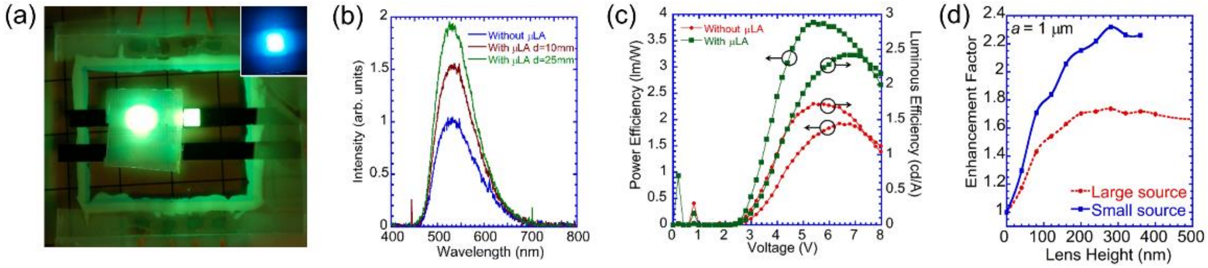

Figure 3.5. (a) Light emission from green and blue OLEDs, using a MLA on the air-glass side. The pixel on the right is devoid of such an array and its emission is ~2 fold lower in comparison to the other. (b) Spectral emission of the green OLED without and with MLA collected with different integrating sphere opening diameter *d* = 10, 25 mm. (c) Power efficiency and luminous efficiency of green OLED without and with MLA. (d) Simulated enhancement factor as a function of lens height for smaller and larger size source as compared to 1mm-period MLA.

3.5 Conclusion

We show that MLA-based light management scheme for PSCs and OLEDs can enhance their performance significantly. This scheme is particularly useful since large-area scalable manufacturing of MLA is possible and the lens array can be placed external to the actual device without disturbing the internal active layers which can affect the electronic properties. External MLAs can enhance absorption and photocurrent in perovskite solar cells by >6%, through light focusing within the active layer. In OLEDs external MLAs larger than the pixel size show measured light extraction enhancement >100% by reducing waveguided modes in the substrate and collecting light outside the pixel area.

3.6 Funding

Ames Laboratory, operated for the U. S. Department of Energy (DOE) by Iowa State University (Contract No. DE-AC02-07CH11385); National Energy Research Scientific Computing Center (NERSC), Office of Science, U.S. DOE (Contract No. DE-AC02-05CH11231).

3.7 References

1. “Best Research Cell Efficiencies,” National Renewable Energy Laboratory.
2. M. Long, Z. Chen, T. Zhang, Y. Xiao, X. Zeng, J. Chen, K. Yan and J. Xu, “Ultrathin efficient perovskite solar cells employing a periodic structure of a composite hole conductor for elevated plasmonic light harvesting and hole collection,” *Nanoscale* **8**, 6290–6299 (2016).
3. S.-H. Lin, Y.-H. Su, H.-W. Cho, P.-Y. Kung, W.-P. Liao and J.-J. Wu, “Nanophotonic Perovskite Solar Cell Architecture with Three-Dimensional TiO_2 Nanodendrite Scaffold for Light Trapping and Electron Collection,” *J. Mater. Chem. A* **4**, 1119–1125 (2016).

4. S. Carretero-Palacios, M. E. Calvo and H. Míguez, “Absorption Enhancement in Organic-Inorganic Halide Perovskite Films with Embedded Plasmonic Gold Nanoparticles,” *J. Phys. Chem. C* **119**, 18635–18640 (2015).

5. Z. Lu, X. Pan, Y. Ma, Y. Li, L. Zheng, D. Zhang, Q. Xu, Z. Chen, S. Wang, B. Qu, F. Liu, Y. Huang, L. Xiao and Q. Gong, “Plasmonic-enhanced perovskite solar cells using alloy popcorn nanoparticles,” *RSC Adv.* **5**, 11175-11179 (2015).

6. Q. G. Du, G. Shen and S. John, “Light-trapping in perovskite solar cells,” *AIP Adv.* **6**, 065002 (2016).

7. B. W. Schneider, N. N. Lal, S. Baker-Finch and T. P. White, “Pyramidal surface textures for light trapping and antireflection in perovskite-on-silicon tandem solar cells,” *Opt. Express* **22**, A1422–A1430 (2014).

8. D. Shi, Y. Zeng and W. Shen, “Perovskite/c-Si tandem solar cell with inverted nanopyramids: realizing high efficiency by controllable light trapping,” *Sci. Rep.* **5**, 16504 (2015).

9. S. M. Iftiquar and J. Yi, “Numerical simulation and light trapping in perovskite solar cell,” *J. Photon. Energy* **6**, 025507 (2016).

10. M. Saliba, W. Zhang, V. M. Burlakov, S. D. Stranks, Y. Sun, J. M. Ball, M. B. Johnston, A. Goriely, U. Wiesner and H. J. Snaith, “Plasmonic-Induced Photon Recycling in Metal Halide Perovskite Solar Cells,” *Adv. Funct. Mater.* **25**, 5038–5046 (2015).

11. H.-L. Hsu, T.-Y. Juang, C.-P. Chen, C.-M. Hsieh, C.-C. Yang, C.-L. Huang and R.-J. Jeng, “Enhanced efficiency of organic and perovskite photovoltaics from shape-dependent broadband plasmonic effects of silver nanoplates,” *Sol. Energy Mater. Sol. Cells* **140**, 224–231 (2015).

12. W. Zhang, M. Saliba, S. D. Stranks, Y. Sun, X. Shi, U. Wiesner and H. J. Snaith, “Enhancement of Perovskite Based Solar Cells Employing Core-shell Metal Nanoparticles,” *Nano Lett.* **13**, 4505-4510 (2013).

13. Y. Chen, M. Elshobaki, R. Gebhardt, S. Bergeson, M. Noack, J.-M. Park, A. C. Hillier, K.-M. Ho, R. Biswas and S. Chaudhary, “Reducing optical losses in organic solar cells using microlens arrays: theoretical and experimental investigation of microlens dimensions,” *Phys. Chem. Chem. Phys.* **17**, 3723–3730 (2015).

14. Z.-Y. Li and L.-L. Lin, “Photonic band structures solved by a plane-wave-based transfer-matrix method,” *Phys. Rev. E* **67**, 46607 (2003).

15. R. Biswas and C. Xu, “Nano-crystalline silicon solar cell architecture with absorption at the classical 4n2 limit,” *Opt. Express* **19**, A664–A672 (2011).

16. A. Peer and R. Biswas, “Nanophotonic Organic Solar Cell Architecture for Advanced Light Trapping with Dual Photonic Crystals,” *ACS Photonics* **1**, 840–847 (2014).

17. J. M. Ball, S. D. Stranks, M. T. Hörantner, S. Hüttner, W. Zhang, E. J. W. Crossland, I. Ramirez, M. Riede, M. B. Johnston, R. H. Friend and H. J. Snaith, “Optical properties and limiting photocurrent of thin-film perovskite solar cells,” *Energy Environ. Sci.* **8**, 602–609 (2015).

18. P. Löper, M. Stuckelberger, B. Niesen, J. Werner, M. Filipic, S.-J. Moon, J.-H. Yum, M. Topic, S. De Wolf and C. Ballif, “Complex Refractive Index Spectra of $CH_3NH_3PbI_3$ Perovskite Thin Films Determined by Spectroscopic Ellipsometry and Spectrophotometry,” *J. Phys. Chem. Lett.* **6**, 66–71 (2015).

19. A. Peer and R. Biswas, “Extraordinary optical transmission in nanopatterned ultrathin metal films without holes,” *Nanoscale* **8**, 4657–4666 (2016).

20. Z. Yu, A. Raman and S. Fan, “Fundamental limit of nanophotonic light trapping in solar cells,” *Proc. Natl. Acad. Sci. U. S. A.* **107**, 17491–17496 (2010).

21. S. Pattnaik, N. Chakravarty, R. Biswas, V. Dalal and D. Slafer, “Nano-photonic and nano-plasmonic enhancements in thin film silicon solar cells,” *Sol. Energy Mater. Sol. Cells* **129**, 115–123 (2014).

22. P. Pathi, A. Peer and R. Biswas, “Nano-photonic structures for light trapping in ultra-thin crystalline silicon solar cells,” *Nanomaterials* **7**, 17 (2017).

23. J.-M. Park, Z. Gan, W. Y. Leung, R. Liu, Z. Ye, K. Constant, J. Shinar, R. Shinar and K.-M. Ho, “Soft holographic interference lithography microlens for enhanced organic light emitting diode light extraction,” *Opt. Express* **19**, A786-792 (2011).

24. R. Liu, Z. Ye, J.-M. Park, M. Cai, Y. Chen, K.-M. Ho, R. Shinar, and J. Shinar, “Microporous phase-separated films of polymer blends for enhanced outcoupling of light from OLEDs,” *Opt. Express* **19**, A1272-1280 (2011).

CHAPTER 4

EXTRAORDINARY OPTICAL TRANSMISSION IN NANOPATTERNED ULTRATHIN METAL FILMS WITHOUT HOLES

Akshit Peer[1,3] and Rana Biswas[1,2,3]

1. Department of Electrical and Computer Engineering, Iowa State University, Ames, Iowa 50011, USA
2. Department of Physics and Astronomy, Iowa State University, Ames, Iowa 50011, USA
3. Ames Laboratory, Ames, Iowa 50011, USA

Adapted from an article published in *Nanoscale* **8**, 4657-4666 (2016)

4.1 Abstract

We experimentally and theoretically demonstrate that a *continuous* gold film on a periodically textured substrate exhibits extraordinary optical transmission, even though no holes were etched in the film. Our film synthesis started by nanoimprinting a periodic array of nanocups of period ~750 nm on a polystyrene film over a glass substrate. A thin *non-conformal* gold film was sputter-deposited on the polystyrene with angle-directed deposition. The gold film was continuous with spatial thickness variation, the film being thinnest at the bottom of the nanocup. Measurements revealed an extraordinary transmission peak at a wavelength just smaller than the period, with an enhancement of ~2.5 as compared to the classically expected value. Scattering matrix simulations model well the transmission and reflectance measurements when an ultrathin gold layer (~5 nm), smaller than the skin depth, is retained at the bottom of the nanocups. Electric field intensities are enhanced by >100

within the nanocup, and ~40 in the ultrathin gold layer causing transmission through it. We show a wavelength red-shift of ~30 nm in extraordinary transmission peak when the nanocups are coated with a thin film of few nanometers, which can be utilized for biosensing. The continuous corrugated metal films are far simpler structures to observe extraordinary transmission, circumventing the difficult process of etching the metal film. Such continuous metal films with ultrathin regions are simple platforms for non-linear optics, plasmonics, and biological and chemical sensing.

4.2 Introduction

The seminal discovery of extraordinary transmission in sub-wavelength hole arrays by Ebbesen et al. [1] spurred an immense body of activity in sub-wavelength optics [2,3], plasmonics [4,5] and sensing [6,7]. It is very well established that a sub-wavelength array of holes in a free standing thin metal film, exhibits an extraordinary transmission peak at a wavelength (λ) close to array period (a) i.e. $\lambda \sim a$. When the hole array in the metal film resides on a substrate of refractive index n, there is an is an additional transmission peak at the wavelength $\lambda \sim na$. At both peaks the transmission is dramatically enhanced over the expected classical value [8] for the area of holes, with the enhancement increasing for smaller holes. The sub-wavelength holes do not allow transmission of classical waveguided modes. Rigorous studies established that the excitation of surface plasmon modes on both surfaces of the metal film and their coupling to each other underlies the physics of the extraordinary transmission (EOT) phenomena [9].

Experimental demonstration of EOT has typically involved *complex* multistep lithographic processes on thin metal films, with two approaches. A common approach employed for *small area* hole arrays, typically less than 1mm^2, is to utilize photolithography for patterning and reactive ion etching (RIE) or focused ion-beam (FIB) milling for etching the arrays on thin metal films on substrates [10-13]. The optical properties of such small scale structures can only be measured with microspectrophotometers. The microspectrophotometer is a complex setup combining optical microscope with a sensitive spectrophotometer, and is used to measure the optical spectra of small area samples such as hole arrays [14,15] and patterned structures [16,17] non-destructively. The reflected, transmitted, or emitted light from the sample is collected either by the objective lens of the microscope or through optical fibers and focused on the spectrophotometer aperture for measurement. The microscope can be integrated with spectrophotometer to do measurement in UV-Vis-NIR region or infrared region (FTIR microscopy).

Alternatively patterning can be achieved by optical lithography performed with an elaborate projection lithography procedure, utilizing ultraviolet exposure, where a pattern on a reticle can be reduced (e.g. by a factor ~4) and transferred to photoresist, followed by reactive ion-etching to produce hole arrays [18]. In either case the fabrication involves advanced microelectronics facilities and procedures, and is difficult to implement for larger area samples. Previously metal coated self-assembled polystyrene spheres [19] exhibited transmission peaks due to waveguide modes within the photonic crystal slab, but these experiments relied on fabrication of self-assembled monolayers.

We demonstrate a particularly simpler method to fabricate a subwavelength array structure using simple soft-lithographic procedures that does not require any nanofabrication facilities, and may be easily achieved in a workbench without high vacuum facilities. Moreover we demonstrate that a simple deposition of *continuous* metal film on a patterned substrate can exhibit EOT phenomena, without the need for etching features in the metal film – which is a particularly complex step. It seems counterintuitive that there are no holes in our deposited films, but the EOT relies instead on thickness variations of the metal film.

4.3 Experimental

4.3.1 Fabrication

The corrugated metal films were fabricated by the steps schematically depicted in Figure 4.1a. We started with a master pattern (Microcontinuum Inc.) consisting of a periodic array of tapered nanocups (radius ~ 250 nm) with sub-micron period (~750 nm) patterned on a polycarbonate substrate by lithographic techniques, and a roll-to-roll process. Such master patterns and imprint stamps at customizable period and nanocup depth can also be commercially purchased from vendors [20], without the need for in-house nanofabrication. The inverse of this pattern on polycarbonate was transferred to a polydimethylsiloxane (PDMS) mold by soft lithography techniques [21] (*see PDMS Mold Preparation*). We used the patterned PDMS mold to transfer the pattern onto polystyrene (PS) films by first spin-coating PS films on a glass substrate and then imprinting the PS film with the PDMS mold, under elevated pressure and temperature (*see Polystyrene Film Preparation and Nanoimprinting*). Polystyrene is an excellent choice for the substrate since it is optically very well matched to the glass. Large area hole arrays have been fabricated by similar soft lithographic methods for enhanced thin film solar cells [22].

The patterned PS films were then sputter-coated (Denton, Desk V HP) with gold. We initially coated ~3nm iridium on the samples to increase the adhesion of thin gold layers on PS films. For sputtering the films, glass slides with the nanopatterned films were positioned at ~45° from the horizontal in the sputter chamber and rotated along the vertical axis so as to obtain highly non-conformal coating over the nanocup arrays (Figure 4.1a). This procedure is especially effective in coating the sidewalls of the arrays such that the metal coating is thicker at the top of the sidewall (~100 nm) and gradually becomes thinner as we move towards the bottom of nanocup sidewall (Figure 4.1b). The bottom of the nanocup has an ultrathin gold coating (estimated at ~5 nm) that is smaller than the skin depth of gold ($\frac{\lambda}{2\pi\,\mathrm{Im}(n)} \sim$ 25-30 nm) at optical wavelengths. Our deposition process ensures that the gold films are continuous. No further etching of the films was performed.

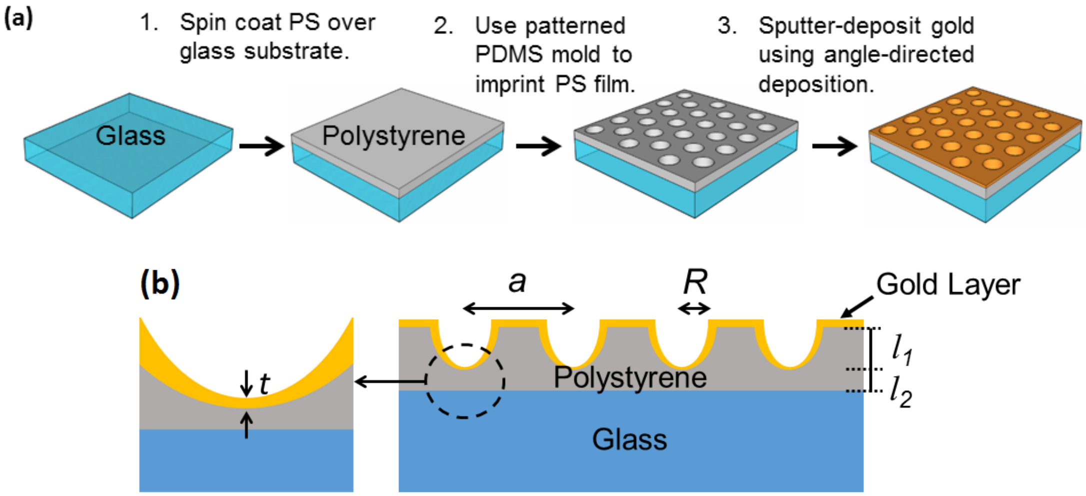

Figure 4.1. (a) Schematic illustrating imprinting the tapered nanocups on spin-coated polystyrene over glass substrate and subsequent gold deposition. (b) Cross sectional view of the gold-coated imprinted polystyrene surface with tapered nanocups. The magnified view of the encircled region is shown in left. The thickness of ultrathin gold layer at the bottom of the nanocup is *t*. l_1 is the imprint depth and l_2 is the thickness of polystyrene between the nanocup and glass substrate.

4.3.2 PDMS mold preparation

PDMS was prepared by mixing the elastomer base and curing agent (Sylgard 184, Dow Corning) in 10:1 w/w ratio. The mixture was degassed to remove any air bubbles. The mixture was then poured directly onto the master substrate with nanopatterns. After curing at room temperature for ~48 hours and subsequent heating on a hotplate at 65°C for ~12 hours, the PDMS was peeled off from the master substrate to expose the inverse pattern on the PDMS surface. The transferred pattern was characterized by scanning electron microscopy (SEM).

4.3.3 Polystyrene film preparation and nanoimprinting

For preparing the PS films, polystyrene (Sigma Aldrich, average MW 35,000) was dissolved in toluene to form solutions with 2%, 5% and 10% w/v concentration. The PS solution with different concentrations was spin-coated on the glass substrate (500 rpm, 60 seconds) to form thin films of different thicknesses, varying from 0.26 μm to 9 μm (Table 4.1). After allowing the films to dry for ~12 hours, the PDMS stamp was placed on each of the PS films over the glass substrate so that the patterned PDMS stamp faces the PS film. The PDMS stamp was further pressed down by another glass slide having the same size as substrate, and the assembly was held together with two binder clips at each end. The whole assembly was placed on a hotplate at 165°C, a temperature higher than the glass transition temperature (T_g) of PS (~100°C), for 45 minutes. After allowing it to cool at room temperature for 12 hours, the PDMS stamp was removed carefully from the PS films to reveal the inverse replica of the pattern on it. The thickness of the films obtained after spin-coating different concentrations of PS solution was measured using a Filmetrics F20 thin-film thickness measurement. The patterned nanocup array on PS films was characterized using SEM. All the samples were sputtered with ~3 nm iridium before SEM.

4.4 Results

4.4.1 Film characterization

For solutions of concentrations 2%, 5%, and 10%, the measured film thicknesses were 0.265 ± 0.002 µm, 0.839 ± 0.012 µm, and 2.245 ± 0.041 µm, respectively. The measured PS film thicknesses were consistent with the data reported elsewhere [23]. The thickness of films over the glass substrate with different concentrations of PS solution is listed in Table 4.1.

Table 4.1. Thickness of polystyrene films for solutions of different concentrations.

Concentration (w/v)	**Thickness (µm)**
2%	0.265 ± 0.002
3%	0.369 ± 0.002
4%	0.569 ± 0.009
5%	0.839 ± 0.012
10%	2.245 ± 0.041
20%	9.014 ± 0.052

Figure 4.2a-4.2c shows the SEM images of the gold-coated patterned PS films for 2%, 5%, and 10% solution concentrations, respectively. The images show the regular array of tapered nanocups with a period of ~750 nm. The images demonstrate that the radius (*R*) of cups at the surface of the film fabricated using 2% PS solution is the smallest, and as a result the inter-cup spacing is largest. The nanocup radius increases and the depth decreases as the PS solution concentration increases from 2% to 10%. This yields three films with the same period (*a*) but different radius to period (*R*/*a*) ratio. The difference in R/*a* and nanocup imprint depth (l_1) can be ascribed to difference in film thickness and PS concentration – the 2% PS film is thin (~265 nm) and thus the stamp cannot penetrate completely into the film to

replicate exactly the same radius of features as is on the stamp. However, at the same time, the stamp also has difficulty penetrating deep into the higher concentration PS film predominantly resulting in shallower features as the PS concentration increases from 2% to 10%.

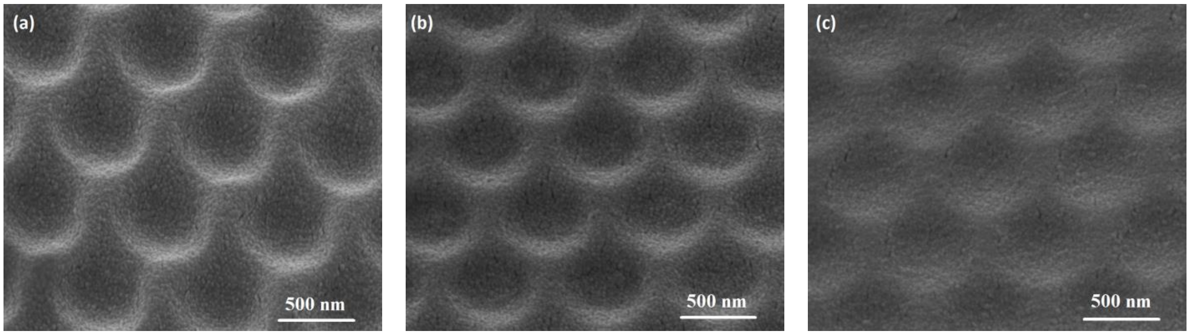

Figure 4.2. SEM micrographs of (a) 2%, (b) 5%, and (c) 10% w/v gold-coated polystyrene films after nanoimprinting with PDMS stamp at a 45° tilt. All the films show tapered nanocups with period ~750 nm. The scale bar is 500 nm.

4.4.2 Optical measurements

Specular transmission measurements on the gold-coated samples were performed using a Cary 5000 UV-Vis-NIR spectrophotometer, using an unpolarized source. The measured transmission characteristics of the gold-coated nanocup films (PS concentration 2%, 5%, 10%) are illustrated in Figure 4.3a-4.3c. The strongest peak at $\lambda_{sp} \sim 504$ nm, present in all cases, corresponds to the characteristic surface plasmon resonance (SPR) peak of gold, which is expected at the wavelength when $|\varepsilon_{Au}+2\varepsilon_{air}|=0$ [24]. The extraordinary transmission (EOT) peak remarkably appears at an expected $\lambda_1 \sim 704$ nm, nearly the period (a) of the structure. For nanocups on gold-coated 2% PSF (Figure 4.3a), the transmission approaches ~4%, which is more than 2 times larger than the classically expected value. The enhancement factor of 2 is typical for EOT measurements, and the classic measurements of Ebbesen et al. also observed an enhancement factor of 2-3 relative to the classically expected values. There is a weak transmision peak (T ~ 1.5%) at ~1000 nm which gradually diminishes as the concentration of PS solution increases. This peak appears at a wavelength $\lambda_2 \sim an_0$, where n_0 is the refractive index of the glass substrate ($n_0 \sim 1.5$). As expected, the EOT peak becomes weaker as the PS solution concentration increases from 2% to 10%, corresponding to decrease in depth of the nanocup.

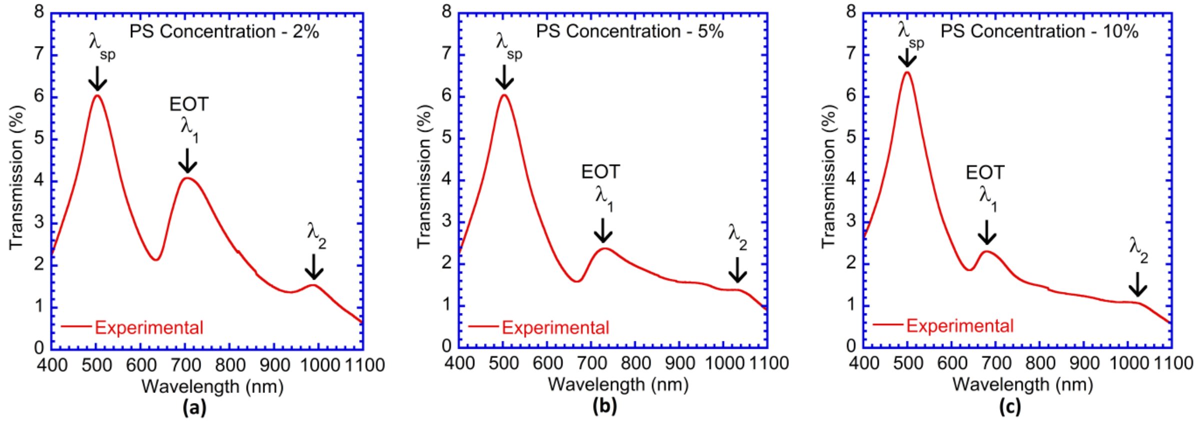

Figure 4.3. Measured transmission spectra of gold-coated polystyrene films with (a) 2%, (b) 5%, and (c) 10% concentration. The peak at $\lambda_{sp} \sim 504$ nm corresponds to SPR peak of gold. The peak at $\lambda_1 \sim 704$ nm is the EOT peak.

4.4.3 Surface plasmons

Our experimental EOT peak and the simulated results (described in next section) support the formation of surface plasmons (SPs) on the periodically corrugated nanocup lattice. To see this connection, we note that the triangular lattice (with period a) has the reciprocal lattice vectors $\boldsymbol{G}$:

$$G_1 = \frac{2\pi}{a}(1, -\frac{1}{\sqrt{3}}); G_2 = \frac{2\pi}{a}(0, \frac{2}{\sqrt{3}}) \tag{4.1}$$

Surface plasmons at metal-dielectric interface films are longitudinal modes propagating along the surface with exponentially decaying amplitude away from the interface, with the dispersion relation,

$$k_{sp} = \frac{\omega}{c}\left(\frac{\varepsilon_1\varepsilon_2}{\varepsilon_1+\varepsilon_2}\right)^{1/2} \tag{4.2}$$

k_{sp} is the wave-vector of surface plasmons and ω is the angular frequency. ε_2 is the real part of the metal dielectric function that is negative, and large in magnitude, for IR frequencies. ε_1 describes the dielectric media. Since the surface plasmon dispersion lies below the incoming light line for any angle of incidence (θ), incoming light cannot directly generate SPs on a smooth surface.

When an incident light of angular frequency ω, impinges on the patterned surface at an angle θ, it can couple to a surface plasmon at the air-metal interface through a reciprocal lattice vector,

$$\frac{\omega}{c}\sin\theta\,\mathbf{i} + \mathbf{G} = \mathbf{k}_{sp} \tag{4.3}$$

By combining the dispersion relation (4.2) with the momentum conservation condition (4.3), we get the well-known eigenvalue equation for the surface plasmon frequencies,

$$\left(\frac{\varepsilon_1\varepsilon_2}{\varepsilon_1+\varepsilon_2}\right) = \left(\sin\theta\cos\varphi \pm i\frac{\nu_0}{\nu}\right)^2 + \left(\sin\theta\sin\varphi \mp i\frac{1}{\sqrt{3}}\frac{\nu_0}{\nu} \pm j\frac{2}{\sqrt{3}}\frac{\nu_0}{\nu}\right)^2 \tag{4.4}$$

Here the dimensionless frequency unit is ν_0=c/a (400 THz for a=750 nm). The fundamental mode (i=1, j=0 or i=0, j=1), or Wood's anomaly, is predicted to occur at $\lambda_W = \sqrt{3}a/2$, i.e. at a wavelength slightly *smaller* than the lattice period a, for the triangular lattice symmetry. At this wavelength $\lambda_W = \sqrt{3}a/2 = 0.866a$ (650 nm for a=750 nm) the transmission T has a minimum, and is the position of the well-known Wood's anomaly, where the diffraction order changes from evanescent to propagating. The EOT peak occurs at a wavelength λ_1 slightly larger than this value near ~704 nm (Figure 4.3), which is still slightly smaller than the period *a*. The wavelength difference between the EOT peak and the Wood's anomaly depends on details of the metal layer thickness, hole radius, and geometry. λ_1 is close to *a* and can be slightly lower/higher than *a* depending on the geometry.

It is interesting to compare this analysis with the more frequently used square lattice, where the Wood's anomaly is predicted to occur at a wavelength of *a*, where T=0, and the EOT peak is at a wavelength slightly *larger* than *a*. This is precisely the result which we found in our previous scattering matrix simulations for the square lattice [26], where the minimum T occurs at $\lambda \sim a$ and the EOT peak at $\lambda > a$ (square lattice).

4.4.4 Optical simulations

We use the rigorous scattering matrix (SM) method [25] to simulate the electromagnetic properties of subwavelength nanocup arrays on a gold-coated polystyrene film and understand the underlying physics. The simulated structure is similar to that Figure 4.1a with tapered nanocup arrays arranged in triangular symmetry in the lattice. The simulation methodology for similar structure has been described in detail in our previous publications [26,27]. Briefly, Maxwell's equations are solved in Fourier space in three-dimensions. The structure is divided into slices along the *z*-axis and the dielectric function $\varepsilon(r)$ is expressed as a periodic function of the planar coordinates (*x*,*y*) in each slice. Hence the dielectric function and its inverse are expressed as a Fourier expansion with coefficients $\varepsilon(\mathbf{G})$ or $\varepsilon^{-1}(\mathbf{G})$, where **G** are the reciprocal lattice vectors of the two-dimensional lattice. The electric and magnetic fields are expanded in Bloch waves, N_G (*k* is a Bloch wave vector).

$$\mathbf{E}_{\mathbf{k}}(\mathbf{r}) = \sum_{\mathbf{G}} \mathbf{E}_{\mathbf{G}}(z) e^{i(\mathbf{k}+\mathbf{G}).\mathbf{x}_{\|}} \tag{4.5}$$

A transfer matrix in each layer is calculated that relates the *z* dependence of the **E**, **H** fields in each layer. The transfer matrix includes both polarizations of the wave, and is diagonalized to obtain the eigenmodes within the layer. Continuity of the parallel components of **E** and **H** at each interface leads to the individual scattering matrices of each layer, which are then convoluted into the scattering matrix S for the entire structure using a recursion algorithm. Using the total S matrix, we obtain the reflection and transmission of the structure when fields are incident from the top. For this case, we have tested the convergence of these results with 400-769 Bloch waves (N_G) per polarization corresponding to a scattering matrix size of 800-1538. The number of Bloch waves terminates on a closed shell of reciprocal lattice vectors **G**. The largest scattering matrix of size 1538 cannot be performed easily with routine compilation due to memory constraints and requires dynamic linking of runtime libraries [28]. The convergence was achieved with ~535-769 Bloch waves corresponding to scattering matrix size of 1070-1538 for both polarizations of the field in the triangular lattices [26]. We utilize the experimentally measured frequency dependent dielectric functions $\varepsilon(\lambda)=(\varepsilon_1,\varepsilon_2)$ of gold [29].

The physics underlying the SM matrix method is very similar to that employed in the rigorous coupled wave analysis (RCWA), where the fields are expanded also in Bloch waves. Early RCWA simulations [30,31] have concentrated on 1-d grating structures, where TE and TM modes are decoupled. Most implementations of RCWA utilize a transfer matrix to connect the fields in one layer with the next successive layer, utilizing continuity of the parallel components of **E** and **H**. The transmitted and reflected fields are obtained through transfer matrices on each layer. The SM utilizes the individual scattering matrices s_i for each layer which can have greater stability than the transfer matrices [32]. Rather than computing the fields at the individual layers in RCWA, the entire scattering matrix of the structure is computed in SM.

We plot the computed transmission spectra for gold-coated polystyrene films in Figures 4.4a and 4.4b, in conjunction with measurements. Similar to the experimental geometry for the film fabricated from 2% PS solution, the simulations have been done for array of nanocups arranged in a triangular lattice of period (*a*) 750 nm. The polarization is along the *x*-axis – the symmetry of the nanocups. Due to triangular lattice symmetry all polarizations rotated by 60° from the x-axis, and polarization vectors reflected through the six mirror planes are equivalent at normal incidence. The nanocups are tapered with largest R/*a* ~ 0.33 at the surface and the smallest R/*a* ~ 0.06 at the bottom rendering the nanocup aperture at the bottom highly subwavelength as their depth from the surface increases (Figure 4.1b). Simulations utilized different thickness (*t*) of an ultrathin gold layer between the substrate and the nanocup as shown in Figure 4.1b.

It can be seen that the computed transmission spectra for (Figures 4.4a, 4.4b) for two different thicknesses of the ultrathin gold layer ($t = 5$ nm, 10 nm) are in reasonable agreement with the measured values, especially for the positions and magnitudes of the transmission peaks. The simulated transmission shows a doublet peak at 707 nm and 720 nm centered at the same wavelength as the measured curve (Figure 4.4a). There are additional sharp side-bands on both sides of the simulated doublet peak. It is expected that these features will combine into the single broad peak observed in experiment at 704 nm. Furthermore, averaging over all the polarizations in the plane also results in the generation of a broader peak centered at 704 nm. The EOT peak occurs from the generation of surface plasmons at the top surface of the structure – the corrugated air-gold interface – as discussed previously. There is a second weaker SP at the gold-(PS/glass) interface at $\lambda_2 \sim n_0 a \sim 1.5a$ near ~1.0 µm. The interaction between the gold-air and gold-(PS/glass) SPs splits each of them into double modes similar to a SP molecule [9] with the splitting dependent on the spatial separation between the two interfaces. This is the cause of the double peak feature at 707-720 nm and also the weaker double peak at 950-1000 nm (visible more clearly as a reflectance dip in Figure 4.4c). The simulated transmission is smaller than experiment because the experimental structure has gold sidewalls that are gradually graded from the thin value (5-10 nm) to the bulk value, whereas the simulations assume a fixed thickness of gold on the sloping sidewalls, thereby overestimating the gold content and reducing the transmission. Another notable feature (Figures 4.4a, 4.4b) is the departure of the simulated specular transmission (T_{spec}) from the total transmission (T_{tot}) at the expected Wood's anomaly wavelength $\lambda_W = \sqrt{3}a/2 =$ 650 nm when the incoming wave-vector ($k=2\pi/\lambda$) matches the first reciprocal lattice vector ($G_1=2(2\pi)/\sqrt{3}a$). Below this wavelength diffraction takes place and decreases the specular transmission (described in previous section on *Surface Plasmons*). This is exactly the case for the simulations where $T=0$ at $\lambda_W=660$ nm (Figure 4.4a), and the measured T has a minimum at ~635 nm.

The various features of the transmission spectra (Figure 4.4a) are also represented in the reflectance (Figure 4.4c). The simulated and measured transmission peaks at 504 nm from the gold surface plasmons correspond to broad regions of low reflectance below 510 nm. At short wavelengths near 400 nm the structure is absorbing and has low T and R. The simulated EOT peak at ~707 nm corresponds to a sharp minima of the reflectance (R~0, Figure 4.4c). Similarly, the experimental EOT peak at 704 nm corresponds to the measured reflectance minimum at ~725 nm. The two weak double peaks in the simulated T at 950 nm and 1000 nm also appear as distinct shallow reflectance minima. The Wood's anomaly related minima in T at ~660 nm (simulation) and 635 nm (experiment) correspond to the maxima in simulated and experimental reflectance, at similar wavelengths. The simulated reflectance is overall somewhat higher than measurement possibly due to the random fine grain gold structure (<50 nm) seen in the SEM (Figure 4.2), that is superimposed on the larger scale periodicity, and may cause additional scattering in the experimental structure.

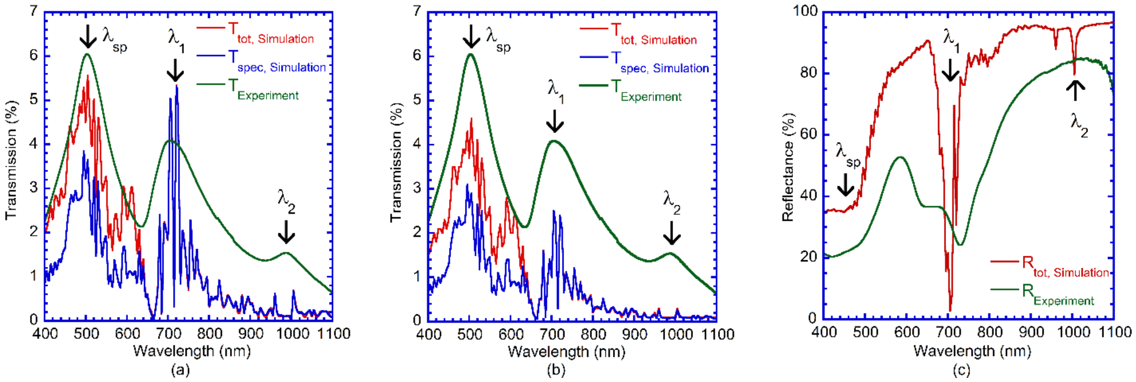

Figure 4.4. Simulated transmission through tapered nanocup array arranged in a triangular lattice of period 750 nm for two thicknesses (*t*) of the ultrathin gold layer (a) 5 nm, and (b) 10 nm at the bottom of the nanocup. The simulations are done for constant R/*a* = 0.33 at the nanocup opening. (c) Comparison of simulated (red) total reflection spectra with experimental (green) values for 2% concentration gold-coated PS film, for the 5 nm ultrathin gold film. The simulations utilize N_G=769.

The multi-layered experimental structure is more complex consisting of nanocup / Au (5 nm) / Ir (3 nm) / PS (15 nm) / Glass. The PS thickness below the nanocup is the thickness of the starting PS layer (265 nm for 2% solution - Table 4.1), from which the experimentally determined imprinted depth (l_1 ~ 250 nm) is removed, resulting in l_2 ~ 15 nm of PS between the nanocup and glass substrate (see Figure 4.1b). We have simulated the effect of this multilayer structure that adds a 3 nm Ir layer and the PS layer of index n_{PS} = 1.57 between the Ir and the glass. The resulting transmission shown in Figure 4.5 (lower panel) is not significantly affected from the result in Figure 4.4a (also Figure 4.5, upper panel), showing both the gold SP peak and the EOT peak at the similar positions without the Ir or PS layer.

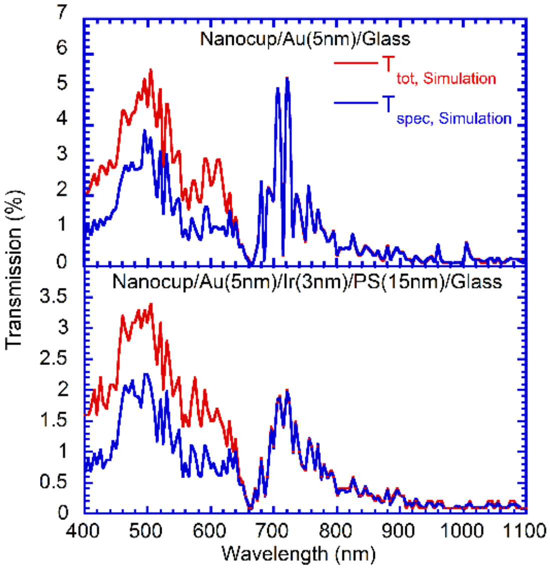

Figure 4.5. Simulated transmission through tapered nanocup array consisting of nanocup / Au(5 nm) / Ir(3 nm) / PS(15 nm) / Glass arranged in a triangular lattice of period 750 nm. The simulated transmission for nanocup / Au(5 nm) / Glass (same as Figure 4.4a) is presented in the upper panel for comparison. The simulations utilize N_G=769.

4.4.5 Electric field intensity profile

To obtain insight into the extraordinary transmission mechanisms we calculate the electric field intensity $|\mathbf{E}|^2$ at the resonant λ_1 = 700 nm in the *xz*-plane perpendicular to the structure and passing through the symmetry axis of the nanocup array (Figure 4.6a). Within the air region of the nanocups very large field enhancements exceeding 100 are found, with the highest enhancements occurring in a layer ~40 nm above the bottom of the nanocup, where modal maxima occur. Since the opening radius of the nanocup (R/*a* ~ 0.33) exceeds the waveguide cutoff for propagating modes (R/*a* ~ 0.29) in a cylindrical waveguide [33], the lowest order modes (such as TE_{11}, TM_{01}) can begin propagating in the upper region of the nanocup. As the nanocup tapers the mode gets squeezed near the bottom of the nanocup producing regions of high field intensity. Focusing of fields to high intensities near the bottom of a nanocone hole array in Si have also been observed in simulations [34].

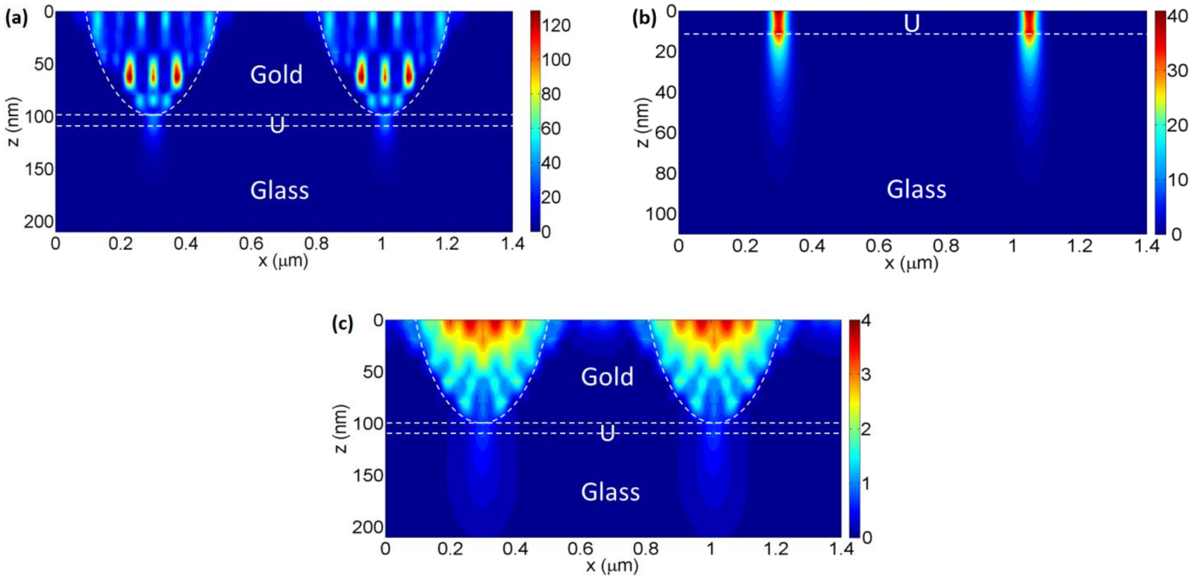

Figure 4.6. (a) Electric field intensity at λ_1 = 700 nm showing the enhanced field in the *xz*-plane. (b) Enlarged view of the electric field intensity plot showing the fields in glass and ultrathin gold layer (U). (c) Electric field intensity at λ_{sp} = 504 nm showing the enhanced field in the *xz*-plane.

A magnified view of the ultrathin gold layer and substrate (Figure 4.6b) shows very large electric field intensities within the 10 nm ultrathin gold layer, with intensities enhanced by a factor of 30-40 *inside* the gold layer. The field transmits through the ultrathin gold layer in a very narrow cylindrical profile of width ~50 nm, into the substrate, with the axis of the cylinder along the depth axis (*z*-axis). The cylindrical mode profile is deeply sub-wavelength with a spatial scale <λ/10. This is possible since the thickness of the ultrathin gold layer, is smaller than the skin depth of gold at optical wavelengths ($\frac{\lambda}{2\pi\,\mathrm{Im}(n)}$ ~ 25-30 nm). The $|\mathbf{E}|^2$ is enhanced by 30-40 at the gold-glass interface and by >10 at a depth of ~20 nm in the glass. Such enhancements in the field intensity can lead to strong non-linear phenomena such as second harmonic generation (SHG) [35,36], which is proportional to the localized $|\mathbf{E}|^2$. Qualitatively, the transmission arises from a focusing of a waveguide mode into the ultrathin gold layer. The transmission peak at 504 nm is due to the surface plasmon mode of gold where $|\mathbf{E}|^2$ is enhanced by 3-4 within the nanocup (Figure 4.6c) and the intensity is large at the entire gold-air surface. The SPP mode generates transmission through the ultrathin gold layer into the glass.

4.5 Discussion

Previous observations of EOT have been performed on well-defined holes or cavities in metal films. We demonstrate that a *continuous* gold film deposited on a periodically corrugated substrate demonstrates the EOT, without the need to do any etching of the film. This result is counter-intuitive, and may be understood by recognizing that the thickness of our metal film is highly non-uniform. The sputter-deposition of gold at a 45° angle to the substrate likely generates thicker sidewalls within the nanocup arrays, and very thin gold coatings at the bottom of the conical pits (Figure 4.1b), which may be comparable or less than the skin depth of gold (~25-30 nm at optical wavelengths). The thin non-uniform layer of gold at the bottom of the conical pits, may allow sufficient light transmission, whereas the thicker gold film away from the bottom of the conical pits will not allow light transmission. Our method does not require self-assembly of spheres [19]. Self-assembly results in domain formation and random point defects – both features causing larger inhomogeneities than in nanoimprinting method that we utilize here. Furthermore the transmission occurs through the ultrathin metal layer in our nanocup array in contrast to waveguided modes through the spheres in the self-assembled structure [19]. For a triangular lattice, the fraction of area occupied by nanocups in the film is given by $f = \pi R^2 \big/ \left(\sqrt{3} a^2 / 2 \right)$. For smallest R/$a$ ~ 0.06, f ~ 1.5%. We see that the transmission (T ~ 4%) is enhanced significantly by more than a factor of 2.5 compared to the fraction of the area occupied by nanocups in the film. The enhancement factor of 2.5 is typical of *larger* radius (R/*a*) arrays. It is well known that when the radius of the apertures decreases the enhancement factor increases considerably. For example at R/*a*=0.2 we found an enhancement factor of 8 in our previous work on hole arrays [26].

A continuous film also allows the possibility of modulating optical transmission in the presence of a current flow in the continuous gold film i.e. under current bias, where currents flow in the thin Au film region through which light transmits. Although currents can flow in discontinuous hole array films, there is no current flow within the holes, limiting electro-optical effects.

Thus our novel corrugated structure has the functionality of a subwavelength hole array *without* actually having holes or etched features, and can be replicated over large areas with continuous gold films. As noted earlier, the complex step of etching the film is no longer required, and advanced nanofabrication facilities are not necessary

4.5.1 Ultrathin films

We note that recently there has been great interest in continuous ultrathin coatings, with thickness far smaller than the optical thickness. Highly absorbing dielectric coatings (of Ge) as small as 5-25 nm thickness exhibited novel interference effects which selectively absorb and transmit various wavelengths of visible spectrum [37]. Ultrathin silver coatings have been shown to have a reflection phase shift continuously tunable from a perfect electric mirror ($\varphi=\pi$) to a perfect magnetic mirror ($\varphi=0$) depending on the thickness of the coating [38]. This changes the standing wave profile in planar devices allowing highly enhanced absorption in sub-100 nm thick solar cell layers [38] – a feature not possible with conventional optically thick metal coatings. Our ultrathin gold film is an example of novel optical effects arising from ultrathin films, and illustrates surprising consequences of such optically thin films, that are of much topical interest.

4.5.2 Biosensing applications

We envisage our nanocup structure may have robust application to biosensing, where a thin protein layer can be coated on the surface of the nanocup lattice. Experiments by Cetin [39] et al. with a bare gold nanohole square array (of period 600 nm and hole diameter 200 nm) demonstrated the typical EOT peak at 683 nm. After binding a protein bilayer of 3 nm thickness the EOT mode shifted to 702 nm, due to the minute changes in the refractive index in the vicinity of the nanohole. The wavelength shift was proportional to the protein (IgG) concentration, resulting a lens-free imaging platform with a detection limit of μg ml^{-1}. In these experiments *small* 100 μm x 100 μm pixels were utilized, fabricated with e-beam lithography.

We envisage our nanocup structure would serve as a robust platform for biosensing, utilizing far *larger* pixels upto and exceeding 1cm x 1cm in size. A protein bilayer few nm thick can bind on the nanocup surface, and result in a detectable shift of the EOT transmission peak at ~700 nm. Furthermore our large area nanocup structure could be fabricated with much faster throughput and lower cost than with the traditional e-beam lithographic methods.

We illustrate this biosensing concept with the simulation of a thin biosensing film of thickness d, and a typical dielectric (protein) refractive index $n_{\text{diel}} \sim 1.4$ on the surface on the nanocup. Our simulations (Figure 4.7 with $N_G = 535$) show a red-shift $\Delta\lambda$ of the EOT peak by 30 nm with a 5 nm coating, typical of a protein bilayer. An additional gold-dielectric surface plasmon transmission peak appears at ~ $n\lambda_1$ ~ 800-830 nm corresponding to the average n (~1.2) of air and dielectric (protein) layer.

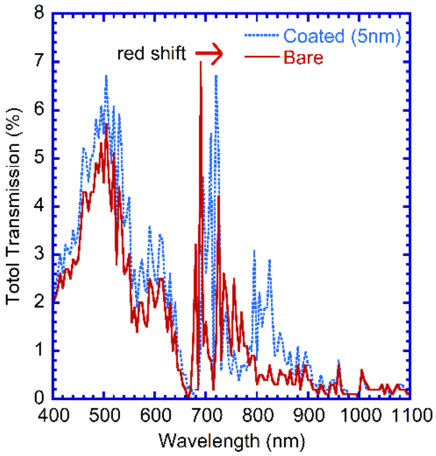

Figure 4.7. Simulated transmission for nanocup structure with and without a 5 nm adsorbed layer, illustrating the red-shift of the EOT peak by 30 nm. The simulations utilize N_G=535.

We note that the EOT based biosensing approach is in contrast to the local SP resonance (LSPR) methods extensively developed [40,41,42] utilizing functionalized gold nanoparticles that exhibit the LSPR peak dependent on the size and shape of the nanoparticle. When the analytes bind to the functional group, characteristic wavelength shifts ($\Delta\lambda$), as large as 20-67 nm, are readily observed [40]. A future direction may be to combine the nanoparticles with nanohole/nanocup arrays to detect biomolecules at even lower concentration.

Very recent studies have shown that such nanohole/nanocup arrays exhibiting EOT can be used for other novel biological and imaging applications. Silver nanohole arrays coated with various biological species were imaged with surface-enhanced Raman spectroscopy (SERS) and focused hotspots were positioned using holographic laser illumination [43], to produce a blinking behavior of the hotspots. Nanohole arrays in free standing metal-coated nitride films were used for trapping and analyzing single organelles such as mitochondria [44]. Similarly, binary nanohole structures having two different hole sizes and linear nanoguides were used for exciting fluorescence from bacterial species and observing bacterial dynamics with subwavelength precision [45].

4.6 Conclusion

In summary, we experimentally and theoretically demonstrated the extraordinary transmission on a *continuous* gold film deposited on periodically corrugated substrates, even though no holes were etched in the film. The varying thickness of the gold film on the corrugated substrate enables spatial regions of high transmission through ultrathin regions of the films (~5 nm) that are thinner than the skin depth, in conjunction with negligible transmission through thick regions of the metal film. This phenomenon has functionality similar to a nanohole array. Simulated fields show very high enhanced intensity (~40) in the ultrathin gold layer, and >100 within the nanocup. The extraordinary transmission peak is red-shifted by 30 nm when the nanocups are coated with a few nm thin analyte film, which can find applications in biosensing. Our procedure provides a simple, rapid, low-cost process to fabricate *large area* arrays where complex nanofabrication is not needed, but show the extraordinary transmission phenomena, observable in any spectrophotometer. Our corrugated continuous metal-coated structures have much promise for photonics applications, without the need for microscopy in performing experiments.

4.7 Acknowledgements

We thank Dr. J. Kim and R. Dhakal for assistance with soft lithography, and P. H. Joshi for transmission measurements. This research was partially supported by the National Science Foundation through Grant CMMI-1265844 (fabrication); and the Ames Laboratory, which is operated for the U.S. Department of Energy (USDOE) by Iowa State University under contract No. DE-AC02-07CH11385 (optical measurements and theoretical analysis). We acknowledge use of computational resources at the National Energy Research Scientific Computing Center (NERSC) which is supported by the Office of Science of the USDOE under Contract No. DE-AC02-05CH11231.

4.8 References

1. T. W. Ebbesen, H. J. Lezec, H. F. Ghaemi, T. Thio and P. A. Wolff, "Extraordinary optical transmission through sub-wavelength hole arrays," *Nature* **391**, 667–669 (1998).
2. C. Genet and T. W. Ebbesen, "Light in tiny holes," *Nature* **445**, 39–46 (2007).
3. W. L. Barnes, A. Dereux and T. W. Ebbesen, "Surface plasmon subwavelength optics," *Nature* **424**, 824–830 (2003).
4. H. F. Ghaemi, T. Thio, D. Grupp, T. W. Ebbesen and H. J. Lezec, "Surface plasmons enhance optical transmission through subwavelength holes," *Phys. Rev. B* **58**, 6779–6782 (1998).
5. W. L. Barnes, W. A. Murray, J. Dintinger, E. Devaux and T. W. Ebbesen, "Surface Plasmon Polaritons and Their Role in the Enhanced Transmission of Light through Periodic Arrays of Subwavelength Holes in a Metal Film," *Phys. Rev. Lett.* **92**, 107401 (2004).
6. T. Rindzevicius, Y. Alaverdyan, A. Dahlin, F. Höök, D. S. Sutherland and M. Käll, "Plasmonic sensing characteristics of single nanometric holes," *Nano Lett.* **5**, 2335–2339 (2005).

7. Y. Liu, J. Bishop, L. Williams, S. Blair and J. Herron, “Biosensing based upon molecular confinement in metallic nanocavity arrays,” *Nanotechnology* **15**, 1368–1374 (2004).

8. H. A. Bethe, “Theory of Diffraction by Small Holes,” *Phys. Rev.* **66**, 163–182 (1944).

9. L. Martín-Moreno, F. J. García-Vidal, H. J. Lezec, K. M. Pellerin, T. Thio, J. B. Pendry and T. W. Ebbesen, “Theory of Extraordinary Optical Transmission through Subwavelength Hole Arrays,” *Phys. Rev. Lett.* **86**, 1114–1117 (2001).

10. K. L. Van Der Molen, K. J. Klein Koerkamp, S. Enoch, F. B. Segerink, N. F. Van Hulst and L. Kuipers, “Role of shape and localized resonances in extraordinary transmission through periodic arrays of subwavelength holes: Experiment and theory,” *Phys. Rev. B* **72**, 045421 (2005).

11. Y.-H. Ye and J.-Y. Zhang, “Middle-infrared transmission enhancement through periodically perforated metal films,” *Appl. Phys. Lett.* **84**, 2977–2979 (2004).

12. K. J. K. Koerkamp, S. Enoch, F. B. Segerink, N. F. Van Hulst and L. Kuipers, “Strong influence of hole shape on extraordinary transmission through periodic arrays of subwavelength holes,” *Phys. Rev. Lett.* **92**, 183901 (2004).

13. T. Thio, H. F. Ghaemi, H. J. Lezec, P. A. Wolff and T. W. Ebbesen, “Surface-plasmon-enhanced transmission through hole arrays in Cr films,” *J. Opt. Soc. Am. B* **16**, 1743-1748 (1999).

14. K. Kumar, H. Duan, R. S. Hegde, S. C. Koh, J. N. Wei and J. K. Yang, “Printing colour at the optical diffraction limit,” *Nature Nanotech.* **7**, 557–561 (2012).

15. V. Canpean and S. Astilean, “Multifunctional plasmonic sensors on low-cost subwavelength metallic nanoholes arrays,” *Lab Chip* **9**, 3574-3579 (2009).

16. R. H. Fan, L. H. Zhu, R. W. Peng, X. R. Huang, D. X. Qi, X. P. Ren, Q. Hu and M. Wang, “Broadband antireflection and light-trapping enhancement of plasmonic solar cells,” *Phys. Rev. B* **87**, 195444 (2013).

17. Y. Liu, R. Dhakal, V. Dalal and J. Kim, “Polarization-diverse light absorption enhancement in organic photovoltaic structures with one-dimensional, long-pitch metallic gratings: Design and experiment,” *Appl. Phys. Lett.* **101**, 233904 (2012).

18. B. Curtin, R. Biswas and V. Dalal, “Photonic crystal based back reflectors for light management and enhanced absorption in amorphous silicon solar cells,” *Appl. Phys. Lett.* **95**, 93–96 (2009).

19. L. Landström, D. Brodoceanu, D. Bäuerle, F. J. Garcia-Vidal, S. G. Rodrigo and L. Martin-Moreno, “Extraordinary transmission through metal-coated monolayers of microspheres,” *Opt. Express* **17**, 761–772 (2009).

20. Benchmark Technologies, http://www.benchmarktech.com/imprintstamps.

21. D. Qin, Y. Xia and G. M. Whitesides, “Soft lithography for micro- and nanoscale patterning,” *Nat. Protoc.* **5**, 491–502 (2010).

22. V. E. Ferry, M. A. Verschuuren, H. B. T. Li, R. E. I. Schropp, H. A. Atwater and A. Polman, “Improved red-response in thin film a-Si:H solar cells with soft-imprinted plasmonic back reflectors,” *Appl. Phys. Lett.* **95**, 183503 (2009).

23. D. B. Hall, P. Underhill and J. M. Torkelson, “Spin coating of thin and ultrathin polymer films,” *Polym. Eng. Sci.* **38**, 2039–2045 (1998).

24. J. D. Jackson, *Classical Electrodynamics*, Wiley, New York, 1998.

25. Z.-Y. Li and L.-L. Lin, “Photonic band structures solved by a plane-wave-based transfer-matrix method,” *Phys. Rev. E* **67**, 046607 (2003).

26. R. Biswas, S. Neginhal, C. G. Ding, I. Puscasu and E. Johnson, “Mechanisms underlying extraordinary transmission enhancement in subwavelength hole arrays,” *J. Opt. Soc. Am. B* **24**, 2589–2596 (2007).

27. R. Biswas, C. G. Ding, I. Puscasu, M. Pralle, M. McNeal, J. Daly, A. Greenwald and E. Johnson, “Theory of subwavelength hole arrays coupled with photonic crystals for extraordinary thermal emission,” *Phys. Rev. B* **74**, 045107 (2006).

28. Documentation on compilation options at www.nersc.gov.

29. E. D. Palik, *Handbook of Optical Constants of Solids*, Academic Press, San Diego, 1998.

30. M. G. Moharam and T. K. Gaylord, “Diffraction analysis of dielectric surface-relief gratings,” *J. Opt. Soc. Am.* **72**, 1385-1392 (1982).

31. M. G. Moharam and T. K. Gaylord, “Rigorous coupled-wave analysis of metallic surface-relief gratings,” *J. Opt. Soc. Am. A* **3**, 1780-1787 (1986).

32. V. Liu and S. Fan, “S^4: A free electromagnetic solver for layered periodic structures,” *Comput. Phys. Commun.* **183**, 2233–2244 (2012).

33. J. D. Kraus, *Electromagnetics*, McGraw-Hill, New York, 1992.

34. X. Zhang, Y. Yu, J. Xi, Y. Wang and X.-H. Sun, “Absorption enhancement in double-sided nanocone hole arrays for solar cells,” *J. Opt.* **17**, 75901 (2015).

35. M. Airola, Y. Liu and S. Blair, “Second-harmonic generation from an array of sub-wavelength metal apertures,” *J. Opt. A* **7**, S118–S123 (2005).

36. J. A. H. Van Nieuwstadt, M. Sandtke, R. H. Harmsen, F. B. Segerink, J. C. Prangsma, S. Enoch and L. Kuipers, “Strong Modification of the Nonlinear Optical Response of Metallic Subwavelength Hole Arrays,” *Phys. Rev. Lett.* **97**, 146102 (2006).

37. M. A. Kats, R. Blanchard, P. Genevet, and F. Capasso, “Nanometre optical coatings based on strong interference effects in highly absorbing media,” *Nature Mater.* **12**, 20-24 (2013).

38. M. Esfandyarpour, E. C. Garnett, Y. Cui, M. D. McGehee and M. L. Brongersma, “Metamaterial mirrors in optoelectronic devices,” *Nature Nanotech.* **9**, 542-547 (2014).

39. A. E. Cetin, A. F. Coskun, B. C. Galarreta, M. Huang, D. Herman, A. Ozcan and H. Altug, “Handheld high-throughput plasmonic biosensor using computational on-chip imaging,” *Light Sci. Appl.* **3**, e122 (2014).

40. J. N. Anker, W. P. Hall, O. Lyandres, N. C. Shah, J. Zhao and R. P. Van Duyne, “Biosensing with plasmonic nanosensors,” *Nature Mater.* **7**, 442-453 (2008).

41. A. G. Brolo, “Plasmonics for future biosensors,” *Nature Photon.* **6**, 709-713 (2012).

42. Y. Lu, G. L. Liu, J. Kim, Y. X. Mejia and L. P. Lee, “Nanophotonic Crescent Moon Structures with Sharp Edge for Ultrasensitive Biomolecular Detection by Local Electromagnetic Field Enhancement Effect,” *Nano Lett.* **5**, 119-124 (2005).

43. C. T. Ertsgaard, R. M. McKoskey, I. S. Rich and N. C. Lindquist, “Dynamic Placement of Plasmonic Hotspots for Super-resolution Surface-Enhanced Raman Scattering,” *ACS Nano* **8**, 10941-10946 (2014).

44. S. Kumar, G. G. Wolken, N. J. Wittenberg, E. A. Arriaga and S.-H. Oh, “Nanohole Array-Directed Trapping of Mammalian Mitochondria Enabling Single Organelle Analysis,” *Anal. Chem.* **87**, 11973-11977 (2015).

45. W. Lee, Y. Kinosita, Y. Oh, N. Mikami, H. Yang, M. Miyata, T. Nishizaka and D. Kim, “Three-Dimensional Superlocalization Imaging of Gliding *Mycoplasma mobile* by Extraordinary Light Transmission through Arrayed Nanoholes,” *ACS Nano* **9**, 10896-10908 (2015).

CHAPTER 5

PHOTOLUMINESCENCE ENHANCEMENT OF $CuInS_2$ QUANTUM DOTS IN SOLUTION COUPLED TO PLASMONIC GOLD NANOCUP ARRAY[§]

Akshit Peer[1,2], Zhongjian Hu[3], Ajay Singh[3],
Jennifer A. Hollingsworth[3], Rana Biswas[1,2,4], and Han Htoon[3]

1. Ames Laboratory, Ames, IA 50011, USA
2. Department of Electrical and Computer Engineering, Iowa State University, Ames, IA 50011, USA
3. Center for Integrated Nanotechnologies, Materials Physics and Applications Division, Los Alamos National Laboratory, Los Alamos, NM 87545, USA
4. Department of Physics and Astronomy, Iowa State University, Ames, IA 50011, USA

Adapted from an article published in *Small* **13**, 1700660 (2017)

5.1 Abstract

A strong plasmonic enhancement of photoluminescence (PL) decay rate in quantum dots (QDs) coupled to an array of gold-coated nanocups is demonstrated. $CuInS_2$ QDs that emit at a wavelength that overlaps with the extraordinary optical transmission (EOT) of the gold nanocup array are placed in the cups as solutions. Time-resolved PL reveals that the decay rate of the QDs in the plasmonically coupled system can be enhanced by more than an order of magnitude. Using finite-difference time-domain (FDTD) simulations, it is shown

---

[§] A part of this work was carried out at Center for Integrated Nanotechnologies, Los Alamos National Laboratory, New Mexico under user proposals 2016AU0125 and 2016ARA0013. The quantum dots were fabricated by Dr. Ajay Singh.

that this enhancement in PL decay rate results from an enhancement factor of ~100 in field intensity provided by the plasmonic mode of the nanocup array, which is also responsible for the EOT. The simulated Purcell factor approaches 86 at the bottom of the nanocup and is ~3-15 averaged over the nanocup cavity height, agreeing with the experimental enhancement result. This demonstration of solution-based coupling between QDs and gold nanocups opens new possibilities for applications that would benefit from a solution environment such as biosensing.

5.2 Introduction

Plasmonic nanostructures, with their ability to concentrate intense electromagnetic energy within a small volume, not only modify light-matter interactions but also offer unprecedented opportunities to engineer the spontaneous emission processes of emitters that are coupled to them [1-4]. Semiconductor quantum dots (QDs) are versatile, solution-processible, photostable fluorophores capable of room-temperature single-photon emission with readily tunable optical properties. For these reasons, QDs have been included as the emitter in hybrid photonic-plasmonic systems comprising QDs and plasmonic nanostructures. Such coupled systems have been used for fundamental and applied investigations in nano-optics, nano-spectroscopy, and single-photon phenomena. Coupling between plasmonic optical antenna and QDs has been used to demonstrate enhanced and directional emission, which are crucial for numerous potential applications ranging from quantum optics to biological sensing [5-11].

“Non-toxic” QDs (typically defined as heavy metal-free compositions) are being investigated as biocompatible nanocrystal fluorophores. $CuInS_2$ QDs possess PL wavelengths in the red to near-infrared and, therefore, represent a promising system for biosensing, bioimaging, photovoltaics, and solid-state lighting [12-14]. Recent reports have shown that high PL quantum yields (QYs) are possible for $CuInS_2$ QDs with the addition of a thick ZnS shell [15-17]; however, in these cases the PL is shifted to the blue from the starting CIS QD emission to ~600-650 nm. QYs for CIS QDs emitting above 700 nm are still typically relatively low (*even with thin ZnS shell*) [17], for which the origin is still under debate [18,19]. Possible mechanisms for low QYs involve nonradiative electron trap states, recombination of electrons with dark hole states, or defect-induced donor-acceptor pair non-radiative recombination [12-14]. Coupling $CuInS_2$ QDs with a resonant plasmonic nanostructure offers an alternative route for enhancing PL performance. However, only a few such studies have been performed to date [20,21]. Furthermore, there is a lack of research for plasmonic-QD coupled systems in solution. QDs in the solution phase that are coupled to plasmonic nanostructures are potentially relevant for applications requiring a solution environment such as biosensing. For example, the enhanced photoluminescence in hot spot regions could be specifically utilized to improve the sensitivity and the limit of detection of photoluminescence-based analysis [22-24].

It has been shown previously that an array of subwavelength holes in a metal film (free-standing or on a substrate) generates extraordinary optical transmission (EOT) at a wavelength λ_{res} close to the period of the structure [25-29]. In addition, light tunneling through continuous metal films with periodic nanostructures such as nanocups, nanocones or dielectric ridges has recently attracted intense research interest [30-33]. In general, when these nanostructure arrays in the metal film reside on a substrate of refractive index n, there is an additional transmission peak at the wavelength $\lambda_{sub} \sim n \cdot \lambda_{res}$. At both peaks the transmission is dramatically enhanced over the expected classical value for the area of the nanostructure [34]. Such nanostructure arrays have been utilized extensively in chemical and biological sensing [35-37]. For instance, we have demonstrated a biosensing application of nanocup array structure based on the shift in the EOT peak by introducing a few nanometer thick dielectric coating with different refractive index (e.g. a typical protein layer with a refractive index of ~1.35-1.40) [33]. In the present study, we use a simple soft-lithographic technique to fabricate a large-area (>1 cm^2) nanocup array that does not require extensive photolithography and etching of the metal films. We investigate the plasmonic-exciton coupling between the gold nanocups and $CuInS_2$ QDs in solution. We demonstrate plasmonically enhanced PL decay of the $CuInS_2$ QDs coupled to the gold nanocup arrays, which is maximized at an EOT resonance wavelength that approximately matches the QD emission wavelength. Utilizing spectrally time-resolved spectroscopy, we observe that the PL decay rate is enhanced by more than one order-of-magnitude for the QDs coupled to plasmonic nanocups. The experimental observations are supported by numerical simulation results that show high electric field intensity in the nanocups, and a Purcell factor up to two orders-of-magnitude at the bottom of the nanocup and ~3-15 averaged over the nanocup height for a dipole coupled to the nanocup cavity.

5.3 Results and Discussion

5.3.1 Fabrication and characterization

The gold nanocup arrays were fabricated using a previously described method [33] (*Experimental Section*). Briefly, starting with a polycarbonate master pattern consisting of a periodic array of tapered nanocups having a period of ~750 nm, an inverse of the master was transferred onto a polydimethylsiloxane (PDMS) mold. The patterned PDMS mold was used to imprint on a polystyrene (PS) film spin-coated over a glass substrate thereby transferring the nanocup pattern to the PS film, in a double replication process. This was followed by an angle-directed sputter deposition of a thin gold film (~70 nm) on the PS nanocup substrate. The sample was placed at an angle of 45 degrees to the vertical and rotated so as to have non-uniform coating of gold over the nanocup sidewalls. This coating method ensures that the deposited gold is thicker at the top sidewalls and thinner towards the bottom of the nanocup. There is an ultrathin (~5 nm) layer of gold at the bottom of each nanocup, through which transmission of light may occur.

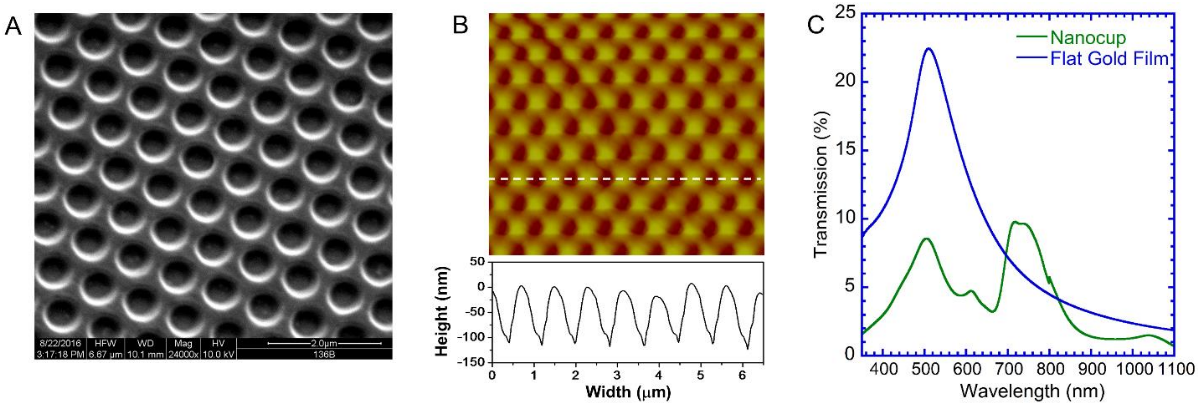

Figure 5.1. SEM micrograph (A) and AFM imaging (B) of the nanocups. The inset of (B) displays a linescan for the above image demonstrating the depth of nanocups. (C) Measured transmission spectra of gold nanocup arrays and a reference flat thin gold film with thickness of ~35 nm that has similar transmittance as the nanocup arrays near 700 nm.

Figure 5.1A and 5.1B show the images of the gold nanocup structure characterized by scanning electron microscopy (SEM) and atomic force microscopy (AFM), respectively. As shown in Figure 5.1A, a periodic array of gold nanocups with period ~750 nm and cup diameters ~500 nm were replicated with high fidelity. The AFM line-scan in Figure 5.1B reveals the depth of nanocups to be 120 nm. The optical transmission spectrum (Figure 5.1C) of the nanocup array shows a peak at ~504 nm, corresponding to the characteristic surface plasmon resonance (SPR) peak of gold. This SPR transmission peak is at the same wavelength as that in a thin gold (~35 nm thick) film on glass. The broader EOT peak appears at ~707 nm and ~720 nm. The EOT peak originates from the generation of surface plasmons at the top surface of the structure – the corrugated air-gold interface – as discussed previously [33]. The doublet peak is a result of the interaction between the gold-air and gold-glass SPs, which splits the single peak into a doublet mode similar to a SP molecule with the splitting dependent on the spatial separation between the two interfaces [38].

$CuInS_2/ZnS$ core/shell nanocrystals (hereafter denoted by CIS) were synthesized using a previously published procedure with slight modifications (*Experimental Section*) [17]. Figure 5.2A shows an angular dark field scanning transmission electron microscope (ADF-STEM) image of the CIS QDs with an average diameter of ~4 nm. As typical for this system, the absorption spectrum extending up to ~800 nm is relatively featureless (Figure 5.2B), while the PL peaks at 720 nm with a full width at half-maximum of 0.36 eV (150 nm), also consistent with previous reports [17, 39]. The broad emission around 720 nm (1.72 eV) of these CIS QDs overlaps the EOT peak of the gold nanocup arrays (Figure 5.2C), hence offering a prerequisite for effective plasmon-exciton coupling and PL enhancement of CIS QDs in the hybrid system.

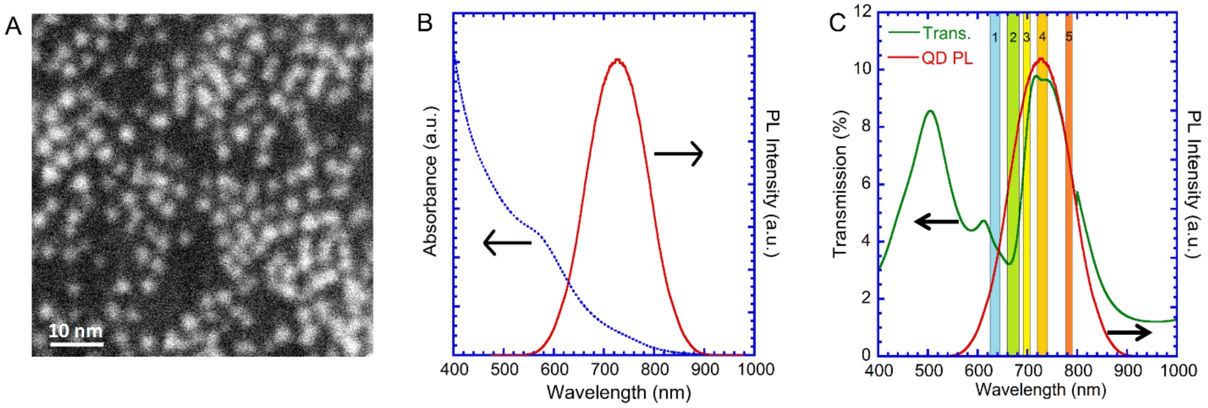

Figure 5.2. (A) ADF-STEM image of the CIS QDs. (B) Absorption and emission spectra of CIS QDs in toluene. (C) CIS QD PL (red) overlayed with the EOT (green) of the gold nanocup array. The different wavelength bands highlighted with colors are 1: 625-645 nm, 2: 660-683 nm, 3: 692-705 nm, 4: 720-740 nm, 5: 777-790 nm.

The hybrid system of the gold nanocups with CIS QDs in solution was prepared by depositing 100 μl QD solution on the nanocup array. A coverslip "lid" was added to minimize evaporation of the QDs solvent – a mixture of hexane and dichlorobenzene in a 1:9 volume ratio. Two control samples were prepared, one comprising CIS QDs on a clean glass coverslip and another with CIS QDs on a flat gold film-coated coverslip, which possessed similar transmission characteristics as the nanocup array sample at 700 nm. Again, both samples were covered with a top coverslip.

5.3.2 Optical spectroscopy

The PL characteristics of the samples were examined using a wide-field optical microscope, in which a 403 nm pulsed laser was used for excitation and the PL intensity and decays were collected from the other side of the samples by a single photon avalanche diode connected with a Hydraharp 400 TCSPC system (*Experimental Section*). Spectrally resolved PL decays were collected by placing tunable bandpass filters in front of the SPADs or a combination of short- and long-pass filters.

Figure 5.3A displays the decay curves of the overall broad PL band for the CIS QD solutions on a glass coverslip, on a gold film, and in the nanocup array, respectively. For QD solutions on the glass, the PL decays can be well fitted by four exponentials (see Table 5.2 in Supporting Information, SI). Compared to the typical lifetime of tens of ns for CdSe QDs, the PL lifetime of CIS QDs are much longer with an amplitude-weighted averaged lifetime around 200 ns. Such a long lifetime and multi-exponential decay behavior have been reported in previous research [12-14, 40-44]. The excited-state dynamics for this type of QDs is still under debate and not clearly understood yet, mainly due to uncertainties in the ternary CIS QD composition, size and shape, and external/internal defects. Some initial studies have attributed the short lifetime components to surface or interface defect states and the longer components to intrinsic defect states possibly involving donor-acceptor recombination transitions [40-42]. Recent studies have suggested that the short lifetime components are related to the band edge surface trapping and/or defect-induced charge recombination, while the longer one was attributed to sub-bandgap transition between band edge electrons and Cu vacancy localized holes [12-14, 43, 44].

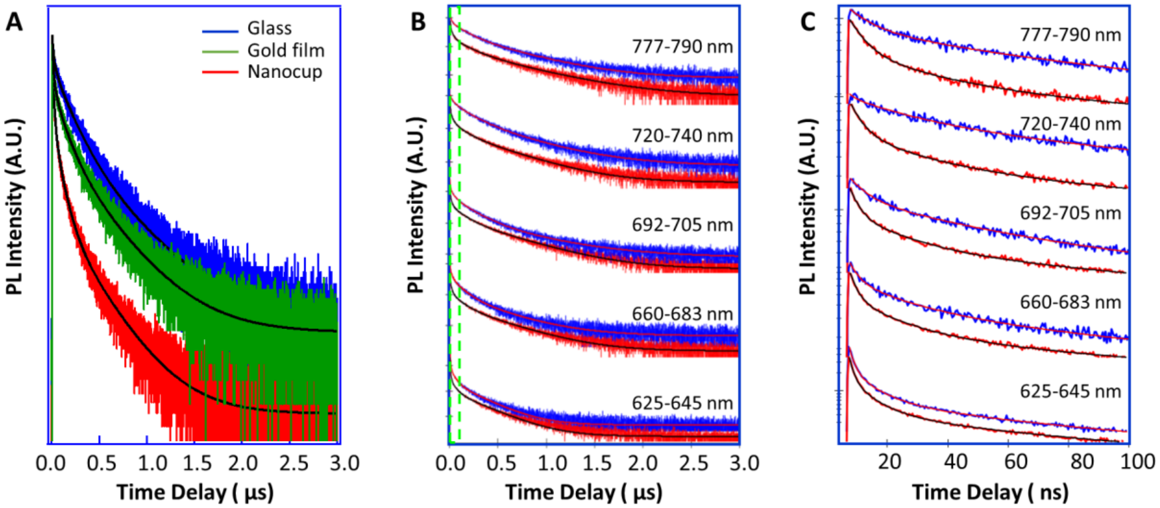

Figure 5.3. (A) Normalized broadband PL decay curves of CIS QDs on a glass coverslip, on a gold film, and in gold nanocup arrays. (B) Spectrally resolved PL decay curves of CIS QDs in gold nanocup arrays (red) and on glass coverslip (blue). Panel (C) displays the decays in the first 100 ns (green box) for corresponding curves in (B). Corresponding PL emission bands are shown as insets and multiexponential fits (black) overlay the decay curves. The decays in (B) and (C) have been slightly displaced vertically for clarity.

For the flat gold film sample, the PL intensity of CIS QD solution detected through the gold film is found be ~5.25% of that detected in case of QD solution on glass coverslip, 25% less than that would have allowed by an average transmission of 7% of the gold film for the CIS QDs emission band of 580-900 nm. We attribute this 25% reduction to PL intensity quenching by the gold film. This finding is consistent with a slightly faster decay of the gold film sample as shown in Figure 5.3A. In stark contrast, the PL intensity of QD solution transmitted through the nanocup array is observed to be 13.5% of that of the QD solution on glass coverslip. Since this value is 2.7 times higher than an average transmission of 5% of the nanocup array for the 580-900 nm band, we conclude that the nanocup array enhances the PL intensity of the QD solution by 2.7 times. Meanwhile, the average PL decay rate for the nanocup array sample is enhanced by 4.4 times relative to that the reference glass sample (Figure 5.3A and Table 5.2), suggesting an effective enhancement in PL decay rate due to the plasmonic nanostructure. Taking into account the enhanced PL intensity and the PL average decay rate shown above, the enhancement of the radiative decay rate due to the nanocup array can be estimated to be 11.8. These results clearly demonstrate effective enhancement in both PL intensity and decay rate due to the plasmonic effect by the nanocup array.

Table 5.1. Spectrally resolved PL decay lifetime components, τ_i, and amplitude, A_i, of CIS QDs on the glass coverslip and in the gold nanocup array, fitted to four exponential functions, at different PL emission bands.

	625-645 nm		**660-683 nm**		**692-705 nm**		**720-740 nm**		**777-790 nm**	
	glass	nanocup	glass	nanocup	glass	nanocup	glass	nanocup	glass	nanocup
τ_1(ns)/A_1	1.57/0.54	1.44/0.54	2.9/0.31	2.9/0.48	5.81/0.27	2.79/0.45	4.47/0.11	3.8/0.49	7.75/0.27	4.9/0.5
τ_2(ns)/A_2	7.72/0.31	7.34/0.32	18.5/0.33	17.6/0.32	37.0/0.30	17.0/0.31	28.4/0.26	20.5/0.27	46.7/0.24	25.5/0.27
τ_3(ns)/A_3	46.6/0.11	46.0/0.1	107/0.26	109/0.14	174/0.34	114/0.16	166/0.43	104/0.14	105/0.38	147/0.15
τ_4(ns)/A_4	239/0.04	252/0.04	392/0.1	386/0.06	558/0.09	406/0.08	500/0.2	392/0.1	629/0.11	515/0.08
τ_{avg} (ns)	17.9	17.8	74.0	45.4	122.0	57.2	179.2	61.1	122.2	72.5

To further probe the plasmon-exciton coupling effect between the CIS QDs and the nanocup array, we performed spectrally resolved PL decay measurement for emission bands labeled in Figure 5.2. Figure 5.3B and Table 5.1, respectively, display the spectrally resolved PL decay curves and corresponding four exponential fitting results for the CIS QD solution on the glass coverslip and in the nanocup array. For the PL band of 625-645 nm, which is off-resonance with the EOT band of the nanocup array, the decay of the QDs in the nanocups is almost the same as that of the QDs on the glass, suggesting the absence of an effective plasmonic enhancement. With the wavelength approaching the EOT band peaking around 720 nm, the decays of the QDs in the nanocup array become faster. This trend manifests more clearly in Figure 5.3C, which shows the zoomed-in decays in the first 100 ns for decays in Figure 5.3B. Table 5.1 shows that not only the time constant of each decay component of the QDs coupled to the nanocups decreases compared to those on the glass, but also the amplitude of the fastest decay component increases with complementary decreases in amplitudes of the two slowest decay components. Specifically, when the QDs going from on-glass to in-nanocups, the amplitude of the fastest component (A_1) increases from 0.31 to 0.48 for the 660-683 nm band, from 0.27 to 0.45 for the 692-705 nm band, from 0.11 to 0.49 for the 720-740 nm band, and from 0.27 to 0.5 for the 777-790 nm band, respectively. Correspondingly, the second slowest decay component (A_3) decreases from 0.26 to 0.14, from 0.34 to 0.16, from 0.43 to 0.14, and from 0.38 to 0.15 for the four wavelength bands, respectively. For our ensemble PL measurement these decay amplitudes represent the population fractions of QDs sub-ensembles, which decay with the corresponding time constants. The increases of A_1s can therefore be interpreted as an increase of the fast-decaying QD population resulting from the plasmonic enhancement of the decay rate of the QDs, which originally decays with much slower time constants. This interpretation further leads to a conclusion that for those QDs decaying with the two slowest time constants (i.e., τ_3 and τ_4), the highest possible decay rate enhancement can be estimated from the ratio of τ_3 or τ_4 measured on glass to τ_1 measured in nanocups [9,22,28], yielding very high enhancement factors of ~40 (= 166/3.8) and ~130 (= 500/3.8) for the 720-740 nm band, respectively.

Considering that the change of A_4 is relatively smaller compared to that of A_3 for QDs going from glass to nanocups, the enhancement by ~40 would be a conservative value for the coupled system.

5.3.3 Optical simulations

In support of the experimental results, we performed numerical simulations of gold nanocup arrays. The nanocup structure is assumed to be periodic in the *xy*-plane with a triangular lattice symmetry having a period (a) ~750 nm, and is surrounded by perfectly matched layers (PML) in the *z*-directions as shown in Figure 5.4A. The radius (r) and depth (d) of the nanocup is chosen to be 250 nm and 120 nm respectively to match the experimental structure. The nanocup is coated with 65 nm thick gold layer on the top, and the thickness of gold decreases gradually as nanocup tapers leaving an ultrathin (5 nm) gold layer at the nanocup bottom. A uniform grid size of 3 nm is used in the three dimensions which is sufficient for convergence. For obtaining the transmission and reflectance spectra, the structure is illuminated with a normally incident plane wave source with wavelength spectrum ranging from 400 nm to 1100 nm incremented in steps of ~2 nm. Figure 5.4B shows the simulated extraordinary transmission spectrum calculated using Lumerical FDTD solution software for the nanocup structure with resonance peak wavelength λ_{res} ~720 nm. The transmission peak at ~520 nm is due to the characteristic gold surface-plasmon resonance, whereas the substrate-induced peak at ~1000 nm is due to gold–(PS/glass) interface at a wavelength $\lambda_{sub} \approx n \cdot \lambda_{res}$ where $n = 1.45$ for glass. The Wood's anomaly where the parallel component of the incident wave-vector lies in the plane of the grating, discussed in detail in our previous publication [33], also appears at the wavelength $\lambda_W \sim \sqrt{3}a/2 = 650$ nm (a is the structure period ~750 nm). The simulated peaks in the transmission spectrum match the corresponding dips in the reflectance spectrum. The positions of the peaks in the simulated transmission spectra agree very well with the experimentally measured data (Figure 5.1C), except for some differences in the peak intensity. These might be due to minute structural irregularities, whereas the simulation assumes a perfect geometry. We also perform the simulations to investigate the effect of changing the nanocup periodicity (a), radius (r), and depth (d) on the optical properties of the structure (see SI). Since the EOT peak position is strongly dependent on the array periodicity, the peak red-shifts (blue-shifts) on increasing (decreasing) the period. Increasing the nanocup radius while keeping the period constant increases the FWHM width and transmission intensity of the EOT peak due to increase in nanocup aperture [45]. Changing the nanocup depth, however, does not significantly affect the optical properties of the nanocup array. We then modeled the electric field intensity inside the nanocup at the resonance wavelength ~720 nm. As displayed in Figure 5.4C, the electric field intensity is enhanced significantly by a factor exceeding 100 for *hot* regions near the bottom of the nanocup.

Since it has been well established that a QD can be modeled using a classical dipole source in a first approximation [46,47], we consider a dipole source residing in the gold nanocup cavity similar to the experimental structure. The emission wavelength of the dipole source is set to vary from 650 nm to 850 nm to match the measured emission wavelength of CIS QDs (Figure 5.2B). Since in the experiment the CIS QDs in solution are randomly located at different positions inside the nanocups, we next varied the distance (d) of the dipole source from the bottom of the nanocup to the top and calculated the Purcell factor (P) for x, y, and z oriented dipoles (Figure 5.4A). The average Purcell factor for randomly oriented dipoles is obtained by summing the contribution from dipoles oriented in the three directions as <*P*> = 1/3 ($P_x + P_y + P_z$). Figure 5.4D shows the effect of moving the dipole from nanocup bottom to the top region. The Purcell factor enhancement from *z*-oriented dipole normal to the nanocups is the highest indicating stronger coupling to the enhanced field. In addition, we find that P_x and P_y are the same, which is expected since the nanocup has a rotational symmetry about the *z*-axis, thereby making *x* and *y* dipole orientations identical. As expected the <*P*> is the highest (~86) when the dipole is close to the bottom of the nanocup since there would be strongest coupling of the dipole with the enhanced electric field intensity, and is expected for low filling density of QDs. This highest <*P*> value is roughly close to the upper limit of enhancement factor of ~130 as we approximately deduced from experiment. As it moves towards the top of nanocup cavity, <*P*> decreases exponentially to ~2 indicating the weakest coupling due to the much diminished plasmonic field in that region (Figure 5.4C). The variation in <*P*> reveals a broad distribution of coupling efficiency between the CIS QDs and the hot regions inside the nanocups. From the simulations we extract an average Purcell factor over the height of the nanocup to be ~3-15 (see SI). This value is in reasonable agreement with the enhancement of average decay rates of 3 which is calculated from the ratios of τ_{avg}s of 720-740 nm band. It is worth noting that the decay of the Purcell factor with distance (*d*) above the nanocup bottom for the dipole source, follows an approximately exponential behavior $\langle P(d) \rangle \approx \exp(-d/\zeta)$ with a decay length ζ ~23 nm (see SI). This decay length corresponds to well-established SPP decay length at the gold-air interface ($\lambda/2\pi n_2 \approx 28$ nm) for wavelength $\lambda_{res} \approx 720$ nm.

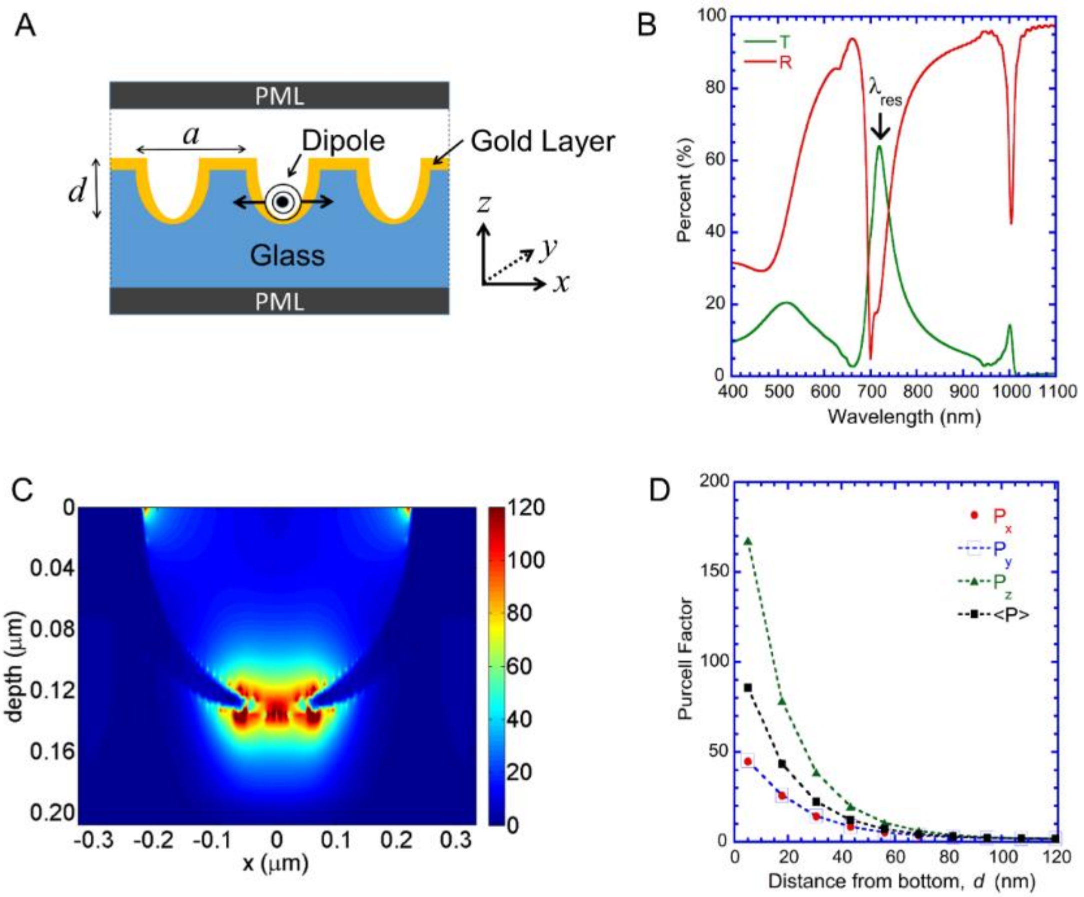

Figure 5.4. (A) Schematic showing the simulated structure utilizing a non-uniform gold coating on the nanocup array with an *x*-oriented dipole source. The period, *a*, of the structure is ~ 750 nm and depth, *d*, is ~ 120 nm. (B) Simulated transmission and reflection spectra of the nanocup structure. (C) The electric field intensity distribution in the *xz*-plane inside the nanocup at λ_{res} ~ 720 nm. (D) Evolution of Purcell factor for *x*, *y* and *z* oriented dipole as a function of its distance from the bottom of the nanocup. P_x and P_y overlap due to the rotational symmetry of nanocup along *z*-axis.

5.4 Conclusion

In summary, we experimentally and theoretically demonstrate strong coupling of non-toxic CIS QDs in solution to plasmonic gold nanocup array structures. The nanocups exhibit extraordinary optical transmission, and strong enhancement of electric fields (by ~100), at resonance wavelengths. The QDs strongly couple to the enhanced field to produce a fast decay rate measured with time-resolved PL. The measured enhancement factor of PL decay rate of QDs represents an average of all locations of the QD within the nanocup. FDTD simulations indicate that the PL decay rate can be enhanced by almost two orders-of-magnitude in the effectively coupled hot regions near the bottom of the nanocups, in agreement with our experimental estimation. The solution-based exciton-plasmon coupled system between the biocompatible CIS QDs and the gold nanocup array could be useful for applications such as biological sensing. Furthermore, the fundamental understanding on plasmonic PL enhancements of CIS QDs demonstrated in this work could motivate researchers to develop other CIS QD-metal nanostructures coupled systems that are more appropriate for biological sensing and imaging applications.

5.5 Experimental Section

5.5.1 Fabrication of gold nanocup arrays

The gold-coated periodic nanocup arrays were fabricated using the method described in detail in one of our previous publication. Briefly, we started with a polycarbonate master (Microcontinuum Inc., MA) pattern consisting of periodic array of tapered nanocups with a period of ~ 750 nm. The inverse of this polycarbonate master was transferred onto the PDMS mold using soft lithographic replication process. For preparing the PDMS mold, prepolymer and curing agent (Dow Corning, Sylgard 184) were mixed in ratio of 10:1 by weight followed by degassing to remove any air bubbles. The mixture was then poured directly on the polycarbonate master and left to cure at room temperature for 48 hours. The PDMS mold was then peeled off the master to obtain an array of periodic nanocones. This PDMS mold was used to imprint the polystyrene films spin-coated over the glass substrate. For preparing polystyrene-coated glass substrates, polystyrene beads (Sigma Aldrich, average molecular weight 35,000) were dissolved in toluene to form a solution with 2% w/v concentration. The solution was then spin-coated over the glass substrate (500 rpm, 60 seconds) to form a thin film. After allowing the film to dry for ~12 hours, the PDMS stamp was placed on the PS films over the glass substrate so that the patterned PDMS stamp faces the polystyrene film. The PDMS stamp was further pressed down by another glass slide having the same size as substrate, and the assembly was held together with two binder clips at each end. The whole assembly was placed in an oven at ~170°C, a temperature higher than the glass transition temperature (T_g) of PS (~100°C), for 45 minutes. After allowing it to cool at room temperature for 12 hours, the PDMS stamp was removed carefully from the PS film to reveal the inverse replica of the pattern on it. This was followed by angle-directed sputter deposition of thin gold film ~70 nm on the nanocup substrate. The sample was placed at an angle of 45 degrees to the vertical and rotated so as to have non-conformal coating of gold over the nanocup sidewalls. This coating method ensures that the deposited gold is thicker at the top sidewalls and becomes thinner as we move towards the bottom of the nanocup. The gold-coated nanocup structure was characterized using scanning electron microscopy and atomic force microscopy as shown in Figure 5.1. As it can be seen from Figure 5.1A, periodic array of nanocups with period ~750 nm and diameter ~500 nm have been replicated with high fidelity on the polystyrene substrate. The AFM linescan in Figure 5.1B shows the depth of nanocups ~120 nm.

5.5.2 Synthesis of $CuInS_2/ZnS$ nanocrystals

Copper(I) acetate (Cu(Ac), 97%), zinc acetate ($Zn(Ac)_2$), indium acetate ($In(Ac)_3$, 99.99%), 1-dodecanethiol (1-DDT, 98%), Oleylamine (OAm, ≥98%), 1-octadecene (ODE, 90%), oleic acid (OA, 90%) were purchased from Sigma Aldrich and used without further purification. $CuInS_2$/ZnS nanocrystals were synthesized using pervious published procedure with slight modification.[17] Briefly, Cu(Ac) (0.2 mmol) and $In(Ac)_3$ (0.18 mmol) were mixed with 1-DDT (2 mL, 8.35 mmol), OA (0.3mL) and ODE (3 mL) in 3-necked flask under an inert atmosphere. The reaction mixture was degassed at room temperature for 15-30 minutes and then heated to 100°C under argon flow for 10-12 min until a clear solution was formed. Next, the flask was heated to 275°C and retained at this temperature for 15 min with continuous stirring to allow the CIS nanocrystal growth. The color of the reaction solution gradually changed during heating from light yellow to red and then dark brown/black. Afterward, the reaction solution was cooled to 230 °C for the ZnS shell growth. To make the Zn precursor solution, $Zn(Ac)_2$ (2 mmol) was loaded in the 3-neck flask with ODE (4 mL) and OAm (1 mL). The reaction mixture was heated to 100 °C and degassed for 15-30 minutes followed by heating to 160 °C under argon flow to make optical clear solution. After that the solution was cooled to 60 °C for further use. The ZnS shell growth was performed by injecting the zinc precursor slowly into the CIS nanocrystal growth solution and the temperature was maintained at 230 °C for 30 min. Nanocrystal growth was terminated by removing the heating mantel, and at 90 °C, anhydrous toluene (2-3 mL) was added to quench the reaction. The $CuInS_2$/ZnS nanocrystal was purified using toluene/ethanol mixture and re-suspended in toluene or hexane/dichlorobenzene for further measurements. The solution used for the nanocup arrays is in a solvent mixture of hexane and dichlorobenzene (1:9 in volume ratio), with a concentration of ~ 7.7 μM estimated based on the measured absorbance and the literature reported molar extinction coefficient [48].

5.5.3 Optical spectroscopy

The PL emission experiments were carried out on a typical wide-field optical microscope. A pulsed 403 nm laser beam focused to a spot size with diameter of ~ 40 μm was used to excite the samples from the top. The PL emission from the other side of the samples was collected with a 100×, 0.85 NA objective lens and cleaned with long pass filters. The time resolved PL was detected with a single photon avalanche photodiode (SPAD, SPCM-AQR-14, PerkinElmer) connected with a Hydraharp 400 TCSPC system. To collect spectrally resolved PL decays, Semrock VersaChrome tunable bandpass filter (TBP01-697/13, Semrock) or a combination of short and long pass filters were placed in front of the SPADs. The fitting of the PL decays was conducted using Igor program. During typical spectroscopy tests (usually within ~2 hours), we did not observe detectable PL degradation of QD solution in the nanocup array. This good stability might results the fact that the QDs are in solution (that is, not exposed to air or moisture) that fills the nanocup array. Moreover, several batches of nanocup array sample have been fabricated in this study and good repeatability in both nanocup structures and PL enhancement have been obtained.

5.6 Supporting Information

5.6.1 PL decay curves fitting

The decay curves can be well fitted to a four exponential function which can be expressed as:

$$N = A_1 e^{-t/\tau_1} + A_2 e^{-t/\tau_2} + A_3 e^{-t/\tau_3} + A_4 e^{-t/\tau_4} \tag{5.1}$$

where A_1, A_2, A_3, A_4 and τ_1, τ_2, τ_3, τ_4 correspond to the amplitude and lifetime of each decay component, respectively.

The amplitude-weighted average lifetime is computed by using the following expression:

$$\tau_{avg} = A_1\tau_1 + A_2\tau_2 + A_3\tau_3 + A_4\tau_4 \tag{5.2}$$

Table 5.2. Multiexponential fitting results for decays shown in Figure 5.3A in the main text.

	glass	**gold film**	**nanocup**
τ_1(ns)/A_1	5.8/0.13	3.6/0.32	3.4/0.49
τ_2(ns)/A_2	28.6/0.23	23.2/0.25	18.6/0.24
τ_3(ns)/A_3	190/0.46	131/0.27	84.7/0.21
τ_4(ns)/A_4	585/0.18	439/0.16	365/0.06
τ_{avg}(ns)	200.0	112.6	45.8

5.6.2 Effect of changing nanocup periodicity

We investigate the effect of changing the nanocup periodicity on the EOT peak position by simulating four different periods (a) = 650 nm, 700 nm, 750 nm, and 800 nm for a constant nanocup radius (r) of 250 nm and depth (d) of 120 nm. It can be seen from Figure 5.5 that the surface plasmon resonance peak due to gold appears at the same wavelength ~504 nm for all the structures with different periodicities. However, the position of EOT peak (λ_{res}) red-shifts when the period of the structure increases, indicating the strong dependence of EOT peak on nanocup periodicity. The corresponding position of the substrate peak (λ_{subs}) also scales accordingly with the period.

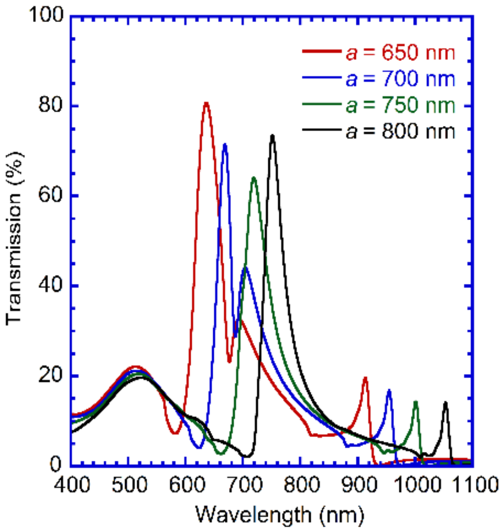

Figure 5.5. Simulated transmission spectra for the nanocup structure with different periods (*a*) = 650 nm, 700 nm, 750 nm, and 800 nm. The nanocup radius is 250 nm and depth is 120 nm for all the cases. The EOT peak red-shifts (blue-shifts) on increasing (decreasing) the nanocup period.

5.6.3 Effect of changing nanocup radius

We investigate the effect of changing the nanocup radius on the optical properties of the structure by simulating three different nanocup radii (*r*) = 150 nm, 200 nm, and 250 nm while keeping the period (*a*) and depth (*d*) constant. The filling ratio (or the density) for the nanocup array arranged in triangular lattice, given by the following expression, can be changed by varying the nanocup radius (Table 5.3).

$$f = \frac{\pi r^2}{\left(\sqrt{3}a^2/2\right)} = \frac{2\pi}{\sqrt{3}}\left(\frac{r}{a}\right)^2 \tag{5.3}$$

Table 5.3. Filling ratio of nanocups for different values of *r*/*a*.

Radius (*r*)	**Period (*a*)**	***r*/*a***	***f***
150 nm	750 nm	0.20	0.145
200 nm	750 nm	0.27	0.258
250 nm	750 nm	0.33	0.403

The simulated transmission spectra presented in Figure 5.6 show that decreasing the nanocup radius narrows the EOT peak while decreasing the transmission intensity at the same time. This is because the nanocup aperture decreases resulting in less transmission through the nanocup array. However, it is to be noted that the position of EOT peak and the weaker substrate peak slightly blue-shift with decreasing radius for same nanocup period of 750 nm. As expected the gold surface plasmon peak at ~504 nm remains unaffected.

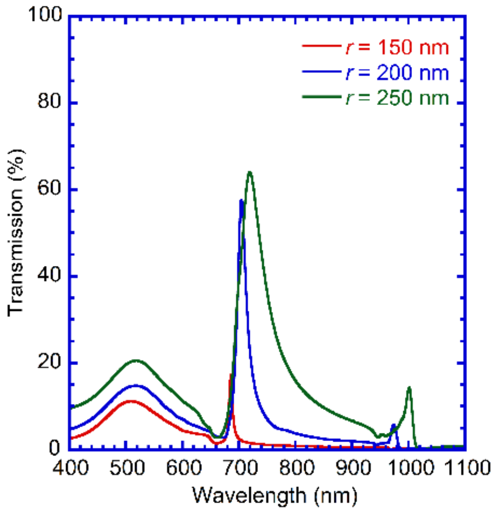

Figure 5.6. Simulated transmission spectra for the nanocup structure with different radii (r) = 150 nm, 200 nm, and 250 nm. The nanocup periodicity is 750 nm and depth is 120 nm for all the cases.

5.6.4 Effect of changing nanocup depth

We investigate the effect of changing the nanocup depth on the optical properties of the structure by simulating three different nanocup depths (d) = 60 nm, 120 nm, and 180 nm while keeping the periodicity (a) and radius (r) constant. As shown in Figure 5.7, it can be seen that varying the nanocup depth does not have significant effect on the plasmonic performance of the nanocup array with EOT peaks appearing at the same wavelength with nearly similar transmission intensities.

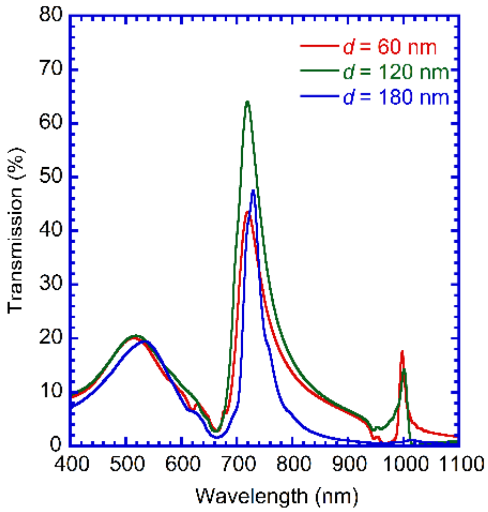

Figure 5.7. Simulated transmission spectra for the nanocup structure with different depths (*d*) = 60 nm, 120 nm, and 180 nm. The nanocup periodicity is 750 nm and radius is 250 nm for all the cases.

5.6.5 Average Purcell factor calculation

The Purcell factor averaged over the height of nanocup is calculated to be ~3-15. To extract the Purcell factor, we vary the height of the dipole in the *z*-direction placed inside the nanocup for two different *x* positions while keeping the *y*-position fixed (*y*=0). For the dipole placed at *x*=0 and varying height, the Purcell factor averaged over the nanocup height is ~15 (Figure 5.8A). It is noteworthy that the Purcell factor approaches ~86 for QDs at the bottom of the nanocup, which may be expected for low filling density of the QDs.

When the dipole is displaced 100 nm from the *x*=0 position as shown in Figure 5.8B, the average Purcell factor over the heights of the dipole decreases to ~3. For this displaced configuration, the highest Purcell factor (<*P*>) for the dipole closest to the nanocup bottom is ~11 and it drops exponentially to ~2 as the height of the dipole from the bottom increases (Figure 5.9). It is noteworthy that the P_x and P_y are slightly different for this configuration as opposed to the dipole placed at *x*=0. This is because the nanocup with the dipole is not symmetric anymore about *z*-axis resulting in slightly different Purcell factor values for *x* and *y* orientations. This drop in Purcell factor for the displaced dipole is quite intuitive since the electric field intensity has a maximum in the center of the nanocup which is the point of maximum plasmonic coupling. However, for the electric dipole placed at *x*=100 nm from central axis, the plasmonic coupling is not as efficient resulting in a decrease in average Purcell factor. Since QDs are expected to be present everywhere inside the nanocup cavity from the experiment, Purcell factor should ideally be calculated for all the orientations of the dipoles averaged over the entire volume of the nanocup cavity. However, such calculation requires positioning the dipole over the entire cavity volume in suitable grid and is highly computationally intensive requiring large number of simulation runs with this FDTD method. In order to get a rough estimate of how the Purcell factor changes with the different positions of dipoles, we follow this method by selecting two representative positions in the *x*-direction and extract an average range of ~3-15, which approximates the limit of high filling density of the QDs.

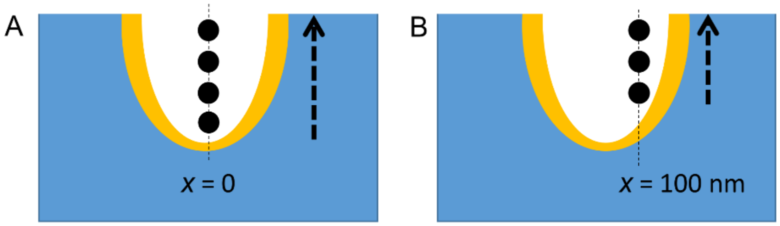

Dipole moved along *z*-direction to get average Purcell factor over heights of dipole

Figure 5.8. Average Purcell factor over the heights of dipole placed in the nanocup cavity. The dipole is placed at (A) *x*=0 and (B) *x*=100 nm, and the height is varied in *z*-direction.

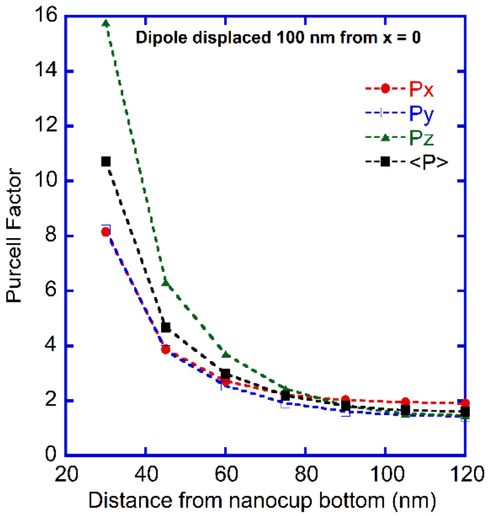

Figure 5.9. Evolution of Purcell factor for *x*, *y* and *z* oriented dipole initially displaced to *x*=100 nm from the central axis as a function of its distance from the bottom of the nanocup.

5.6.6 Purcell factor decay

Since the decay of average Purcell factor as a function of distance (*d*) from the nanocup bottom follows an approximately exponential behavior $<P(d)> \sim \exp(-d/\zeta)$, we plot $ln<P(d)>$ as a function of *d* in Figure 5.10.

$$\ln < P(d) >= A - {}^{d}\!/\!_{\zeta} \tag{5.4}$$

We see that the curve is approximately a straight line with the slope $1/\zeta \sim 0.0437$, giving a decay length $\zeta \sim 23$ nm.

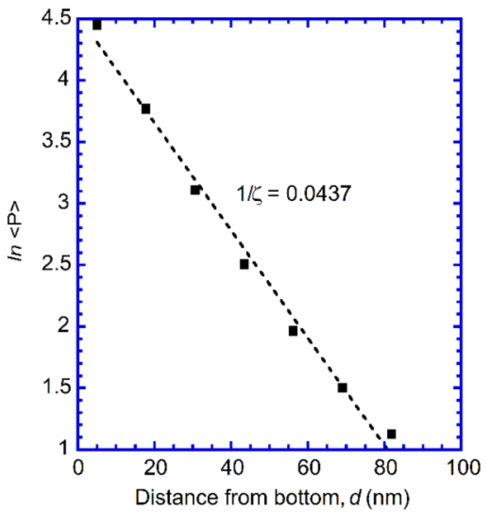

Figure 5.10. *ln* <*P*(*d*)> as a function of distance from the nanocup bottom. The slope of the straight line is 1/ζ = 0.0437.

5.7 Acknowledgements

This work was performed, in part, at the Center for Integrated Nanotechnologies, an Office of Science User Facility operated for the U.S. Department of Energy (DOE) Office of Science by Los Alamos National Laboratory (Contract No. DE-AC52-06NA25396) and Sandia National Laboratories (Contract No. DE-NA-0003525), in support of User Projects 2016AU0125 and 2016ARA0013. This work was also supported in part (R.B. and A.P.) by the U.S. DOE Office of Science, Basic Energy Sciences, Materials Science and Engineering Division. Ames Laboratory is operated for the U.S. DOE by Iowa State University under Contract No. DE-AC02-07CH11358. A.P., Z.H., J.A.H., and H.H. acknowledge support of Los Alamos National Laboratory, Laboratory Directed Research and Development Funds. A.S. gratefully acknowledges a Director's Postdoctoral Fellowship support from Los Alamos National Laboratory. The authors thank Dr. Jinkyoung Yoo for allowing us to use Lumerical FDTD Solutions software and Jon Baldwin for gold deposition.

5.8 References

1. D. K. Gramotnev and S. I. Bozhevolnyi, “Plasmonics beyond the diffraction limit,” *Nat. Photon.* **4**, 83-91 (2010).

2. S. A. Maier, M. L. Brongersma, P. G. Kik, S. Meltzer, A. A. G. Requicha and H. A. Atwater, “Plasmonics—A Route to Nanoscale Optical Devices,” *Adv. Mater.* 13, 1501-1505 (2001).

3. E. Ozbay, “Plasmonics: Merging Photonics and Electronics at Nanoscale Dimensions,” *Science* **311**, 189-193 (2006).

4. J. A. Schuller, E. S. Barnard, W. S. Cai, Y. C. Jun, J. S. White and M. L. Brongersma, “Plasmonics for extreme light concentration and manipulation,” *Nat. Mater.* **9**, 193-204 (2010).

5. A. G. Curto, G. Volpe, T. H. Taminiau, M. P. Kreuzer, R. Quidant and N. F. van Hulst, “Unidirectional Emission of a Quantum Dot Coupled to a Nanoantenna,” *Science* **329**, 930-933 (2010).

6. A. V. Akimov, A. Mukherjee, C. L. Yu, D. E. Chang, A. S. Zibrov, P. R. Hemmer, H. Park and M. D. Lukin, “Generation of single optical plasmons in metallic nanowires coupled to quantum dots,” *Nature* **450**, 402-406 (2007).

7. M. S. Tame, K. R. McEnery, S. K. Oezdemir, J. Lee, S. A. Maier and M. S. Kim, “Quantum plasmonics,” *Nat. Phys.* **9**, 329-340 (2013).

8. F. Wang, N. S. Karan, N. Hue Minh, B. D. Mangum, Y. Ghosh, C. J. Sheehan, J. A. Hollingsworth and H. Htoon, “Quantum Optical Signature of Plasmonically Coupled Nanocrystal Quantum Dots,” *Small* **11**, 5028-5034 (2015).

9. T. B. Hoang, G. M. Akselrod, C. Argyropoulos, J. Huang, D. R. Smith and M. H. Mikkelsen, “Ultrafast spontaneous emission source using plasmonic nanoantennas,” *Nat. Commun.* **6**, 7788 (2015).

10. Q. Li, H. Wei and H. Xu, “Quantum Yield of Single Surface Plasmons Generated by a Quantum Dot Coupled with a Silver Nanowire,” *Nano. Lett.* **15**, 8181-8187 (2015).

11. B. Ji, E. Giovanelli, B. Habert, P. Spinicelli, M. Nasilowski, X. Xu, N. Lequeux, J.-P. Hugonin, F. Marquier, J.-J. Greffet and B. Dubertret, “Non-blinking quantum dot with a plasmonic nanoshell resonator,” *Nat. Nanotechnol.* **10**, 170-175 (2015).

12. A. C. Berends, F. T. Rabouw, F. C. M. Spoor, E. Bladt, F. C. Grozema, A. J. Houtepen, L. D. A. Siebbeles and C. M. Donega, “Radiative and Nonradiative Recombination in $CuInS_2$ Nanocrystals and $CuInS_2$-Based Core/Shell Nanocrystals” *J. Phys. Chem. Lett.* **7**, 3503-3509 (2016).

13. D. H. Jara, K. G. Stamplecoskie and P. V. Kamat, “Two Distinct Transitions in Cu_xInS_2 Quantum Dots. Bandgap versus Sub-Bandgap Excitations in Copper-Deficient Structures,” *J. Phys. Chem. Lett.* **7**, 1452-1459 (2016).

14. K. F. Wu, G. J. Liang, D. G. Kong, J. Q. Chen, Z. Y. Chen, X. H. Shan, J. R. McBride and T. Q. Lian, “Quasi-type II $CuInS_2$/CdS core/shell quantum dots,” *Chem. Sci.* **7**, 1238-1244 (2016).

15. H. Zang, H. Li, N. S. Makarov, K. A. Velizhanin, K. Wu, Y.-S. Park and V. I. Klimov, “Thick-Shell $CuInS_2$/ZnS Quantum Dots with Suppressed "Blinking" and Narrow Single-Particle Emission Line Widths,” *Nano. Lett.* **17**, 1787-1795 (2017).

16. K. Qi, Y. Wang, R. Wang, D. Wu and G.-D. Li, “Facile synthesis of homogeneous $CuInS_2$ quantum dots with tunable near-infrared emission,” *J. Mater. Chem. C* **4**, 1895-1899 (2016).

17. D. Deng, Y. Chen, J. Cao, J. Tian, Z. Qian, S. Achilefu and Y. Gu, “High-Quality $CuInS_2$/ZnS Quantum Dots for In vitro and In vivo Bioimaging,” *Chem. Mater.* **24**, 3029-3037 (2012).

18. A. D. P. Leach and J. E. Macdonald, “Optoelectronic Properties of $CuInS_2$ Nanocrystals and Their Origin,” *J. Phys. Chem. Lett.* **7**, 572-583 (2016).

19. K. E. Knowles, K. H. Hartstein, T. B. Kilburn, A. Marchioro, H. D. Nelson, P. J. Whitham and D. R. Gamelin, “Luminescent Colloidal Semiconductor Nanocrystals Containing Copper: Synthesis, Photophysics, and Applications,” *Chem. Rev.* **116**, 10820-10851 (2016).

20. Q. Rice, S. Raut, R. Chib, A. Hayes, Z. Gryczynski, I. Gryczynski, Y.-K. Kim, B. Tabibi and J. Seo, “Defect-mediated spontaneous emission enhancement of plasmon-coupled $CuInS_2$ and $CuInS_2$/ZnS,” *Opt. Mater. Express* **6**, 566-577 (2016).

21. K. Weiguang, Z. Bingpo, L. Ruifeng, W. Feifei, X. Tianning and W. Huizhen, “Plasmon enhanced fluorescence from quaternary Cu-In-Zn-S quantum dots,” *Appl. Surf. Sci.* **327**, 394-399 (2015).

22. K. Tawa, X. Cui, K. Kintaka, J. Nishii and K. Morigaki, “Sensitive bioimaging in microfluidic channels on the plasmonic substrate: Application of an enhanced fluorescence based on the reverse coupling mode,” *J. Photoch. Photobio. A* **221**, 261-267 (2011).

23. A. G. Brolo, S. C. Kwok, M. G. Moffitt, R. Gordon, J. Riordon and K. L. Kavanagh, “Enhanced Fluorescence from Arrays of Nanoholes in a Gold Film,” *J. Am. Chem. Soc.* **127**, 14936-14941 (2005).

24. M. Li, S. K. Cushing and N. Wu, “Plasmon-enhanced optical sensors: a review,” *Analyst* **140**, 386-406 (2015).

25. T. W. Ebbesen, H. J. Lezec, H. F. Ghaemi, T. Thio and P. A. Wolff, "Extraordinary optical transmission through sub-wavelength hole arrays," *Nature* **391**, 667-669 (1998).

26. H. F. Ghaemi, T. Thio, D. E. Grupp, T. W. Ebbesen and H. J. Lezec, "Surface plasmons enhance optical transmission through subwavelength holes," *Phys. Rev. B* **58**, 6779-6782 (1998).

27. H. Wang, H.-Y. Wang, A. Toma, T.-a. Yano, Q.-D. Chen, H.-L. Xu, H.-B. Sun and R. Proietti Zaccaria, "Dynamics of Strong Coupling between CdSe Quantum Dots and Surface Plasmon Polaritons in Subwavelength Hole Array," *J. Phys. Chem. Lett.* **7**, 4648-4654 (2016).

28. A. G. Brolo, S. C. Kwok, M. D. Cooper, M. G. Moffitt, C. W. Wang, R. Gordon, J. Riordon and K. L. Kavanagh, "Surface Plasmon−Quantum Dot Coupling from Arrays of Nanoholes," *J. Phys. Chem. B* **110**, 8307-8313 (2006).

29. N. Bonod, S. Enoch, L. F. Li, E. Popov and M. Neviere, "Resonant optical transmission through thin metallic films with and without holes," *Opt. Express* **11**, 482-490 (2003).

30. B. Ai, Y. Yu, H. Moehwald, L. Wang and G. Zhang, "Resonant Optical Transmission through Topologically Continuous Films," *ACS Nano* **8**, 1566-1575 (2014).

31. L. Wang, B. Ai, H. Moehwald, Y. Yu and G. Zhang, "Invertible Nanocup Array Supporting Hybrid Plasmonic Resonances," *Adv. Opt. Mater.* **4**, 906-916 (2016).

32. D. Gerard, L. Salomon, F. de Fornel and A. V. Zayats, "Ridge-enhanced optical transmission through a continuous metal film," *Phys. Rev. B* **69**, 113405 (2004).

33. A. Peer and R. Biswas, "Extraordinary optical transmission in nanopatterned ultrathin metal films without holes," *Nanoscale* **8**, 4657-4666 (2016).

34. H. A. Bethe, "Theory of Diffraction by Small Holes," *Phys. Rev.* **66**, 163-182 (1944).

35. A. E. Cetin, A. F. Coskun, B. C. Galarreta, M. Huang, D. Herman, A. Ozcan and H. Altug, "Handheld high-throughput plasmonic biosensor using computational on-chip imaging," *Light: Science & Applications* **3**, e122 (2014).

36. R. Gordon, D. Sinton, K. L. Kavanagh and A. G. Brolo, "A New Generation of Sensors Based on Extraordinary Optical Transmission," *Acc. Chem. Res.* **41**, 1049-1057 (2008).

37. M. Wang, C. Zhao, X. Miao, Y. Zhao, J. Rufo, Y. J. Liu, T. J. Huang and Y. Zheng, "Plasmofluidics: Merging Light and Fluids at the Micro-/Nanoscale," *Small* **11**, 4423-4444 (2015).

38. L. Martin-Moreno, F. J. Garcia-Vidal, H. J. Lezec, K. M. Pellerin, T. Thio, J. B. Pendry and T. W. Ebbesen, "Theory of Extraordinary Optical Transmission through Subwavelength Hole Arrays," *Phys. Rev. Lett.* **86**, 1114-1117 (2001).

39. P. J. Whitham, A. Marchioro, K. E. Knowles, T. B. Kilburn, P. J. Reid and D. R. Gamelin, "Single-Particle Photoluminescence Spectra, Blinking, and Delayed Luminescence of Colloidal $CuInS_2$ Nanocrystals," *J. Phys. Chem. C* **120**, 17136-17142 (2016).

40. V. K. Komarala, C. Xie, Y. Q. Wang, J. Xu and M. Xiao, "Time-resolved photoluminescence properties of $CuInS_2$/ZnS nanocrystals: Influence of intrinsic defects and external impurities," *J. Appl. Phys.* **111**, 124314 (2012).

41. J. Sun, M. Ikezawa, X. Wang, P. Jing, H. Li, J. Zhao and Y. Masumoto, "Photocarrier recombination dynamics in ternary chalcogenide $CuInS_2$ quantum dots," *Phys. Chem. Chem. Phys.* **17**, 11981-11989 (2015).

42. H. Zhong, Y. Zhou, M. Ye, Y. He, J. Ye, C. He, C. Yang and Y. Li, "Controlled Synthesis and Optical Properties of Colloidal Ternary Chalcogenide $CuInS_2$ Nanocrystals," *Chem. Mater.* **20**, 6434-6443 (2008).

43. L. Li, A. Pandey, D. J. Werder, B. P. Khanal, J. M. Pietryga and V. I. Klimov, "Efficient Synthesis of Highly Luminescent Copper Indium Sulfide-Based Core/Shell Nanocrystals with Surprisingly Long-Lived Emission," *J. Am. Chem. Soc.* **133**, 1176-1179 (2011).

44. K. E. Knowles, H. D. Nelson, T. B. Kilburn and D. R. Gamelin, "Singlet–Triplet Splittings in the Luminescent Excited States of Colloidal Cu^+:CdSe, Cu^+:InP, and $CuInS_2$ Nanocrystals: Charge-Transfer Configurations and Self-Trapped Excitons," *J. Am. Chem. Soc.* **137**, 13138-13147 (2015).

45. R. Biswas, S. Neginhal, C. G. Ding, I. Puscasu and E. Johnson, "Mechanisms underlying extraordinary transmission enhancement in subwavelength hole arrays," *J. Opt. Soc. Am. B* **24**, 2589-2596 (2007).

46. R. Guo, S. Derom, A. I. Vakevainen, R. J. A. van Dijk-Moes, P. Liljeroth, D. Vanmaekelbergh and P. Torma, "Controlling quantum dot emission by plasmonic nanoarrays," *Opt. Express* **23**, 28206-28215 (2015).

47. O. L. Muskens, V. Giannini, J. A. Sanchez-Gil and J. G. Rivas, "Strong Enhancement of the Radiative Decay Rate of Emitters by Single Plasmonic Nanoantennas," *Nano. Lett.* **7**, 2871-2875 (2007).

48. M. Booth, A. P. Brown, S. D. Evans and K. Critchley, "Determining the Concentration of $CuInS_2$ Quantum Dots from the Size-Dependent Molar Extinction Coefficient," *Chem. Mater.* **24**, 2064-2070 (2012).

CHAPTER 6

NANOSCALE PATTERNING OF BIOPOLYMERS FOR FUNCTIONAL BIOSURFACES AND CONTROLLED DRUG RELEASE

Akshit Peer[1,2,3], Rabin Dhakal[2], Rana Biswas[1,2,3,4] and Jaeyoun Kim[1,2]

1. Microelectronics Research Center, Iowa State University, Ames IA USA 50011
2. Department of Electrical and Computer Engineering, Iowa State University, Ames, IA USA 50011
3. Ames Laboratory, Ames, IA USA 50011
4. Department of Physics and Astronomy, Iowa State University, Ames, IA USA 50011

Adapted from an article published in *Nanoscale* **8**, 18654-18664 (2016)

6.1 Abstract

We compare the rates of drug release from nanopatterned and flat biodegradable polymer surfaces, and observe significantly lower release rates from the nanopatterned surfaces. Specifically, we nanopattern poly (L-lactic acid) (PLLA), a biodegradable polymer frequently used for fabricating drug-eluting coronary stents, through microtransfer molding and solvent casting and investigate the nanopattern's impact on the release of *sirolimus*, an immunosuppresant agent, coated on the PLLA surface using high performance liquid chromatography/mass spectrometry. We find that PLLA surfaces nanopatterned with 750 nm-pitch nanocup or nanocone arrays exhibit drug release rates significantly lower (25-30%) than that of the flat surface, which is counter-intuitive given the nanopattern-induced increase

in their surface areas. Based on diffusion and meniscus curvature minimization analyses, we attribute the decreased drug release rate to the incomplete wetting of the nanopatterned surface. These results provide new insights on how surface nanopatterning of biomaterials can functionalize the surface and tailor the release kinetics of therapeutic agents coated on it for controlled drug elution.

6.2 Introduction

Periodically patterned structures have imparted profound impacts to diverse scientific disciplines. In physics, chemistry, and material science, artificially engineered photonic crystals have demonstrated unprecedented abilities to control the propagation of photons. In the field of biomaterials, it is of great interest to explore how such periodically patterned structures control diverse biological functions by varying the available surface area – a key attribute for cell growth, surface hydrophobicity, and drug delivery.

Periodically patterned arrays have been synthesized in biopolymers or ceramics [1] through 3-dimensional printing [2] or lithographic techniques [3] for diverse biomedical applications such as templates or scaffolds for bone and tissue culture [4,5]. Bioinspired multiscale periodic structures, such as nanorod-decorated micropillars, have exhibited super-wettability or extreme hydrophobicity [6] that are critical for biological functions.

There is a great interest in nanoscale surface patterning of biodegradable polymers such as poly (L-lactic acid) (PLLA), [7-10] poly (D,L-lactic acid) (PDLLA) [11-13] or poly (lactic-co-glycolic acid) (PLGA) [14-16]. Recent studies have shown that such nanopatterned materials and their fabrication techniques are playing crucial roles in the development of biomedical systems [17,18]. The nanoscale pillar arrays (400~700 nm diameter and

700~1300 nm in pitch), fabricated on PLLA substrates through the microtransfer molding technique are good examples [7]. Human tissue growth experiments on these patterned surfaces revealed that the fibroblast adhesion was enhanced on the patterned surfaces although its proliferation was lower when compared with the smooth surfaces, especially after one day [7]. The underlying mechanisms of the cell-substrate interaction on nanoscale patterned surfaces, including the characterization of the deformation of the cell nucleus [10], are under active study. In another study [12], micropatterned grooves were fabricated on an artificial scaffold of PLLA through combined use of reactive ion etching, compression molding, and solvent casting. These microgrooves, with 10-20 μm in spacing and ≥1.4 μm in depth, were found to be very effective in promoting cell adhesion and Schwann cell alignment within the grooves [13,19], which is of great significance to regeneration of nerve cells on artificial scaffolds.

PLLA has been frequently adopted for the realization of drug eluting stents in cardiac therapy. The stent is inserted into a blocked coronary artery through a balloon catheter and then subsequently expanded to re-open the artery. A common concern is *thrombosis*, or blood clot formation, which leads to the stent rejection by the body. To alleviate thrombosis, polymer-based stents loaded with anti-clotting drugs, to be eluted into the blood stream gradually, have been introduced. The critical factor is the rate at which the coated drug is eluted. The ability to control and slow down the drug release rate has been in high demand. In this work, we show that we can lower the drug release rate through nanopatterning of the PLLA surface. In earlier practice, bare Ti- metal mesh stents patterned at sub-micrometer length scale [20,21] have been utilized primarily. Another major concern is restenosis – a narrowing of the artery that restricts blood flow after stent implantation. Restenosis can also be inhibited with drug eluting stents, further emphasizing the need to control the drug release.

To evaluate the impact of nanopatterning, we first establish simple and reproducible ways to create periodic nanoscale textures on the PLLA surface. We then measured the drug release rate from these nanopatterned PLLA surfaces and compared the results with that of the flat, unpatterned control. The patterned surfaces show a remarkably slower release over a period of ten days in comparison to the control surfaces. We attribute the slower release to the nanopatterning-induced incomplete wetting of the surface, which demonstrates strong potential for morphological, not chemical, control of drug release rate.

In addition, the surface nanopatterning process we established for this work is simple and reproducible. While involving only the solvent casting process that can be performed in a common workbench, the technique can yield nanopatterns with high-level transfer fidelity. Another alternative method for generating periodic patterns is laser-induced nanotexturing with fs pulses, where the interference of incident laser light on the surface creates periodic ripples and patterns whose shape can be controlled by the pulse energies and scan rates [20]. The picosecond laser-induced microtexturing with self-assembled glass microspheres has also been used to periodically pattern silicon substrates where the enhanced optical field at the tip of glass microsphere in contact with the substrate generates enough energy to ablate the underlying substrate material [22]. Micropatterned silicon masters fabricated using photolithography or e-beam patterning have been widely used to generate periodic patterns on polymers by pattern transfer using solvent casting [12,13,19].

In contrast, one of the alternative methods for realizing random nanopatterned surfaces involves electrospun fiber meshes [23,24] which require a syringe pump with high applied voltage. Block copolymers synthesized by hydrolysis can self-assemble in arrays with nanoscale dimension [25-27] which offer another pathway for producing nanoarrays, that may lack long-range periodicity but have good short-range order.

6.3 Experimental

6.3.1 PDMS mold preparation

We started with master pattern consisting of a periodic array of nanocups or nanocones with a sub-micron pitch of 750 nm in a triangular lattice on a polycarbonate substrate (Microcontinnum Inc., MA). Each nanocup (nanocone) is approximately 500 nm in diameter and 250 nm in depth (height). Such master patterns and imprint stamps at customizable pitch and feature size can also be commercially purchased from vendors [28], without the need for in-house nanofabrication. The inverse of this pattern was transferred to a polydimethylsiloxane (PDMS) mold through replica molding [3]. For this, we mixed the PDMS elastomer base and curing agent (Sylgard 184, Dow Corning) in 10:1 w/w ratio, and the mixture was degassed to remove trapped air bubbles. The mixture was then poured directly onto the nanopatterned master polycarbonate substrate. The PDMS mold was cured at room temperature for ~48 hours and subsequently heated on a hotplate at 65°C for ~12 hours, and finally peeled off from the master substrate.

6.3.2 PLLA nanopatterning

The PDMS mold was utilized to create surface nanopatterned PLLA films by solvent casting. We prepared the PLLA solution by dissolving PLLA (Synthecon Inc., Houston, TX, MW 85,000-160,000) in chloroform. The PLLA solution was then directly drop-cast on the

PDMS mold and the resulting film was dried at room temperature for 12 hours. The dried PLLA film was then peeled off from the PDMS mold.

The suitability of chloroform as the solvent has been studied by us in advance, since the swelling of PDMS is a matter of serious concern. We found that most of the chloroform evaporates within 30 minutes of its pouring over the PDMS mold, incurring negligible swelling to PDMS. Since only 1-2 drops of chloroform have been used, its impact is minimal. We have performed separate experiments with chloroform on PDMS and confirmed that it takes more than 1 day for PDMS to swell appreciably. At around the 30 minute-point, the swelling ratio was only ~1.02. This has also been showed by an earlier study by Whitesides and co-workers [29] in which a solid PDMS piece was immersed in chloroform for 24 hours to exhibit a swelling ratio of ~1.39. Further, it is to be noted that these experiments involve immersing the entire PDMS piece in chloroform which is not the case with our process in which only a small amount of chloroform becomes in contact with PDMS. A PDMS block with a randomly rough surface has also been used to nanopattern PLLA films through solvent casting without the swelling issues in another earlier study [30].

6.3.3 High-performance liquid chromatography

We utilized the Agilent Technologies 1100 Series advanced high-performance liquid chromatography (HPLC) facility equipped with a SUPELCOSIL^{TM} LC-18 25 cm x 4.6 mm column (at the W.M. Keck Metabolomics Laboratory in Iowa State University), to measure the amount of *sirolimus* released. The 4-pump HPLC system was equipped with a thermostat-controlled auto-sampler/injector coupled to an Agilent Technologies Mass Selective Trap SL detector integrated with a nanoflow electrospray ion source and an atmospheric pressure chemical ionization source.

The control and patterned substrates with the same surface area and weight of the drug coating (~125 µg/cm^2) were immersed in separate vials of 5.5 mL phosphate buffer solution at room temperature, and the films were allowed to settle in the vial. Sample solutions, 100 µL each, were drawn from the vials at a series of pre-determined times over an eight-day period with a syringe, resulting in 15 samples for each set or a total of 45 samples for one control and two patterned sets. Each sample was stored in a separate vial, at 4°C until the HPLC measurement. The amount of sample drawn (100 µL) was sufficient for the liquid chromatography measurements which require ~10 µL sample per measurement. The amount of phosphate buffer solution remaining in the vial decreases only < 2% for each sample drawn and thereby does not adversely affect the drug release kinetics.

The mobile phase liquid for HPLC was mixture of methanol (80%) and water (20%) with a few drops of acetic acid. For each test sample, 10 µL of the phosphate buffer solution was injected into the HPLC column. The column separates the drug molecule and sends it to the electrospray ion source mass spectrometer to measure the concentration of *sirolimus* in the sample. The entire batch of samples was analyzed at the same time in the HPLC setup to minimize calibration errors. To reduce statistical fluctuations and establish error bars for drug release, HPLC measurements for each sample were performed in triplicate. The sample vials were also kept at 4°C during the HPLC measurement.

6.4 Results and Discussion

6.4.1 Pattern fabrication and characterization

To evaluate the properties of nanoscale patterns on therapeutic coatings, we patterned the PLLA films with periodic nanocup or nanocone arrays using the fabrication steps shown schematically in Figure 6.1. The process illustrated in Figure 6.1 is for fabricating the nanocup array. The process for nanocone patterning is exactly the same except for the use of an inverse polycarbonate master pattern at the initial step. The fabrication details are described in *Experimental Section*.

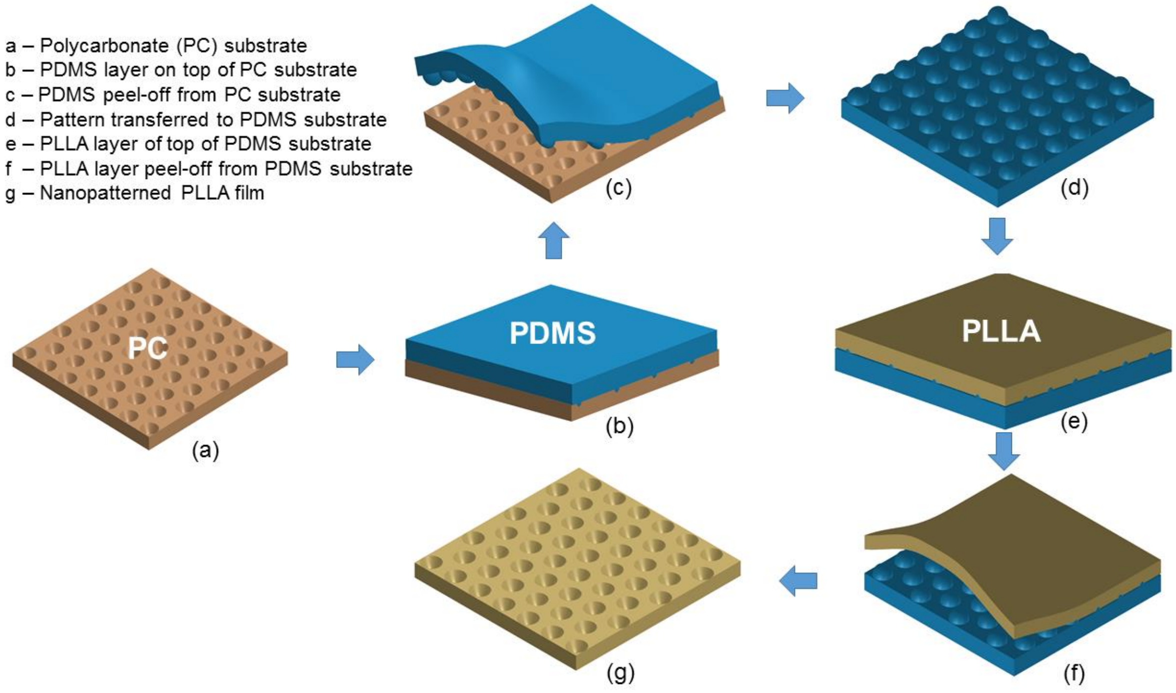

Figure 6.1. Schematic description of the nanoscale PLLA surface patterning process. (a) Polycarbonate (PC) master with nanocup or nanocone pattern. (b-d) First pattern transfer through PDMS replica molding. (e,f) Second pattern transfer through PLLA solvent casting. (g) The final structure exhibits the same pattern as the PC master.

The transferred patterns onto PDMS and PLLA were characterized by scanning electron microscopy (SEM) and atomic force microscopy (AFM) to ensure their pattern fidelity. The SEM and AFM image (Figure 6.9, ESI) of the pattern transferred onto the PDMS surface (e.g. the nanocone array) represents the negative of the master pattern (e.g. the nanocup array). The SEM images of the PLLA films patterned through solvent casting (Figures 6.2a, 6.2b) show excellent fidelity. To further confirm the fidelity of the solvent cast pattern transfer process, we performed AFM scans of the resulting PLLA nanocup (Figure 6.2c) and nanocone (Figure 6.2d) surfaces. The height (~180-190 nm) and shape of the PDMS nanocones are very closely replicated in the PLLA nanocup array which exhibits a similar depth of 182 nm. It implies that the PLLA solution directly cast on the PDMS mold has filled the grooves of the PDMS pattern almost completely, thus resulting in a total replication.

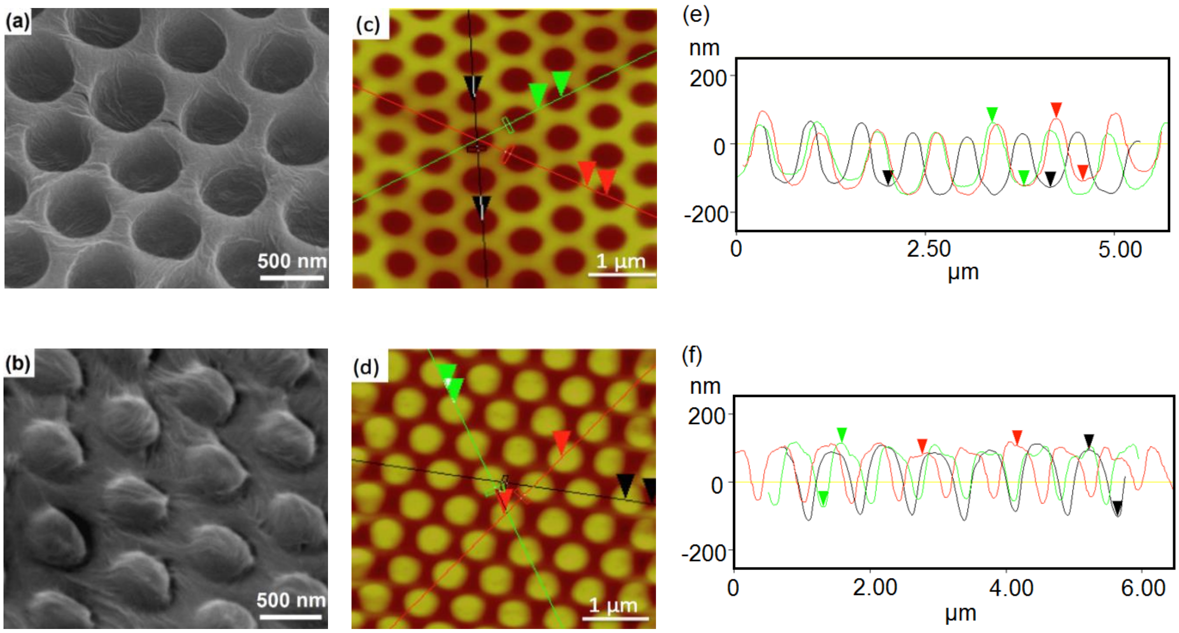

Figure 6.2. The surface of the PLLA films patterned with 750 nm-pitch nanoscale arrays. SEM images of (a) nanocups and (b) nanocones are paired with AFM images (c) and (d) and the section profiles in (e) and (f), respectively. The nanocups exhibit an average depth of 182 nm and the nanocones an average height of 186 nm. Scale bar is 500 nm for (a) and (b) and 1 µm for (c) and (d).

We have also tried nanoimprinting-based patterning of PLLA (Figures 6.10 and 6.11, ESI) but the fidelity was inferior to that from the solvent casting technique. We ascribed the degradation in fidelity to the imprint temperature (~100°C) which is set to considerably lower than what would be usually required for such imprinting to prevent the damage to the polymer and the pattern itself.

6.4.2 Drug coatings on PLLA

To study the drug elution characteristics we selected *sirolimus* (rapamycin) (LC Laboratories, MA) as the coating material since it is an immunosuppresant agent frequently used with coronary stents to prevent stent rejection by the human body. A solution of 1% *sirolimus* (by weight) was prepared in ethanol which is an excellent solvent for *sirolimus* [31] but does not affect the underlying PLLA substrate [32]. The nanocup- and nanocone-patterned PLLA surfaces were conformally coated with 125 μg/cm^2 of *sirolimus* with a fine brush. After coating, the samples were dried at room temperature and weighed in a microbalance. We coated the *same amount* of drug measured by weight (125 μg/cm^2) on the control and patterned surfaces. Otherwise the entire experiment would be meaningless.

The AFM image analysis confirmed that the brush coating conformally coated the corrugated PLLA surface, leaving shallow yet clearly visible depressions on the nanocup-patterned surface, which will be discussed later. The SEM image of *sirolimus*-coated nanocup and nanocone PLLA surface (Figure 6.12, ESI) also shows similar features. Identical coating procedure and *sirolimus* weight were applied to the control (flat), nanocup- and nanocone-patterned PLLA samples. Note that the coated drug is not chemically bonded to the PLLA surface, but adheres to it through weak van der Waals interaction, which facilitates the drug's release.

6.4.3 Hydrophobicity of patterned PLLA

The wetting behavior and effective contact area are critical factors to the interaction between the nanopatterned surface and its liquid-phase ambience [33]. We investigated the changes in the surface characteristics of the PLLA due to the nanopatterning and drug coating by performing contact angle measurements on both the unpatterned and patterned

PLLA samples before and after the *sirolimus* coating. We used a microliter syringe to position a droplet of deionized water on the PLLA film on a glass slide and captured the frontal image using an optical microscope. The contact angle was acquired by processing the images using *ImageJ*. The contact angle measurement results are summarized in Table 6.1.

Table 6.1. Contact angle measurements on control, nanocup, and nanocone patterned PLLA surfaces before and after *sirolimus* coating.

Pattern	***Control***	***Nanocup***	***Nanocone***
Uncoated	87°	106°	116°
Coated	77°	76°	76°

The contact angle has increased in the nanopatterned substrates (Table 6.1), imparting higher hydrophobicity to the patterned surfaces. The increase in the contact angle can be explained through Cassie-Baxter equation which states that increasing the surface roughness increases the contact angle with the compound surface [34]. For a two-component liquid-air system, the Cassie-Baxter equation dictates that:

$$\cos\theta_c = f_1(\cos\theta_1 + 1) - 1 \tag{6.1}$$

where θ_c is the effective contact angle, and θ_1 the equilibrium contact angle of component 1 with area fraction f_1 of the liquid-air interface. Nanopatterning the PLLA surface will increase the area fraction f_1 of the liquid (water) with the film, thus inducing the patterned film to exhibit a higher level of hydrophobicity in comparison with the flat one. The contact angle for the coated PLLA surfaces is less than the uncoated surfaces because the conformal coating fills the nanocups and nanocones to a certain extent, decreasing the depth (height) of the nanocups (nanocones).

6.4.4 Drug release measurement and results

We have established a robust process for measuring the drug released from the PLLA surfaces using high-performance liquid chromatography (HPLC) (*see Experimental Section*). HPLC measures the molecular weight of *sirolimus* derivatives in the phosphate buffer solution. The molecular weight (MW) of *sirolimus* (S) is 914 g mol^{-1}. Due to the interaction of mobile phase liquid (methanol) with sodium glass, a hydrated sodium complex is formed, having MW of 952 g mol^{-1}. The number of counts in the chromatogram corresponding to the MW 952 g mol^{-1} is the highest, thus forming the principal HPLC peak. Other *sirolimus* derived species with different MW have counts that are less than 1% of the principal peak.

The rates of *sirolimus* release from the flat (control), nanocone-, and nanocup-patterned surfaces have been measured over an ~8-day period (see *Experimental Section*) as shown in Figure 6.3. Very counter-intuitively, the nanopatterned surfaces exhibited markedly slower drug release rates when compared with the flat control, even though they have wider surface areas. In the initial 32-hour period, the nanocup samples exhibited 25~30% lower drug release in comparison to the flat control sample. The drug release from the nanocone-patterned sample was higher than that of the nanocup-patterned one but still lower than that of the flat control. The lower release rate implies that the drug coating has adhered to the nanopatterned surfaces for a longer period of time – a highly desired attribute for coronary stents. Even over longer time periods (2-8 days), the drug release rates of the nanocup- and nanocone-patterned surfaces remained below that of the control by ~20% and 7-10%, respectively. Our interpretation of this unexpected finding, based on the hypothesis of incomplete surface wetting, will be presented in the following section.

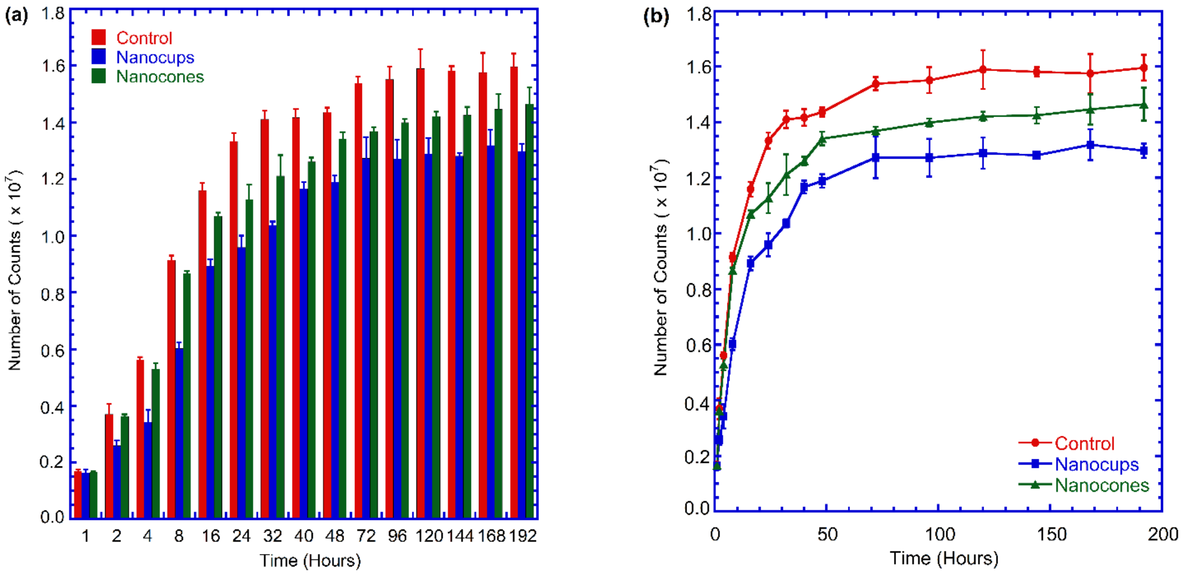

Figure 6.3. (a) Histogram of HPLC-measured quantities of the *sirolimus*-derived species as a function of time. The results from the control (flat), nanocup-patterned, and nanocone-patterned surfaces are superimposed to facilitate comparison. (b) The quantity of *sirolimus*-derived species plotted on a linear scale time axis.

We performed two additional experiments for shorter durations (3 days and 6 days) involving 1 control and 2 patterned samples in each set. The results shown in Figure 6.4 further consistently confirmed the similar slowing of the drug release for nanopatterned drug-coated PLLA samples, in independent experiments and that the slowed drug release was not an artifact of particular experiment conditions.

6.4.5 Drug diffusion

The most significant result is that the nanopatterned substrates release drugs far more slowly than the flat substrates, as observed in a number of independent experiments. This is counter-intuitive since the drug release rate is expected to increase with the contact area. The periodically patterned surfaces have substantially larger surface area than the flat surface. In our nanocup (nanocone) pattern with ~250 nm aperture radius (the conic base radius), 150-250 nm depth (height), and 750 nm pitch, we estimated a 7-20% increase in the surface area.

In spite of the large area increase, the observed drug release rates were lower. Such a slower drug release from the patterned materials involving hydrophobic surfaces (e.g. electrospun fiber meshes, nanoporous templates) has also been reported by others [23-25].

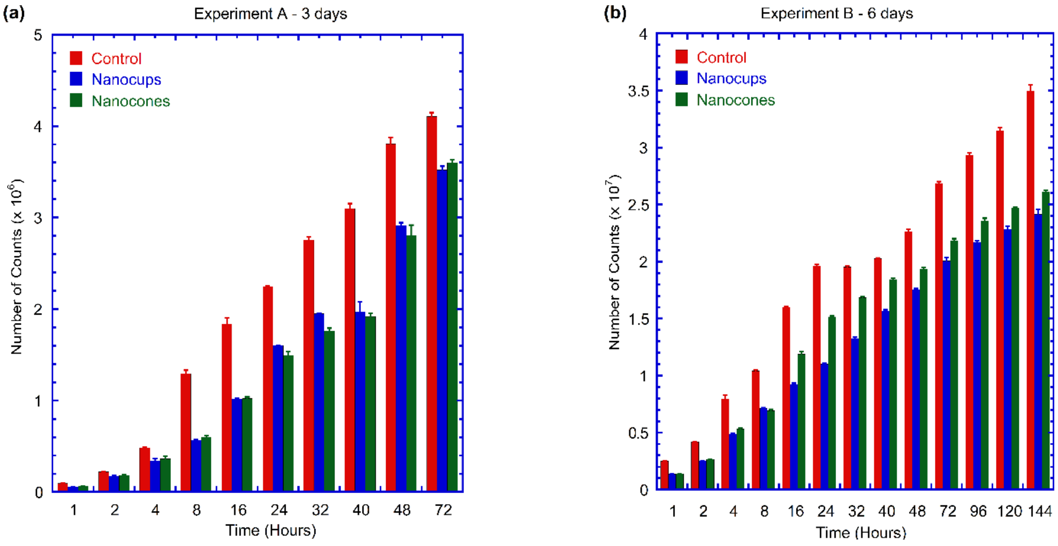

Figure 6.4. (a) Results of an *independent*, shorter-duration 3-day experiment with the histogram of HPLC-measured quantities of the *sirolimus*-derived species as a function of time. The results from the control (flat), nanocup-patterned, and nanocone-patterned surfaces are superimposed. (b) Similar results for another independent 6-day experiment.

We find that the release rate N_s exhibits an approximate asymptotic power-law behavior of $N_s \sim t^{\alpha}$ at shorter times, with $\alpha \sim 0.63$ (flat) and $\alpha \sim 0.53$ (nanocup) and $\alpha \sim 0.66$ (nanocone). This is similar to the square root dependence $N_s \sim \sqrt{t}$ frequently observed in diffusive processes. In accordance, we modeled the release kinetics using the diffusion equation-based model. As is customary, we adopt the separation of variables approach which leads to the power series solution of the amount of material released. Mathematical modeling of controlled drug release from the plane sheet has been widely reported in literature [35-38]. The release of *sirolimus* coated on the PLLA surface into the phosphate buffer solution can be thought of as the drug diffusing from a plane sheet into the solution. For our case, the drug is homogenously coated on the PLLA film and there is no physical barrier separating the drug layer and the polymer. It thus constitutes a monolithic system [35]. We solve the Fick's second law of diffusion

$$\frac{\partial N}{\partial t} = D\frac{\partial^2 N}{\partial x^2} \tag{6.2}$$

by separating the space and time variables with appropriate boundary conditions [39].

We can express the total amount of drug (M_t) leaving the film as a fraction of the corresponding amount after infinite time (M_∞) by the power series relation:

$$\frac{M_t}{M_\infty} = 1 - \frac{8}{\pi^2}\sum_{n=0}^{\infty}\frac{1}{(2n+1)^2}\exp\left(-\frac{(2n+1)^2\pi^2}{4L^2}Dt\right) \tag{6.3}$$

where D is the diffusion coefficient and $2L$ is the thickness of the film. It is to be noted that the above mathematical solution for drug release from both the surfaces of the film can be adapted directly for our case where the release is coming only from one surface. This is because for the case of nearly uniform release, the values of M_t and M_∞ will be reduced by the same factor (~0.5) leaving the resultant ratio M_t/M_∞ unchanged.

We fit the experimental data points for the release to the above equation (6.3) by minimizing the root mean square errors for the experimentally determined PLLA film thickness $2L$ ~ 15 µm. Equation (6.3) was solved for the series with n = 100 terms, though it was found that the results do not differ for n >100. To determine M_∞, we extrapolated the number of counts for long time periods. The best fit was used to extract the value of D for different patterns – control, nanocones, and nanocups. We can see from Figure 6.5a-6.5c that the theoretical fit agrees well with the experimental data, except for the case of nanocones where a slight deviation from the experimental data is evident. For the best fit, we tabulate the corresponding values of *D* in Table 6.2. In practice, the diffusive drug release is three-dimensional, which can create considerable modeling complexity. Since the drug elution is primarily in a single Cartesian direction, the use of one-dimensional diffusion analysis is justified.

Table 6.2. Diffusion coefficients for different pattern types extracted from data fit.

Pattern	**Diffusion Coefficient (D) (10^{-12} cm^2/s)**	**$D_{pattern}/D_{control}$**
Control	3.95	1.00
Nanocups	2.92	0.74
Nanocones	3.67	0.93

The fact that the nanocups exhibits the smallest value of *D* indicates that the release is *slowest* in the nanocups among all the three patterned surfaces, even though the surface area has increased after nanopatterning. This is the result of the nanopatterning (Figure 6.2) which renders it hydrophobic, making it difficult for the solution to wet the PLLA surface. From Table 6.2, the value of *D* for the control is the highest followed by the nanocones and nanocups. Since the diffusion of drug from PLLA into the surrounding solution is proportional to the area of the liquid actually in contact with the patterns [40], we infer that the liquid is able to wet only a part of the area in nanocones and nanocups when compared with the control. We support this *incomplete wetting* hypothesis by calculating the wetting area in the next section.

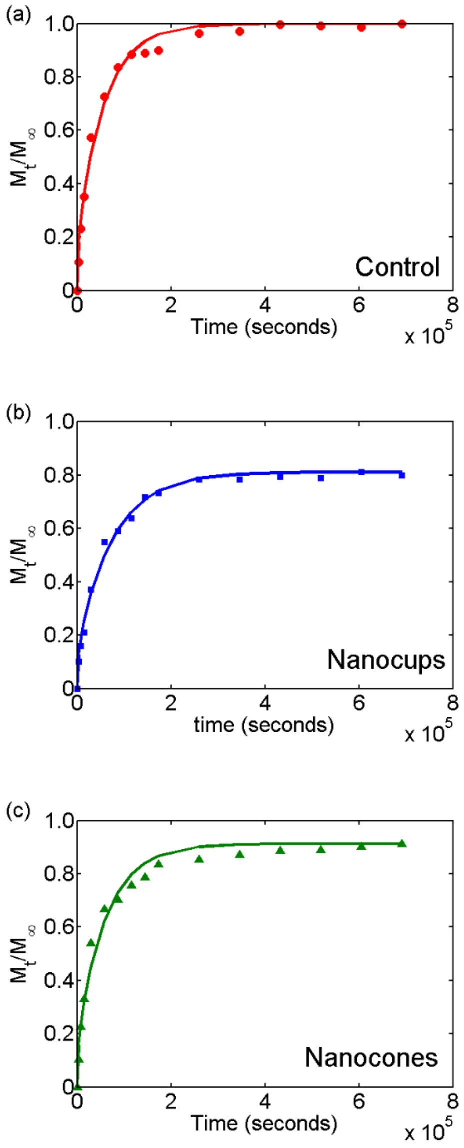

Figure 6.5. Experimental results fitted to the model and plotted as a function of time for (a) control, (b) nanocup, and (c) nanocone arrays.

6.4.6 Incomplete wetting due to nanopatterning

We attribute the slowed drug release from the nanopatterned PLLA surface to the morphologically induced incomplete wetting which has been observed in a variety of configurations [41]. As the theoretical framework, we have adopted the curvature minimization-based approach of Berthier *et al.* [42] according to which the area of the nanopatterned, *sirolimus*-coated PLLA surface in contact with the buffer solution depends strongly on the nanopattern's cross-sectional shape and the wetting properties of the constituent materials. Through judicious structural design and material selection, the nanopatterned surface can be made not only to impede its total wetting but also to support multiple wetting states, enabling stepwise control of the contact area and drug release rate.

Figure 6.6a shows the model structure of one individual nanocup. The grey region represents the *sirolimus*-covered PLLA with its intrinsic contact angle θ at 77°. We assumed that the nanocup's cavity was originally filled with air. The radius of curvature (r) and diameter (d) of the nanocup aperture's edge were set to 100 and 400 nm, respectively, which closely match the fabricated nanocup geometry. Due to the rounding of the edge with a finite r, the outermost diameter h becomes $h = d + 2r$. From the nanocup configuration in Figure 6.6a, we found two wetting states shown in Figure 6.6a and 6.6b, respectively.

As shown in Figure 6.6a, the first wetting state sets its three-phase interface on the curved portion of the nanocup's edge. To find the position (ϕ_1) and radius of curvature (R_1) of the convex meniscus, we modified the formulas in ref. 42 as:

$$\phi_1 = \theta + \cos^{-1}\frac{r.\sin\theta}{h/2} \tag{6.4}$$

$$R_1 = \frac{\frac{h}{2} - r.\sin\phi_1}{\sin(\phi_1 - \theta)} \tag{6.5}$$

The calculated ϕ_1 and R_1 are 147° and 260 nm, respectively.

The analysis has found another wetting state that has its three-phase interface on the onset of the nanocup's straight edge as shown in Figure 6.6b. Based on the formula in ref. 42,

$$R_2 = \frac{d/2}{\sin(\theta - \alpha)} \tag{6.6}$$

where α is the edge slope angle as defined in Figure 6.6b. We set α to 100° in accordance with the SEM image analysis. The calculated second state radius R_2 is 515 nm at $\phi_2=\alpha$. Similar nanoscale meniscus formation has been observed in other configurations, such as nanofluidic channels, as well [43].

In either state, the area in contact with the liquid is smaller than that of the flat surface. In the present nanocup geometry, the contact area for the flat surface is $\pi(h/2)^2$ = 0.283 μm^2. The contact areas for the wetting states 1 and 2, calculated from the torus surface integration, are 0.098 and 0.211 μm^2 which correspond to only 35% and 75% of that of the control, respectively. Such a partial wetting, in turn, would result in a severe reduction in contact area and a markedly lower drug release. Indeed, the experimental observations in previous section indicate that the nanopatterning has resulted in approximately 25-30% lower *sirolimus* release rates. Such reductions are consistent with the incomplete wetting model. As indicated by Figure 6.6b, however, even the second state does not lead to a full wetting of the nanopatterned surface. It leads to the possibility of observing un-dissolved *sirolimus* at the bottom of the nanocup even after a long-term release, which is confirmed by the SEM image in Figure 6.6c taken after 12 days of release. The residual *sirolimus* also explains why the total amount of drug released from the two nanopatterned substrates could not converge to that of the control within the observation period.

Owing to the availability of two wetting states, it becomes also probable that the meniscus was originally pinned on the curved edge with its radius at R_1 but moved to R_2 as the result of a certain perturbation, such as the change in the edge shape due to the dissolution of *sirolimus* or mechanical agitation in the liquid body. The resulting increase in the surface area would have increased the *sirolimus* release rate, causing an abrupt change in the measurement. Although we have not extended the curvature minimization approach to the nanocone array due to the concerns over its axis-asymmetry, we expect the incomplete wetting would also arise near the waist of the nanocone where the radius of curvature changes rapidly.

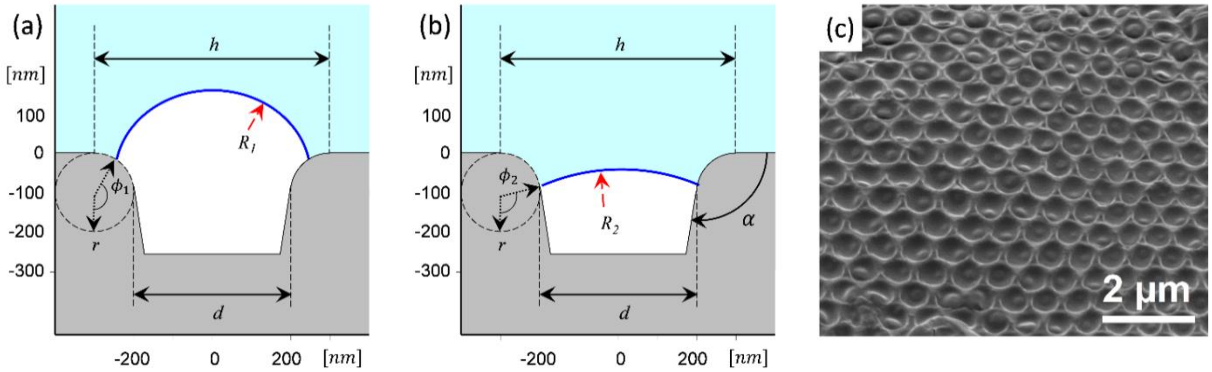

Figure 6.6. The calculated wetting behaviors of water at the *sirolimus*-coated PLLA nanocup structure (r = 100 nm, d = 400 nm). Two wetting states have been found. The first state (a) is pinned at the round edge with the radius of curvature R_1 at 260 nm. The second state (b) is pinned at the starting point of the straight edge with R_2 = 515 nm. (c) SEM image of the nanopatterned PLLA surface after 12 days of drug release experiment. The image clearly shows the existence of the un-dissolved, residual *sirolimus* at the bottom of the nanocups. Scale bar = 2 µm.

We quantitatively estimated the drug delivery rate by measuring the depth profile of the *sirolimus* coated PLLA surfaces with AFM scans. Six *sirolimus*-coated, nanocup-patterned PLLA samples were placed in the saline buffer solution over time periods up to 10 days (as in Figure 6.3) and then retrieved one by one after 1, 2, 4, 6, 8 and 10 days of immersion. Then the samples were dried and characterized by AFM scans. The results in Figure 6.7 show that the gradual release of the drug leads to an increased exposure of the nanopatterned PLLA surface which, in turn, makes the surface more hydrophobic and further slows down the release. Figure 6.7a shows that the AFM-measured average depth of the nanocups increases nearly linear with the drug release duration. The AFM scans in Figure 6.7b-6.7d also show that the nanocup profiles become deeper as the drug release progresses. After the 10-day release experiment the resulting depth of the nanocup array was 154 nm which is significantly less than that of the uncoated PLLA surface (182 nm), indicating the existence of the residual *sirolimus* at the bottom of the nanocup.

We also confirmed that the *sirolimus*-coated patterned PLLA surfaces become more hydrophobic as the drug release progresses, since the nanostructure gets increasingly exposed as shown in Figure 6.7. We measured the contact angle of a water drop on the nanocup-patterned surface in parallel with the drug-release experiment described above. Each time a *sirolimus*-coated, nanocup-patterned PLLA sample was retrieved from the saline buffer solution, we performed contact angle measurements on it. Figures 6.8a and 6.8b show that as more *sirolimus* is released, the surface becomes more hydrophobic, with the contact angle starting at 76° and approaching that of the uncoated surface (106°) as shown in Table 6.3. The water droplet picture after 1 day and 10 day release is shown in Figure 6.8a and the corresponding change in contact angle over a period of 10 days is plotted in Figure 6.8b. The plot in Figure 6.8b also indicates that the rate of the contact angle increase begins to saturate from the 8-day point. There is still hydrophobicity in the drug-coated patterned surface at the beginning of the experiment, indicated by larger contact angle (Table 6.1 and Figure 6.8), which indeed changes the interaction of drug with the medium and results in different drug release profiles.

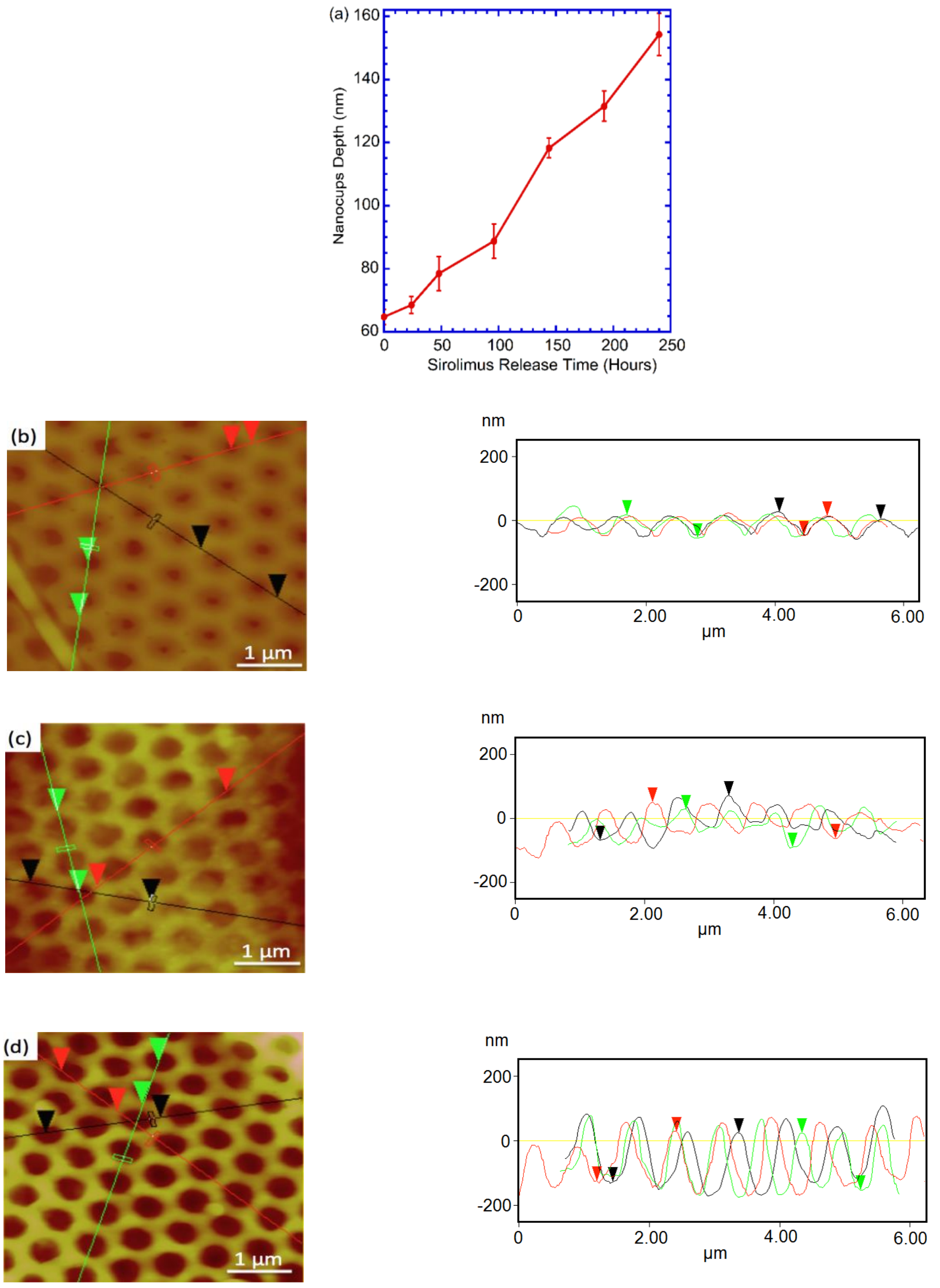

Figure 6.7. (a) The AFM-measured nanocup depth as a function of the *sirolimus* release time. The AFM images and depth profiles of the *sirolimus*-coated PLLA nanocups (b) before the release, (c) after 6 days of release, and (d) after 10 days of release. The corresponding average depths are 65, 118, and 154 nm, respectively. (Scale bars: 1 µm)

Table 6.3. Average contact angle for the nanocup surface coated with *sirolimus*, as a function of time (in days) during which the drug release measurements were carried out. The patterned substrate was dried after each drug release period and the contact angle for the water drop was measured.

Days	**Avg. Contact Angle (degree)**
0	76
1	77
2	79
4	83
6	96
8	102
10	104

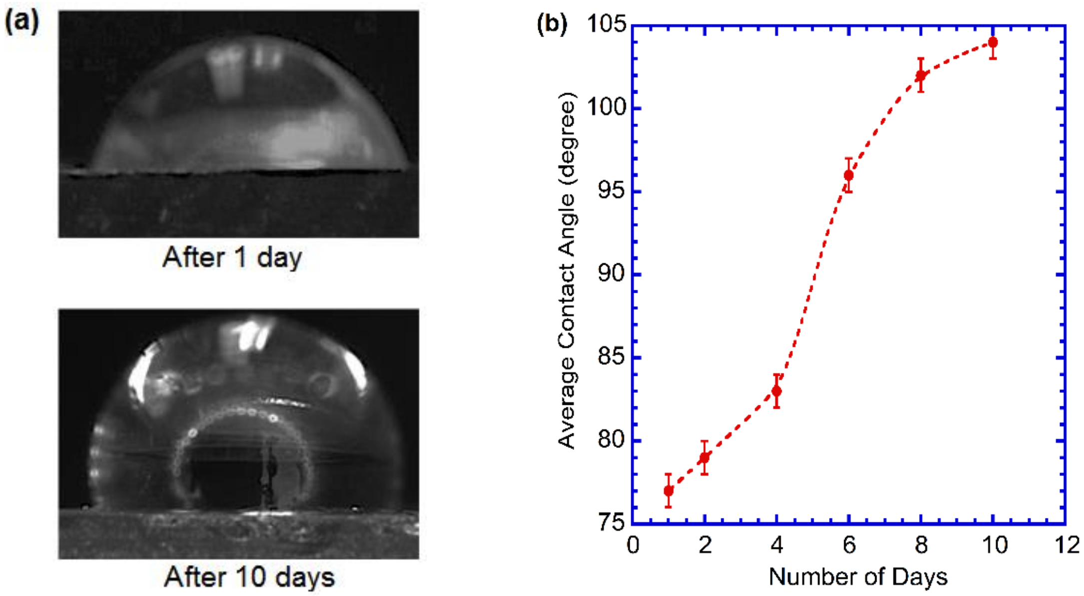

Figure 6.8. (a) Photograph of water droplet on nanocup patterned surface after 1 and 10 days. (b) Graph of average contact angle versus time in days.

As summarized in Table 6.4, similar slowing-down of drug release has been observed in laser nano-textured PLA [20], and native, melted, and degassed 10% PGC-C18-doped PCL electrospun meshes [24]. Nanoporous block copolymers [25] have shown an analogously slower drug release over a longer periods exceeding 80 days and 6 days. This type of slower drug release over ~1 hour has also been observed from surfaces textured with ethyl cellulose layers [44]. As we noted earlier, mechanical agitation can lead to abrupt changes and release of these unexposed *sirolimus* regions. Such abrupt changes have also been observed in dopamine release from highly corrugated surfaces [45].

It is of interest to pattern biodegradable surfaces with microscale patterns and compare with nanoscale pattern behavior found here. Other biocompatible polymers such as PLGA are expected to show similar results as in the present study, since the drug-liquid-surface interactions are similar. These patterned PLLA films can also be rolled into tubular structures which can be used as templates for tissue culture and coronary stents (Figure 6.13, ESI).

Table 6.4. List of existing drug release experiments.

Ref.	**Author**	**Material**	**Result**
20	R. Nair et al.	Nitinol (55% Ni, 45% Ti) metal mesh coated with PLA	93% release (control) to 51% release (laser nanotextured)
23	H. Xu et al.	Polyvinyl butyral (PVB) polymer electrospun fiber with Acetaminophen and 5-fluorouracil	Fig. 6A – Acetaminophen: >70% release (PVB alone) to ~45% release (PVB + 60 min electrospinning)
24	S.T. Yohe et al.	poly(ε-caprolactone) electrospun meshes with SN-38 coating	Fig. 3B – SN-38: 30 days for full release (melted electrospun) vs. ~70 days for full release (electrospun)
25	K. H. Lo et al.	polystyrene-*b*-poly(l-lactide) (PS−PLLA) block copolymer with sirolimus	100% release (AAO hybrid) to ~85% released lamellar nanoarrays)
44	N. Genina et al.	Ethyl cellulose (EC) coated paper substrates with propranolol hydrochloride (PH) and riboflavin sodium phosphate (RSP)	Fig. 7D,E,F – RSP: 85% release (without EC) to 65% release (5 layers of EC) to 25% release (30 layers of EC)
45	K. Gulati et al.	Ti wires with TiO_2 nanotube (TNT) with dopamine and doxorubicin	Burst (~ 6 hours) + release (8 days): (No control)

6.5 Conclusion

We have measured the rates of drug elution from the nanopatterned PLLA surfaces, prepared by a simple and reproducible technique developed for this work, and compared the results with that of the flat control surface. The nanopatterned surfaces exhibit a 25-30% slower release over a period of eight days when compared with the flat, unpatterned surfaces. The slower release is attributed to the nanopattern-induced incomplete wetting of the PLLA surface. We envisage that the geometry and pitch of the nanostructure can be further controlled to provide more refined tailoring of the drug release rate. These are promising directions for improving the performance of drug-eluting stents in cardiac therapies.

6.6 Electronic Supplementary Information

6.6.1 PDMS mold SEM

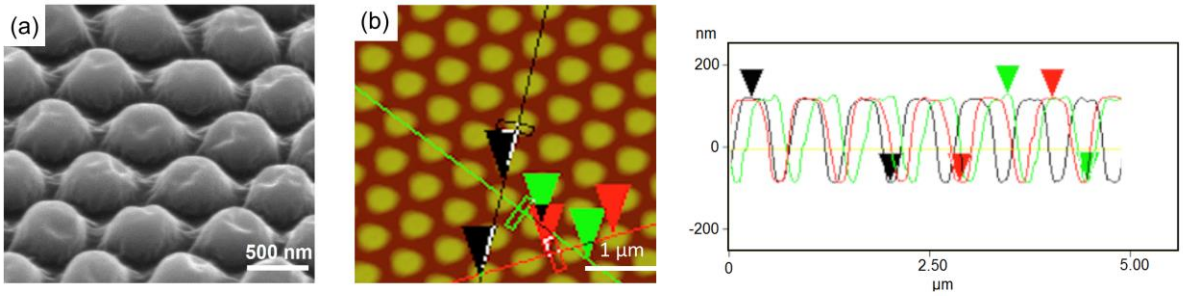

Figure 6.9. The surface of PDMS mold patterned with 750 nm pitch nanocone arrays. (a) SEM images of nanocones and (b) AFM images and the section profile. The nanocones exhibit average depths of 189 nm. Scale bar = 500 nm for (a) and 1 μm for (b).

6.6.2 PLLA nanoimprinting trials and results

We also attempted nanoimprinting of PLLA by stamping the nanopatterned PDMS mold onto a PLLA film as shown in Figure 6.10. For this, the PLLA film was first prepared on the glass substrate by spin-coating (500 rpm, 60 seconds) and dried at room temperature for ~12 hours. Then the PDMS stamp was placed on the PLLA film with the pattern side facing the PLLA surface. Another glass substrate of the same dimensions covered the other side. The two glass substrates were pressed against each other using binder clips and the whole assembly was placed on a hot plate set at 100°C for 35 minutes. The glass transition temperature (T_g) of PLLA is ~60 °C. Therefore, the patterns in the PDMS can be fully embossed into the PLLA surface at a temperature (100°C) higher than T_g. Finally, the PLLA film was gently peeled off from the glass substrate by tweezers. The SEM images of nanoimprinted nanocup and nanocone PLLA films are shown in Figure 6.11.

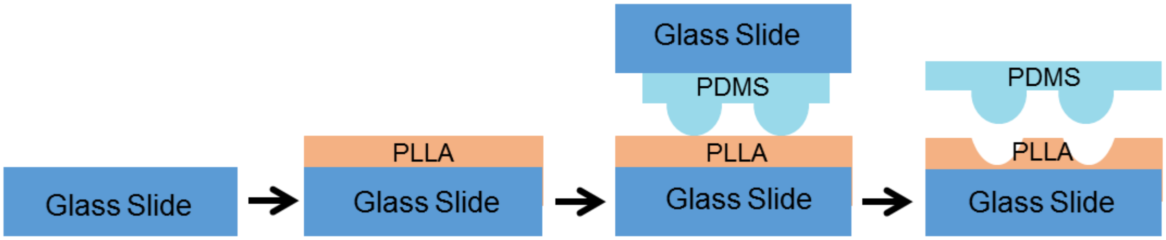

Figure 6.10. Process diagram for the imprinting-based nanotexturing of PLLA film. First, PLLA solution in chloroform is spin-coated on the glass slide. The PDMS stamp touching the PLLA is held between two glass slides and pressure is applied with the binder clips. The array of nanoholes is revealed on the PLLA after the pressure from binder clips is released.

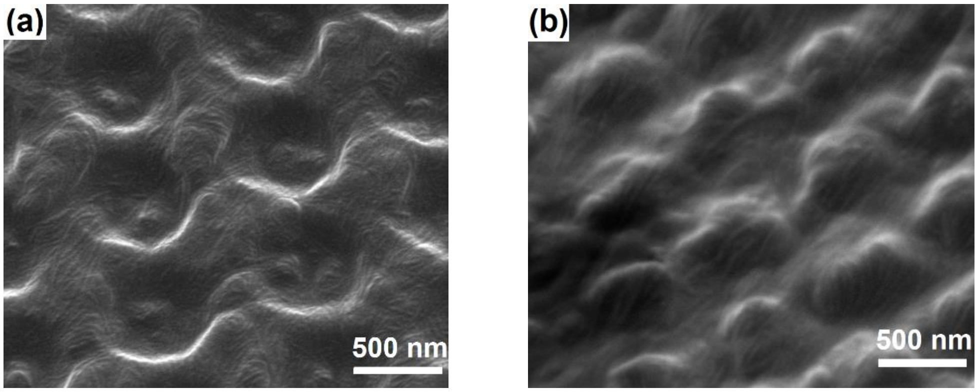

Figure 6.11. SEM images of nanoimprinted PLLA films (a) nanocups, (b) nanocones. (Scale bars: 500 nm for all)

6.6.3 PLLA surface brush coated with sirolimus

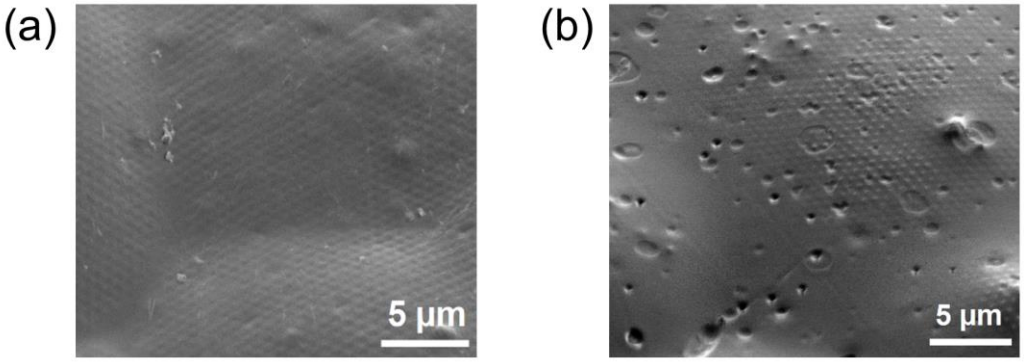

Figure 6.12. SEM image of the PLLA for (a) nanocup (b) nanocone array brush-coated with sirolimus. (Scale bar: 5 µm)

6.6.4 PLLA tubular structures

The nanopatterned PLLA films can easily be rolled into tubular forms. These PLLA tubes with patterns on the inner side can be used as scaffolding structures for cell culture and a framework for fabricating coronary stents. As shown in Figure 6.13, we wrapped the nanopatterned PLLA films around a cylindrical tube and joined the edge by dissolving it with chloroform using a fine brush. The diameter of the tube was ~2 mm and the length was ~1 cm.

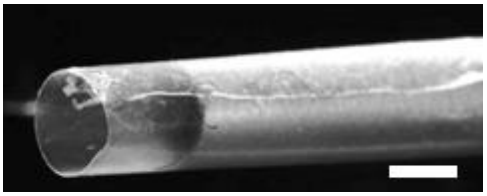

Figure 6.13. Optical microscope image of the PLLA tubular structure. (Scale bar: 2 mm)

6.7 Acknowledgements

This research was supported by the National Science Foundation through Grant CMMI-1265844. We thank Dr. W. Straszheim from the Materials Analysis and Research Laboratory

(MARL) of Iowa State University for assistance with scanning electron microscopy. This research used the resources of W.M. Keck Metabolomics Laboratory at Iowa State University. We thank Dr. M. A. Perera from W.M. Keck Metabolomics Laboratory, E. Manna from Ames Laboratory, and members of the Ames Laboratory Photonic Systems group for stimulating discussions.

6.8 References

1. A. Bandyopadhyay, S. Bose, S. Das, "3D printing of biomaterials," *MRS Bull.* **40**, 108-115 (2015).
2. X. M. Zhao, Y. Xia, G. M. Whitesides, "Fabrication of three-dimensional micro-structures: Microtransfer molding," *Adv. Mater.* **8**, 837-840 (1996).
3. G. M. Whitesides, E. Ostuni, S. Takayama, X. Jiang, D. E. Ingber, "Soft lithography in biology and biochemistry," *Annu. Rev. Biomed. Eng.* **3**, 335-373 (2001).
4. E. P. Childers, M. O. Wang, M. L. Becker, J. P. Fisher, D. Dean, "3D printing of resorbable poly (propylene fumarate) tissue engineering scaffolds," *MRS Bull.* **40**, 119-126 (2015).
5. M. J. Choi, K. J. Cha, H. W. Kim, M. H. Na, B. K. Lee, W. Hwang, D. S. Kim, "Microchamber/nanodimple polystyrene surfaces constructing cell aggregates fabricated by thermoset mold-based hot embossing," *Microelectron. Eng.* **110**, 340-345 (2013).
6. Y. Tian and L. Jiang, "Design of bioinspired, smart, multiscale interfacial materials with superwettability," *MRS Bull.* **40**, 155-165 (2015).
7. K. R. Milner and C. A. Siedlecki, "Submicron poly (L-lactic acid) pillars affect fibroblast adhesion and proliferation," *J. Biomed. Mater. Res. A* **82**, 80-91 (2007).
8. Y. Zhu, C. Gao, Y. Liu, J. Shen, "Endothelial cell functions in vitro cultured on poly (L-lactic acid) membranes modified with different methods," *J. Biomed. Mater. Res. A* **69**, 436-443 (2004).
9. F. Badique, D. R. Stamov, P. M. Davidson, M. Veuillet, G. Reiter, J. N. Freund, C. M. Franz, K. Anselme, "Directing nuclear deformation on micropillared surfaces by substrate geometry and cytoskeleton organization," *Biomaterials* **34**, 2991-3001 (2013).

10. P. M. Davidson, H. Özçelik, V. Hasirci, G. Reiter, K. Anselme, "Microstructured Surfaces Cause Severe but Non-Detrimental Deformation of the Cell Nucleus," *Adv. Mater.* **21**, 3586-3590 (2009).

11. S. Shi, X. H. Wang, G. Guo, M. Fan, M. J. Huang, Z. Y. Qian, "Preparation and characterization of microporous poly (D, L-lactic acid) film for tissue engineering scaffold," *Int. J. Nanomedicine* **5**, 1049-1055 (2010).

12. C. Miller, H. Shanks, A. Witt, G. Rutkowski, S. Mallapragada, "Oriented Schwann cell growth on micropatterned biodegradable polymer substrates," *Biomaterials* **22**, 1263-1269 (2001).

13. G. E. Rutkowski, C. A. Miller, S. Jeftinija, S. K. Mallapragada, "Synergistic effects of micropatterned biodegradable conduits and Schwann cells on sciatic nerve regeneration," *J. Neural Eng.* **1**, 151-157 (2004).

14. L. Moroni, L. P. Lee, "Micropatterned hot-embossed polymeric surfaces influence cell proliferation and alignment," *J. Biomed. Mater. Res. A* **88**, 644-653 (2009).

15. G. Vozzi, C. Flaim, A. Ahluwalia, S. Bhatia, "Fabrication of PLGA scaffolds using soft lithography and microsyringe deposition," *Biomaterials* **24**, 2533-2540 (2003).

16. S. H. Hsu, C. Y. Chen, P. S. Lu, C. S. Lai, C. J. Chen, "Oriented Schwann cell growth on microgrooved surfaces," *Biotechnol. Bioeng.* **92**, 579-588 (2005).

17. S. K. Mallapragada, T. M. Brenza, J. M. McMillan, B. Narasimhan, D. S. Sakaguchi, A. D. Sharma, S. Zbarska, H. E. Gendelman, "Enabling nanomaterial, nanofabrication and cellular technologies for nanoneuromedicines," *Nanomed. Nanotechnol. Biol. Med.* **11**, 715-729 (2015).

18. M. E. Marti, A. D. Sharma, D. S. Sakaguchi, S. K. Mallapragada, "Nanomaterials for neural tissue engineering," in *Nanomaterials in Tissue Engineering*, ed. A. K. Gaharwar, S. Sant, M. J. Hancock, S. A. Hacking, Woodhead Publishing, Sawston, 2013, Ch. 10, 275-301.

19. A. D. Sharma, S. Zbarska, E. M. Petersen, M. E. Marti, S. K. Mallapragada, D. S. Sakaguchi, "Oriented growth and transdifferentiation of mesenchymal stem cells towards a Schwann cell fate on micropatterned substrates," *J. Biosci. Bioeng.* **121**, 325-335 (2015).

20. R. Nair, V. Molian, P. Molian, "Femtosecond Laser Nanotexturing of Drug-Eluting Stents," *J. Manuf. Sci. Eng.* **134**, 061008 (2012).

21. S. C. Gott, B. A. Jabola, M. P. Rao, "Vascular stents with submicrometer-scale surface patterning realized via titanium deep reactive ion etching," *J. Micromech. Microeng.* **25**, 085016 (2015).

22. X. Sedao, T. J.-Y. Derrien, G. R. B. E. Romer, B. Pathiraj, A. J. Huis in ‘t Veld, *Appl. Phys. A* **111**, 701-709 (2013).

23. H. Xu, H. Li, J. Chang, “Controlled drug release from a polymer matrix by patterned electrospun nanofibers with controllable hydrophobicity,” *J. Mater. Chem. B* **1**, 4182-4188 (2013).

24. S. T. Yohe, Y. L. Colson, M. W. Grinstaff, “Superhydrophobic materials for tunable drug release: using displacement of air to control delivery rates,” *J. Am. Chem. Soc.* **134**, 2016-2019 (2012).

25. K. H. Lo, M. C. Chen, R. M. Ho, H. W. Sung, “Pore-Filling Nanoporous Templates from Degradable Block Copolymers for Nanoscale Drug Delivery,” *ACS Nano* **3**, 2660-2666 (2009).

26. R. M. Ho, W.-H. Tseng, H.-W. Fan, Y.-W. Chiang, C.-C. Lin, B.-T. Ko, B.-H. Huang, “Pore-Filling Nanoporous Templates from Degradable Block Copolymers for Nanoscale Drug Delivery,” *Polymer* **46**, 9362–9377 (2005).

27. Y. T. Tseng, W.-H. Tseng, C.-H. Lin, and R. M. Ho, “Fabrication of Double-Length-Scale Patterns via Lithography, Block Copolymer Templating, and Electrodeposition,” *Adv. Mater.* **19**, 3584–3588 (2007).

28. Benchmark Technologies, http://www.benchmarktech.com/imprintstamps.

29. J. N. Lee, C. Park and G. M. Whitesides, “Solvent Compatibility of Poly(dimethylsiloxane)-Based Microfluidic Devices,” *Anal. Chem.* **75**, 6544-6554 (2003).

30. K. R. Milner and C. A. Siedlecki, “Fibroblast response is enhanced by poly(L-lactic acid) nanotopography edge density and proximity,” *Int. J. Nanomedicine* **2**, 201–211 (2007).

31. P. J. Gandhi, Z. V. P. Murthy, “Solubility and Crystal Size of Sirolimus in Different Organic Solvents,” *J. Chem. Eng. Data* **55**, 5050-5054 (2010).

32. S. Sato, D. Gondo, T. Wada, S. Kanehashi, K. Nagai, “Effects of Various Liquid Organic Solvents on Solvent-Induced Crystallization of Amorphous Poly (lactic acid) Film,” *J. Appl. Polym. Sci.* **129**, 1607-1617 (2013).

33. Y. C. Jung, B. Bhushan, “Contact angle, adhesion and friction properties of micro-and nanopatterned polymers for superhydrophobicity,” *Nanotechnology* **17**, 4970-4980 (2006).

34. A. B. D. Cassie, S. Baxter, “Wettability of porous surfaces,” *Trans. Faraday Soc.* **40**, 546-551 (1944).

35. J. Siepmann, F. Siepmann, “Modeling of diffusion controlled drug delivery,” *J. Control. Release* **161**, 351-362 (2012).

36. X. Wang, S. S. Venkatraman, F. Y. Boey, J. S. Loo, L. P. Tan, “Controlled release of sirolimus from a multilayered PLGA stent matrix,” *Biomaterials* **27**, 5588-5595 (2006).

37. F. Alexis, S. S. Venkatraman, S. K. Rath, F. Boey, “In vitro study of release mechanisms of paclitaxel and rapamycin from drug-incorporated biodegradable stent matrices,” *J. Control. Release* **98**, 67-74 (2004).

38. J. Siepmann, F. Lecomte, R. Bodmeier, “Diffusion-controlled drug delivery systems: calculation of the required composition to achieve desired release profiles,” *J. Control. Release* **60**, 379-389 (1999).

39. J.-M. Vergnaud, *Controlled Drug Release of Oral Dosage Forms*, CRC Press, Boca Raton, 1993.

40. M. Kent, *Advanced Biology*, Oxford University Press, Oxford, 2000.

41. E. Martines, K. Seunarine, H. Morgan, N. Gadegaard, C. D. Wilkinson, M. O. Riehle, “Superhydrophobicity and superhydrophilicity of regular nanopatterns,” *Nano Lett.* **5**, 2097-2103 (2005).

42. J. Berthier, F. Loe-Mie, V. M. Tran, S. Schoumacker, F. Mittler, G. Marchand, N. Sarrut, “On the pinning of interfaces on micropillar edges,” *J. Colloid Interface Sci.* **338**, 296-303 (2009).

43. P. Kim, H. Y. Kim, J. K. Kim, G. Reiter, K. Y. Suh, “Multi-curvature liquid meniscus in a nanochannel: Evidence of interplay between intermolecular and surface forces,” *Lab Chip* **9**, 3255-3260 (2009).

44. N. Genina, D. Fors, H. Vakili, P. Ihalainen, L. Pohjala, H. Ehlers, L. Kassamakov, E. Haeggström, P. Vuorela, J. Peltonen, N. Sandler, “Tailoring controlled-release oral dosage forms by combining inkjet and flexographic printing techniques,” *Eur. J. Pharm. Sci.* **47**, 615-623 (2012).

45. K. Gulati, M. Aw, D. Losic, “Nanoengineered drug-releasing Ti wires as an alternative for local delivery of chemotherapeutics in the brain,” *Int. J. Nanomedicine* **7**, 2069-2076 (2012).

CHAPTER 7

CONCLUSION AND FUTURE OUTLOOK

We have successfully demonstrated the fabrication of large-area nanopatterned structures using soft lithography. Using this approach, we have achieved high-fidelity nanoscale patterns on polymers such as polystyrene and poly(L-lactic acid). The nanopatterned polymer surfaces, when coated with thin metal layers, form nanostructured metallic surfaces, which show interesting optical properties due to plasmonic light concentration. We have shown the applications of these nanopatterned structures in light-trapping architectures for solar cells and templates for controlled drug elution.

In the area of photovoltaics, polymer microlens arrays fabricated from soft lithography can be coupled directly to the air-glass side of the solar cell. Using rigorous scattering matrix simulations, we have shown that the presence of microlens array alone enhances the photocurrent by > 5-10% in organic and perovskite solar cells. The performance improvement is a result of the reduced surface reflection and increased path-length of light within the active layer. It is further shown that coupling the microlens-based solar cell architecture with nanotextured back electrode enhances the photocurrent in organic solar cells by > 50% due to light focusing and the presence of waveguided modes inside the organic absorber region.

In the area of plasmonics, we showed the interesting optical phenomena of extraordinary light transmission through periodic nanocup array without any metal holes. The nanocup array structure with sub-750 nm periodicity was fabricated in polystyrene film using nanoimprint lithography and was overcoated with a non-uniform layer of gold using angle-directed deposition. The resulting array with ultrathin gold layer at each nanocup base generated an extraordinary optical transmission at wavelengths close to the period of the structure. The electric field intensity was enhanced 100-fold near the bottom of the nanocup cavity due to plasmonic light concentration. The quantum dots whose emission wavelength overlapped with the extraordinary optical transmission wavelength of the nanocup array were placed within the nanocups in solution phase. Time-resolved photoluminescence at picosecond time scales revealed that the PL decay rate of the quantum dots in the plasmonically coupled system could be enhanced by more than an order of magnitude. The faster PL decay was a result of the high electric field intensity enhancement due to plasmonic light concentration at the bottom of the nanocup cavity. This demonstration of solution-based coupling between quantum dots and gold nanocups opens new possibilities for applications that would benefit from a solution environment such as biosensing.

In the area of biomaterials, we have demonstrated that nanopatterning the surface of biopolymer poly(L-lactic acid) slows down the drug release rate by 25-30% over a period of eight days. This slowing down in the drug release rate is a consequence of the polymer surface becoming hydrophobic after nanopatterning, even though the effective surface area becomes larger. We have also performed the contact angle measurements and microfluidic simulations to confirm the incomplete wetting behavior resulting from surface nanopatterning. This drug release scheme has the potential to improve the design of drug-eluting stents used for treating blocked or narrowed arteries in cardiac therapies.

As an ongoing effort, we are currently developing a nanopatterning strategy to increase the outcoupling of light from organic light emitting diodes (OLEDs). In OLEDs, the fraction of the outcoupled light into air is only ~17-20% in conventional bottom-emitting devices in the absence of extraction measures. This is due to several loss paths within the device, such as photons trapped in the substrate due to total internal reflection (TIR) at the glass/air interface, photons waveguided in the high index organic and anode layers, and photons dissipated at the organic/metal cathode by surface plasmon excitation. The losses due to internal waveguiding through organic layers and photon dissipation due to surface plasmons at metal cathode add up to > 50%, whereas the external waveguiding through the flat glass or plastic substrate to its edges accounts for an additional 30% loss of light. We have already demonstrated the use of microlens arrays to improve the extraction of externally waveguided light. However, minimizing the internally trapped light and plasmon-related loss has proven to be challenging. The proposed conformal nanopatterning of the OLED layers will disrupt the internal waveguiding within the organic layer and reduce the plasmonic losses. The optimization of critical parameters such as pattern periodicity and corrugation height for achieving the maximal outcoupling remain a challenge.

A future aspect of the work would be to study the manifestation of interesting applications demonstrated in this dissertation for structures with microscale-level features. The microscale-level structures are easier to fabricate with lower cost and higher scalability, making them more suitable for practical industry-based applications. Another important direction would be to fabricate hierarchical structures by combining the microscale structures with nanoscale-level features. Those multi-level hierarchical structures will be particularly useful for fabricating functional materials and metasurfaces aimed at realizing unusual optical signatures.